UNIVERSITÀ DEGLI STUDI DI PADOVA
Dipartimento di Fisica e Astronomia "Galileo Galilei"
Master Degree in Physics

Final Dissertation

Simulation of neutron inspection techniques based on laser-plasma neutron beam and first experiments with Cf source

Thesis supervisor	Candidate
Prof. Sandra Moretto	Ahmar Khaliq
Thesis co-supervisor	
Dr. Felix Pino	

Academic Year 2022/2023

Abstract

The purpose of this thesis is to explore the potential of laser-plasma acceleration technology for producing neutron sources to be used for the volumetric inspection of cargo containers at seaports and airports. The goal is to enhance the detection of hazardous and illicit materials. Neutron beams interact with the sample being inspected, causing the emission of characteristic gamma radiation. The analysis of this radiation enables the determination of the composition of various materials without causing visible damage or changes in their chemical composition. In recent years, the development of ultra-short, super-intense lasers with higher intensities of 10^{19} W/cm^2 has opened up new opportunities for laser-plasma interaction and particle acceleration. Laser-driven particle acceleration, which involves the production of high-energy electrons and ions, is becoming an increasingly popular field of study in the scientific community. The compact size and multi-particle nature of laser-based accelerators make them appealing for a wide range of applications, from astrophysics to medical science. However, the potential of laser-driven radiation sources for elemental analysis of materials has not been thoroughly explored. This thesis aims to assess the feasibility of neutron production using laser-driven particle acceleration for materials characterization. The work provides a detailed description of neutron production using laser plasma acceleration, focusing on fusion and portable laser-driven acceleration in the target normal sheath acceleration (TNSA) mechanism. The neutron-in and gamma-out reactions are explored using ${}^{2}_{1}$d(d,n)${}^{3}_{2}$He, ${}^{7}_{3}$Li(p,n)${}^{7}_{4}$Be, ${}^{7}_{3}$Li(d,n)${}^{8}_{4}$Be nuclear reactions. The neutrons produced from these nuclear reactions are used to characterize the target object for material identification. Geant4 simulations were performed to evaluate the feasibility of laser-driven neutron sources for materials characterization. The simulation was first conducted with a laser-driven neutron source, then with a radioactive neutron source to obtain results for a proof-of-concept experiment in the laboratory. The results of the study confirm that materials characterization can be performed using neutrons produced from laser facilities. The predictions made using a ^{252}Cf neutron source indicate that it is a valuable interrogation source, emitting high-energy correlated neutrons and gammas. However, the major limitation of this source is that it cannot be turned off, emitting radiation continuously. As a result, its use is limited to small experiments that rely on a constant neutron flux without pulsed emission. In this regard, laser-driven fusion neutron sources are more practical as they lack intrinsic gamma-neutron correlations and can be turned on and off as needed.

List of Figures

List of Tables

Contents

List of acronyms

CT	Computed Tomography
PMT	Photomultiplier
NaI	Sodium Iodide
FoM	Figure of Merit
SF	Spontaneous Fission
FTNA	Fast and Thermal Neutron Analysis
ToF	Time of Flight
SNM	Special Nuclear Material
LaBr	Lanthanum Bromide
LWFA	Laser Wakefield Acceleration
TNSA	Target Normal Sheath Acceleration
PSD	Pulse Shape Discrimination
HV	High Voltage
NRF	Nuclear Resonance Florescence
MC	Monte Carlo simulation
FPGA	Field Programmable Gate Array
PSD	Pulse Shape Discrimination
TEU	Twenty Equipment Unit
DPP	Digital Pulse Processing
ADC	Analog-to-Digital Converter
INFN-LNL	National Institute of Nuclear Physics-Legnaro
PCB	Printed Circuit Board

Chapter 1

Overview of the problem

1.1 Introduction

Terror attacks are a significant threat now and will only get worse. Such a threat poses a particular risk to the transportation infrastructure. It is possible to make attempts to disguise the loading of weapons, explosives, special nuclear materials (SNM) and illicit drugs onto a ship or into an aircraft in order to convey them to a different location (for instance, hidden in a cargo container). Container traffic accounts for over 85 million TEU (Twenty Equipment Unit) equivalent in 2018, accounting for a fourth of the gross mass handled by the EU's 20 largest ports. It is the most dangerous mode of transport for illegal contraband. Customs inspection is the first authority at the border, with an increased focus on security, and are legally responsible for enforcing EU import and export legislation to and from non-EU nations. In recent years, the necessity of custom control has been emphasized for goals such as security and safety (i.e., smuggling, drugs, cigarettes, firearms, counterfeited items), as well as environmental protection [1,2].

In today's logistics chain, containers are the most efficient ways to transport goods around the world. They travel swiftly and at a low cost, making them an excellent option for developing legal or criminal businesses. Therefore, border inspection services are more focused on container inspection. In this instance, the conventional or standard approach has been used, which includes choosing suspect cargo using unreliable indirect means (documentation inspections, intelligence service information). Only a small portion of the selected cargoes (which are chosen pretty arbitrarily in any case) are sent for additional examination due to the technical issues and the lack of the necessary equipment. This circumstance has a number of negative implications: It places a multifaceted strain on the officer, perhaps leading to decisions based on results that are prone to erroneous positive and negative conclusions, each with significant consequences. Current inspection systems result in a significant percentage of economically unfavorable false positive referrals, as well as the occasional unacceptable threat being missed [1,2].

The aforementioned issue is becoming increasingly important while also pursuing the fight against international organized crime, such as the smuggling of drugs, precursors to drugs, weapons, precursors to explosives, and other items. Customs border checks have long benefited from detection technology to allow lawful trade employing modern non-intrusive inspection systems and developing automated image processing skills to achieve high performance. It makes easier to find dutiable, prohibited, and restricted objects and commodities. For this purpose, the detection of sophisticated smuggling scheme in the logistical flow, requires sensitive detection techniques that can be operated in the first-line of inspection.

1.2 Explosives and Illicit Materials

There are numerous explosives and illegal materials which can be mixed and diluted to create countless varieties, the majority of which are made up entirely of elements H, C, N, and O. These materials differ significantly from most conventional materials by one or more elemental characteristics. A stacked bar graph representing the proportion of each constituent atom in various explosives, illegal substances, and other miscellaneous materials, is shown in Fig. 1.1. As can be seen, explosives may be identified by their relatively high nitrogen and oxygen contents and relatively low carbon and hydrogen contents. Contrarily, illicit drugs contains low proportions of nitrogen and oxygen and being rich in carbon and hydrogen. The majority of explosives have densities between 1.2 and 2.0 g/cm^{-3}, which is frequently more than the majority of common HCNO compounds. These characteristics may be used to detect explosives and illegal narcotics concealed among the other materials within a closed container [1].

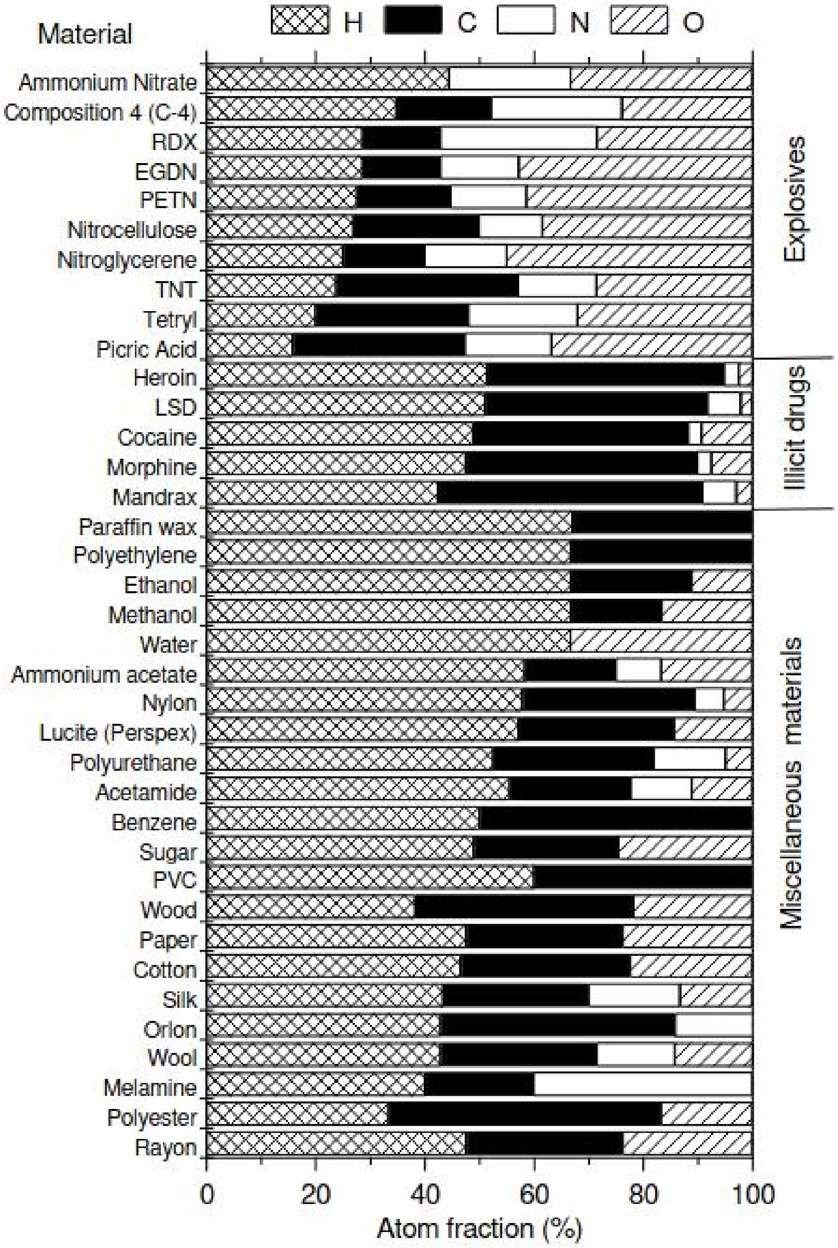

Figure 1.1: Percentages of atomic fractions of elements HCNO that makes up various explosives, illicit drugs and other common miscellaneous materials [78]

.

1.3 Detection Technologies of Illicit Materials

The detection of special nuclear and illicit materials are always been the top priorities because they are:

(a) Oftenly used as a terror attack tool.

(b) Can be purchased or made from readily accessible components.

(c) Can be moved to a target location and are reasonably difficult to detect.

The control of these materials in cargo containers are based on a number of detection techniques, which can be categorized into the following classes.

1.3.1 X-ray Detection Technology

The 1970s saw the development of X-ray and γ-ray scanning for the detection of hazardous objects. Images with good resolution and penetration depth can be produced by modern X-ray equipment. Many explosives detection devices are based on x-ray techniques that assess material x-ray attenuation. Energy, density, and average atomic number all influence attenuation. Because X-rays predominantly interact with electrons, the attenuation coefficient is highly associated with the electron density of the substance under investigation [3]. The X-ray inspection system have been used to identify the most commonly used elements in explosive substances and it was found that they have densities higher than 1.4 g/cm^3 [3]. The efficient systems for detection of materials nowadays using X-ray screening systems includes:

(a) X-ray transmission radiography

(b) X-ray computer tomography (CT)

X-ray radiography, a typical imaging technique, is a collection of two-dimensional x-ray attenuation line integrals. but this approach is incapable of resolving the third dimension along the incident x-ray path [2]. CT is a sophisticated X-ray technology that can reconstruct cross-sectional pictures of an object from several X-ray projections. By using tomographic reconstruction of two-dimensional cross-sectional images and then three-dimensional volumes can greatly enhance the detection of suspicious materials like explosives by identifying certain shapes or patterns, such as wires, batteries, or detonators, as well as by measuring the volume of material [2].

High-energy x-ray based detection system has been developed for identifying illicit materials and explosives on seaports, airports, and at land border crossings. High energy radiographic equipments uses a highly radioactive γ source, such as ^{60}Co or ^{137}Cs, from a linear accelerator with an energy of 2.5–6 MeV, can pass through the loaded container and produce a radiographic image of the contents inside. However, this technology is not efficient to automatically distinguish between dangerous and safe materials [2]. Combining transmission and backscatter x-ray measurements increases identification of light (low Z) materials common in explosives; nonetheless, it does not particularly identify explosives. Dual-energy CT (computed tomography) may offer geometrical and physical density and atomic number information. Effective atomic number cannot completely characterize a material, but it may give more discriminating than physical density alone [3].

1.3.2 Neutron Detection Technology

James Chadwick discovered neutrons in 1932, and they are charge neutral subatomic particles. Their practical value was quickly realized following their discovery. H. Kallmann and E. Kuhn used a tiny neutron source to conduct the first neutron radiography experiment in 1935 (Bilheux, McGreevy, and Anderson 2009) [4]. More applications have emerged as a result of decades of research and development. Neutron sources are now routinely employed in a wide range of applications, making them a necessary tool in both research and industry, i.e., neutron interrogation technqiues for homeland security purposes and neutron cancer therapy. It is particularly well adapted to structural and functional aspects involving light atoms because of its capacity to analyze matter exclusively through nuclei contact [4].

A wide range of important items can be found using neutron-based inspection systems, from risks to national security to custom duties and environmental protection. In principle, when a neutron hits an object, it can start one of many nuclear reactions with the chemical elements that make up the object. Most of the time, these reactions cause the emission of γ-rays with characteristic and unique energies. These γ-rays are like the 'fingerprints' of the elements contained in the object. By counting the number of γ-rays emitted with a certain energy (e.g. the γ-rays from carbon), one can figure out the amount of the element contained in the object. If an object is hidden among other innocuous materials, the identification takes place through the correlation of various chemical elements observed, coupled to the information about the innocuous material itself. Therefore, neutron interrogation is useful for large vehicles like cars, and containers due to the penetration of fast neutrons as probes and the fission neutron and γ rays as signatures [2, 4]. The schematic design of this process is shown in Fig. 1.2.

Neutrons are very penetrating particles. Their intensity is not effected by thickness of typical containers. To a smaller extent, the outgoing γ-rays are also very penetrating, and easily excites the interrogated volume to be detected by an appropriate set of detectors placed outside the object. This technique is non-destructive and non-intrusive (interrogation may occur from a distance of several centimeters) due to the low radiation dose absorbed by the interrogated object [5]. Neutrons of various energies may be required, depending on the chemical elements that one wants to measure. Many of the existing neutron-based applications rely on radioisotopic sources (Am-Be, ^{252}Cf) to produce neutrons. These sources have neutron capture processes that may excite a variety of chemical elements (H, C, N, O, etc.) with energies of few MeV greater than those provided by radioactive sources. This calls for a neutron source that can generate the high energy neutrons needed to test these elements. A radioisotope or a small accelerator, along with a moderator to control the neutron energy, can be used to obtain it. This technique is called "neutron in-gamma-out" reactions. It can be done with both fast/thermal neutron analysis (FTNA). A thermal neutron source, which produces low energy neutrons, while fast neutrons are high energy neutrons. High energy neutrons interact with an element's atomic nuclei in a slightly different way than low energy neutrons. Depending on the size and density of the material, either a thermal neutron source or fast neutrons can be better suited [1, 5].

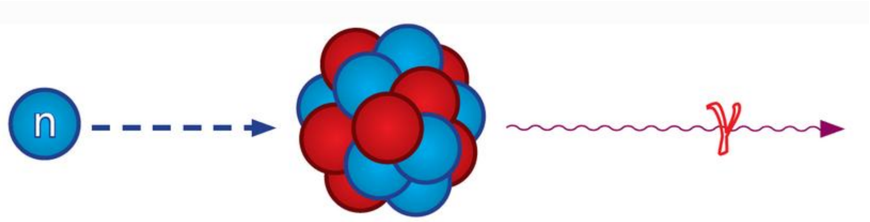

Figure 1.2: Schematic view of "neutron in-gamma-out" reactions

.

1.4 System for simultaneous detection of hazardous and illicit materials - Possible solutions

As we discussed earlier, there is currently no ideal system that fully satisfies the demands of homeland security while also being economical for cargo inspection. The current technology is either a time-consuming process involving multiple types of scanners, and are extremely expensive, or does not produce trustworthy inspection outcomes. Therefore, a detecting system with the following characteristics is clearly needed.

(1) Universality, or the capacity to identify the main categories of dangerous items: weapons (including both firearms and improvised explosive devices), explosive and radioactive materials (isotopes), and special nuclear and illicit materials.

(2) Effectiveness, or compliance with international standards regarding the validity of inspection findings.

(3) Adjustability, or the ability to be installed in different environments, especially in situations where there is a lack of space and time.

In our opinion, the development of an integrated system combining the best features of the most cutting-edge technologies, namely X-ray analysis, which provides high-speed monitoring and identification of suspicious objects and areas, and neutron analysis, which provides high selectivity and precise identification, would be a natural step towards the accurate detection of illicit materials in cargo's of various space dimensions. It will be able to avoid scanning all items when in active interrogation mode, reducing inspection time. Additionally, it helps to clear the whole container through a single system assessment. Companies researching neutron analysis technologies developed integrated systems for the hand luggage inspection of flying passengers which gave them solid in-field practical experience [6]. For instance, Ratec EDS-5101C system has been developed and proved as an integrated solution for the detection of explosives, radioactive hazards, and SNM for luggage inspection [6]. Since then, via in-depth field research, it has become clear that ideal solution for a cargo inspection system should be taken into account as an integrated approach based on the fusion of several inspection systems [2].

In order to enhance universal development in cargo inspection and detection system, a 3D X-ray scanning employing a laser-plasma generator is a prime candidate to fill the gap because it opens up avenues towards extraction of higher-quality information from the container inspection by using advanced automated image analysis strategies. Thus, the MULTISCAN 3D Project which is an X-ray screening (Tomography) system based on innovative electron acceleration technologies for X-ray production, 3D reconstruction for multi-view configurations, data processing, detectors, and X-ray source monitoring. X-rays and neutron radiation are used in the novel laser-plasma sources, used for non-intrusive scanning of maritime containers to detect terrorist threats. It employs nuclear resonance fluorescence, photo fission and interactions based on spectral neutron attenuation to non-intrusively identify substances at locations in the container flagged as anomalies. Nuclear resonance fluorescence, photo fission and interactions based on neutron irradiation technologies signal the presence of a certain group of atoms each. Ratios between the atom may give rise to actual substance identification. First line anomalies identified as probable false – positive in non-intrusive second line of inspection and may result in the container being released without physical inspection. Results with a probability of being true - positive will trigger follow-up activities to take place.

1.5 Multiscan3D Project - Laser Plasma Based Inspection Technique

The MULTISCAN3D project aims at exploiting the opportunities provided by the laser-plasma acceleration technology. A schematic view of this emerging concept and main technical functions are provided in Fig. 1.3 to demonstrate the MULTISCAN3D idea. It can be seen that particle source is compound of a laser system and a laser-plasma interaction chamber where electrons or ions are accelerated and converted into X-rays, neutrons, gamma-rays. Some monitoring is required to check the good operation and to help the data treatment. After crossing through the cargo, particles are detected, and the data processing led to CT reconstruction or chemical identification.

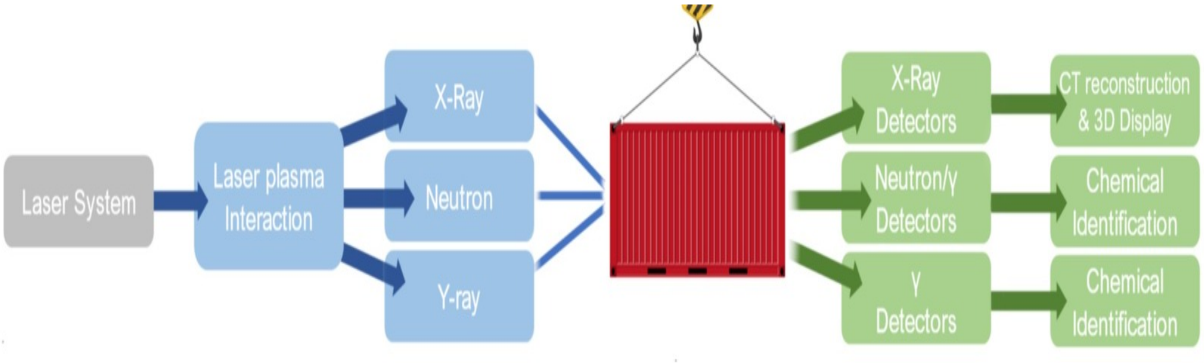

Figure 1.3: General scheme of MULTISCAN3D project.

This project will investigate the capability of the laser-plasma technologies to produce several other types of radiations including X-rays, γ-rays, and neutrons. It opens to the possibility of providing customs with an all-in-one first- and second-line system for containers and large trucks. In this concept, the main mechanical displacement is the translation of the cargo through a ring which includes the ring of detectors and a set of plasma interaction chamber in which the X-rays and neutrons are produced, It leads us to a concept of static cargo inspection shown in Fig. 1.4.

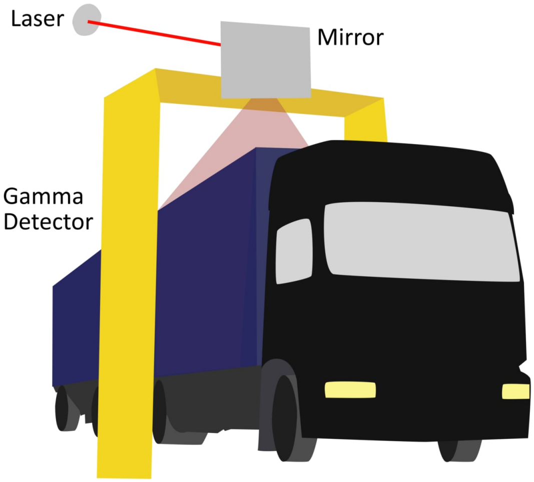

Figure 1.4: Schematic view of a static cargo scanning based on laser-plasma X-ray/neutron production. The cargo is passing through a ring of detectors, itself surrounded by plasma/X-ray interaction chambers

.

Former studies have demonstrated the feasibility of detecting fission neutron and gamma coincidences with induced tagged fast neutrons of 14 MeV with an associated particle neutron generator and EJ-200 plastic scintillators. This method has shown limitations for rich-in-hydrogen cargo like organic materials (wood, paper, clothes, plastics, food, etc.), which strongly attenuate the interrogating fast neutron beam. A high intensity laser-driven pulsed neutron interrogation would allow inducing a sufficient number of fissions, both with fast neutrons during the pulses, and with thermal neutrons moderated in the rich-in-hydrogen goods, between the pulses. Detecting hidden materials in cargo containers by means of neutron interrogation is a valuable complement to photofission and nuclear resonance fluorescence (NRF) inspections. Indeed, combining different technologies increases the detection confidence level and allows addressing a wider range of configurations in terms of cargo cover loads (neutrons and high-energy photons being respectively attenuated by low-Z and high-Z materials).

This project is based on photofission and the NRF technique using Geant4 simulation tests to design their measurement setups. Then, the setups will be tested under irradiation constraints in laboratory. The designed setups could then be optimized before performing experimental tests using the laser-driven neutron beam. Photofission measurements uses samples of depleted uranium. NRF measurements uses samples of various light nuclei materials. For both techniques, the operating concept would be focused on the forward-peaked laser-driven neutron beam onto a suspect area of the cargo container (e.g. dense and low-Z items for explosives, or very dense and high-Z items for SNM). The broad energy spectrum of the neutron beam offers the possibility to implement neutron transmission spectroscopy in the few MeV energy range. The transmitted neutron spectrum across the cargo container is measured by the time-of-flight (ToF) triggered by the short (ns) laser-driven neutron pulse. The attenuation of the incident spectrum at specific energies (i.e. specific ToF) corresponding to absorption cross section resonances of the elements constituting elements i.e., HCNO gives information on the material composition.

In this thesis, we will focus on elemental identification in the view of explosive detection by fast and thermal neutron interrogation system. It will be investigated using numerical Geant4 simulation in order to determine its viability and applicability to cargo containers. Experimental validation of the calculations will be carried out based on proof-of-principle laboratory experiments with ^{252}Cf neutron source. The performances for cargo container inspections will be extrapolated using Geant4 simulation for radioactive ^{252}Cf neutron source and laser driven fusion neutron sources.

The main part of our thesis describes neutron generation, which includes radiation process and nuclear reactions, to understand the important background knowledge. Here, the details of remaining chapters are given below:

Chapter 2 will be based on the different laser driven neutron processes.

Chapter 3 “Scintillation Detectors”, starts with an introduction to the scintillation detectors. Types of scintillation detectors and their scintillation mechanism are discussed in separate sections. After that, a general description of the Digital n-γ Pulse Shape Discrimination (PSD) in organic and inorganic Scintillators is given in order to help the readers to understand the discrimination methods for neutron and gamma detection.

Chapter 4 “Experimental Setup”, reports an experimentation, methods and instruments used in laboratory.

Chapter 5 “Geant4 Simulation”, will present the simulation performed for an experimental campaign in detail.

Chapter 6 “Result and Discussion” to describe the comparison between simulation and experimental tests for ^{252}Cf source, fusion and compact laser driven neutron sources.

In the Appendix, Geant4 Simulation codes are presented.

Chapter 2

Neutron Production and Sources

2.1 Introduction

Neutrons play a crucial role in determining the stability and behavior of atomic nuclei in nuclear physics. The mass and charge of a nucleus are determined by the number of protons and neutrons, and isotopes of the same element can have different numbers of neutrons. The stability of a nucleus also depends on the ratio of protons to neutrons, which affects the types of nuclear reactions that can occur. Neutrons can induce nuclear reactions either by colliding with atomic nuclei or by being absorbed by them. This makes neutrons useful for a wide range of applications, including nuclear power, radiation therapy, energy production, imaging technology, and many other scientific research. The increasing interest in neutrons over time has led to the research of more efficient neutron sources.

This chapter explores the properties of neutrons, nuclear physics of neutron generation, and various sources of neutron radiation in nuclear physics. By understanding these concepts, we can better appreciate the potential of laser-driven neutron production systems, which will be discussed in more detail later in this thesis.

2.2 Properties of Neutrons

The atomic nucleus is composed of both protons and neutrons, which are commonly referred to as nucleons due to their similar behavior and masses within the nucleus. Although a free neutron is slightly heavier than a proton, it is not stable and decays according to a β^- scheme with a mean lifetime of 881.5s= 14.7min:

$$n \rightarrow p + e^- + \bar{\nu}_e \tag{2.1}$$

where p indicates a proton, e^- an electron and $\bar{\nu}_e$ an electronic antineutrino.

Internal structure of neutron is made up of quarks, specifically one up quark (charge +2/3 e) and two down quarks (charge -1/3 e), which explains why it has zero net electric charge, zero electrical dipole moment, and zero electrical polarizability. Neutrons are a member of the hadron family and, more specifically, the baryon family. Their quark structure also explains their magnetic behavior and spin, despite having zero net electric charge [79].

The concept of a neutral particle had been proposed much earlier by Rutherford before James Chadwick discovery at the Cavendish Laboratory in Cambridge. The discovery of neutrons earned Chadwick a Nobel Prize in physics in 1935. Table 2.1 provides a summary of the physical properties of neutrons, and table 2.2 categorizes neutrons based on their energy. Although experiments continue to be performed to test the neutron's electrical properties, the measured values for these quantities correspond to the experimental lower limits [79].

S.No	Parameter	Values
1	Mass	m$_n$ = 1.009u = 1.675×10^{-27} Kg
2	Composition	Quarks: 1 up, 2 down
3	Mean lifetime	881.5 s
4	Spin	1/2
5	Magnetic moment	µ = -1.913 μ_n = -0.966×10^{-26} J/T

Table 2.1: Main properties of neutrons [79]

S.No	Classification	Energies
1	Cold neutrons	E < 0.025 eV
2	Thermal neutrons	E = 0.025 eV
3	Epithermal neutrons	0.025 eV < E < 1000 eV
4	Fast neutrons	E > 1000 eV

Table 2.2: Neutron classification according to their energy [79]

2.3 Nuclear Physics of Neutron Generation

The most significant nuclear reactions that result in neutron emission, as well as how neutrons interacts with other materials and the effects that result, will be covered in this section.

2.3.1 Neutron Production by Direct Nuclear Reactions

To produce neutrons, the reaction mechanisms are classified based on the delay between an interaction and emission of neutrons. Direct nuclear reactions normally occur in a time frame on the order of 10^{-22}s, which is comparable to the amount of time required for an ion to pass through the nucleus. This type of reaction, where projectile can shatter the target nucleus into pieces, This mechanism is known as inelastic scattering. These reactions exhibit a significant neutron emission forward orientation while not producing a compound nucleus. Two direct reactions, which are extensively discussed, play major roles in the neutron generation for deuteron projectiles.

The most frequently discussed reactions below 100 MeV in the context of neutron creation is deuteron break-up. Deuteron break up refers to the dissociation of deuteron in presence of an electric field of a target nuclei. It can be compared to the deuteron rapidly decelerating in the nucleus' field in a classical sense. The proton is affected by the decelerating force, but the momentum is kept by the neutron forces' inertia. The proton and neutron split if a force is applied that is greater than the binding force that holds them together, and the neutron then moves forward with the momentum it had before splitting. Since in 1963, deutreon break-up cross section was theoretically measured by Gold and Wong using perturbation theory, and dipole approximation via equation 2.1.

$$\sigma = \int_0^\infty \frac{16\hbar^2}{3m} n_1^2 \frac{\epsilon_0^{\frac{1}{2}} \epsilon^{\frac{3}{2}}}{(\epsilon + \epsilon_0)^4} ln(\frac{2n_1}{n_2 - n_1}) d\epsilon \tag{2.2}$$

where as,

$$n_1 = \frac{Ze^2}{\hbar |v_1|}, n_2 = \frac{Ze^2}{\hbar |v_2|} \tag{2.3}$$

Here, Z is the atomic number of the target nucleus, $\hbar$ is the Planck's reduced constant, m is the mass of the nucleon, and v_1 and v_2 are the initial and final velocities of the deuteron's internal center of mass in relation to the potential center. The binding energy (ϵ_0) of the deuteron is equal to 2.225 MeV and ϵ is the internal disintegration energy of deuteron.

It is clear from this equation that the cross section of the target nucleus's breakup rises quadratically. We may get the cross section of the neutron yield of deuteron beams on low Z target materials. For deuteron energies more than 25 MeV, this phenomenon results in large cross sections for catcher materials with a high Z number. The coulomb potential, however, is relatively modest for materials with low Z when compared to the ion energies. This leads us to the low break-up cross section and enables strong nuclear force interactions as the deuteron can approach closer to the nucleus. It makes the deuteron stripping processes more likely. As a result, the deuteron and the target nucleus' wave functions begin to overlap. While the other half of deuteron keeps its momentum in that condition, either the proton or the neutron can combine with the target to produce a compound nucleus. This stripping cross section is crucial for neutron production with low cut off energy since it may produce deuterons with energies between 3 and 4 MeV.

2.3.2 Compound Nuclear Reactions

The production of neutrons in a single nuclear reaction characterizes the previously described direct nuclear reactions, whereas several nuclear interactions makes up compound nuclear reactions. Niels Bohr proposed his unified field theory in 1936, which states that after a nuclear exchange, the resulting compound nucleus can be distinguished solely by the number of its nucleons and its energy level. On a nuclear scale, these states last considerably longer, on the order of 10^{-16} s to 10^{-18} seconds, allowing the nucleus to achieve thermal equilibrium. As a result, there is no favored direction for neutron emission and all information about the entrance channel is lost. The decay of compound nucleus only depends on excitation energy and probability of its decay channels. The neutrons spectrum emitted from these reactions by evaporation is shown in Fig: 2.1.

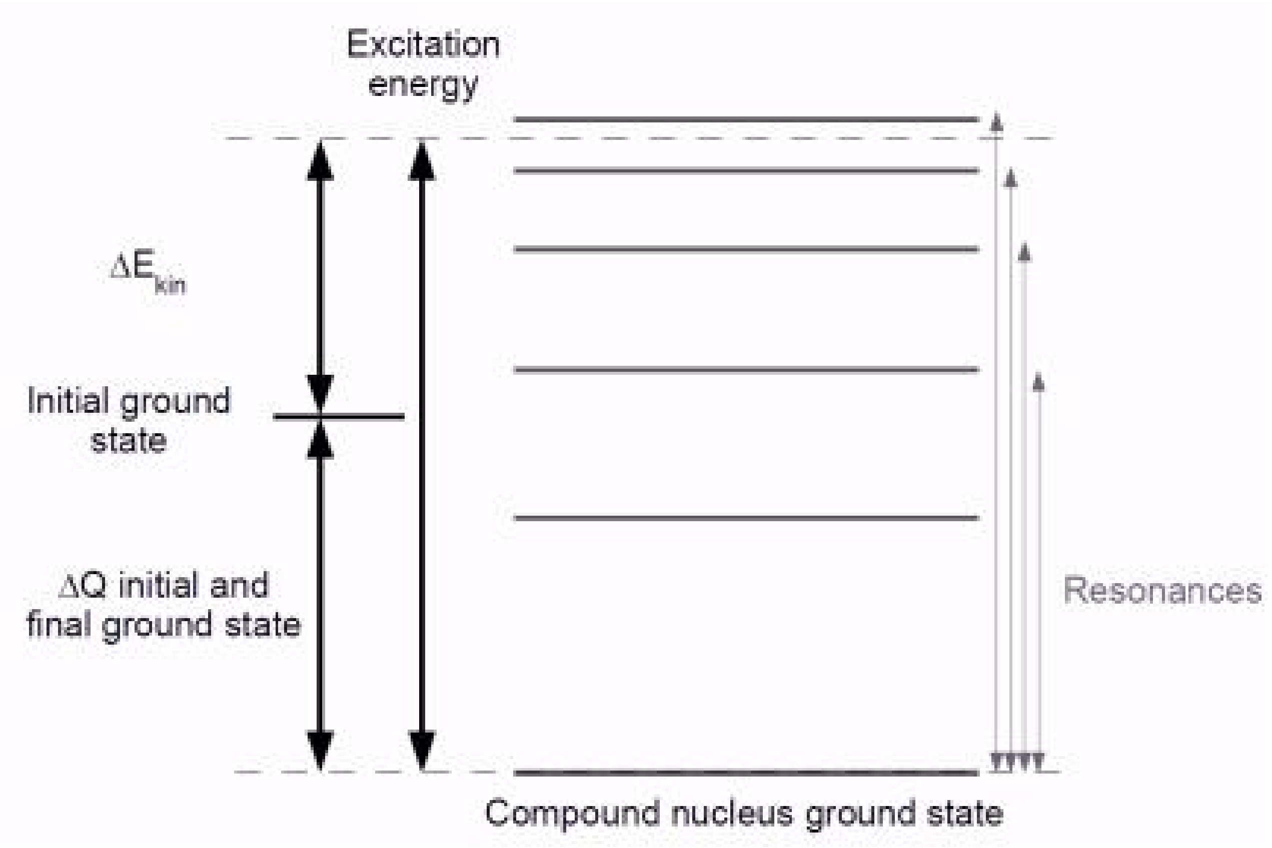

Figure 2.1: Following the creation of a compound nucleus, excitation states occur. The compound's energy state is sum of both its kinetic energy and the energy added from lower ground state. When the sum of E_{kin} and ΔQ becomes equal to new excited state of the compound, then a resonance is formed

.

The term "pre-equilibrium reaction" describes the phase at which neutron emission occurs but the nuclei have not yet attained their thermal equilibrium. It can happens when the projectile energy is greater than the binding energy. In this case, the information of an entry channel is partly maintained and the emitted neutrons will have a stronger forward direction.

Discrete quantum states are predicted by the laws of quantum mechanics for compound nuclei. Fig 2.1 depicts these stages in schematic form. It demonstrates that if the energy of the ground state plus the kinetic energy of an ion equals an excitation state of the generated compound nucleus. This reaction cross section grows, and resonance occurs. These resonances are very unique to each isotope as well as the incoming particle and may be used to identify materials.

2.3.3 Neutrons Propagation In Materials

The microscopic reaction cross section σ may be thought of as the effective surface area of the nucleus for a specific reaction. The bigger the surface area, the more probable it is to be struck by a neutron and undergo a reaction. A material's total cross section is the sum of the cross sections of all accessible reaction channels σ_r.

In classical terms, for a particular reaction, the microscopic cross section σ may be interpreted as the apparent surface area of the nucleus. Increasing the surface area increases the probability that a neutron will strike it, causing a reaction. Total cross section of material is equal to the sum of its individual reaction channel cross sections σ_r given as:

$$\sigma = \Sigma_r^n \sigma_r \tag{2.4}$$

σ shows probability of interaction with a nucleus. The macroscopic cross section is used to determine the interaction rate within a material as a product of the number of nuclei per unit volume given by atomic number density N_i with a microscopic cross section σ:

$$\Sigma_i = N_i \sigma_i \tag{2.5}$$

N_i being the density of atoms in the material and can be calculated by:

$$N_i = A_v f_i \frac{\rho}{M} \tag{2.6}$$

Where ρ is the density of a substance and A_v is the Avogadro constant. If the molecular composition of a material is H_2O, then M is the molecular weight and f is the percentage of nuclei of type i within the substance.

2.4 Conventional Neutron Sources

Neutron sources are typically classified according to the mechanism by which neutrons are produced. Conventional neutron sources use either fission or spallation nuclear reactions to generate neutrons in nuclear confinement by which nuclei breaks apart. Modern continuous and pulsed neutron sources typically employ these reactions.

2.4.1 Fission Neutron Sources

Fission reactions occur when a heavy nucleus, such as uranium or plutonium, is split into two lighter nuclei by absorbing a neutron. This process releases a large amount of energy, as well as several neutrons. These neutrons can then be used to induce further fission reactions, creating a chain reaction. Fission neutron sources are typically reactors, which are designed to sustain a controlled chain reaction. These reactors are using the fission of the uranium isotope ^{235}U. Following the capture of a slow neutron, this nucleus is deformed and is split into two fragments, simultaneously releasing 2 or 3 on average 2.45 neutrons are emitted called to as “prompt” neutrons [33] shown in Fig. 2.2, following an evaporation like spectrum proportional to:

$$N(E) = E^{\frac{1}{2}} \exp \frac{-E}{T_n} \tag{2.7}$$

$$^{235}U + neutron \longrightarrow fission fragments + 2.45 neutrons + 180 MeV. \tag{2.8}$$

Where, $T_n = 1.29$ MeV. Each of the emitted neutrons can cause the fission of another 2-3 nuclei, so that each of them will also emit more 2 to 3 neutrons, and so on as shown in Fig. 2.2. This process is called the chain reaction.

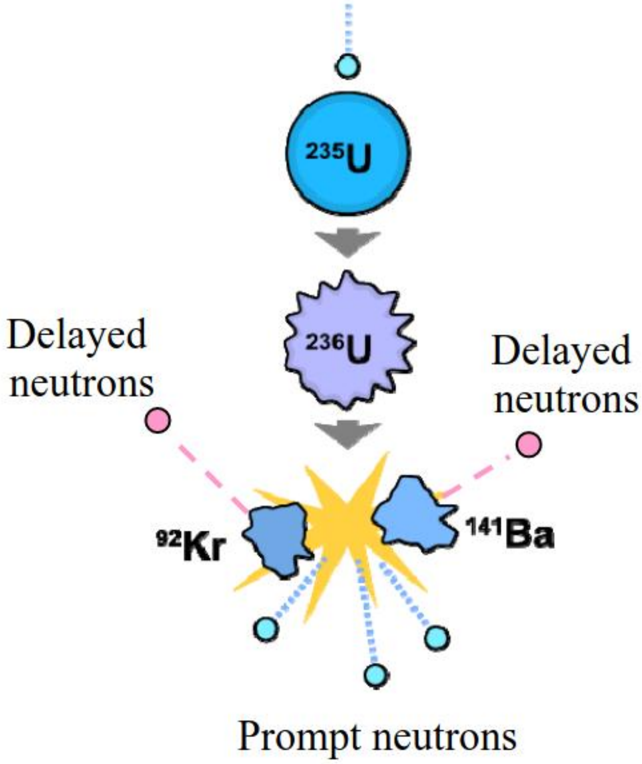

Figure 2.2: Schematic representation of the fission process of U-235 [89]

In addition to fission reaction, delayed neutrons play a critical role in sustaining a stable neutron flux in nuclear reactors. These neutrons are emitted by fission fragments as part of their radioactive decay and account for only a small fraction of the total amount, approximately 0.64%. However, their average time delay of a few seconds is crucial in controlling the chain reaction, allowing the reactor to be sub-critical for prompt neutrons to prevent uncontrolled multiplication. The delayed neutrons can sustain the reaction just in time when it is about to die out, enabling the reactor to reach criticality. Control rods made of neutron-absorbing material such as boron are used to moderate and adjust the number of slow neutrons, ensuring a self-sustaining chain reaction. This mechanical control system is simple and reliable, making it effective in regulating the nuclear reaction [89]. Fig. 2.3 illustrates the scheme of controlled chain reaction in the nuclear reactor.

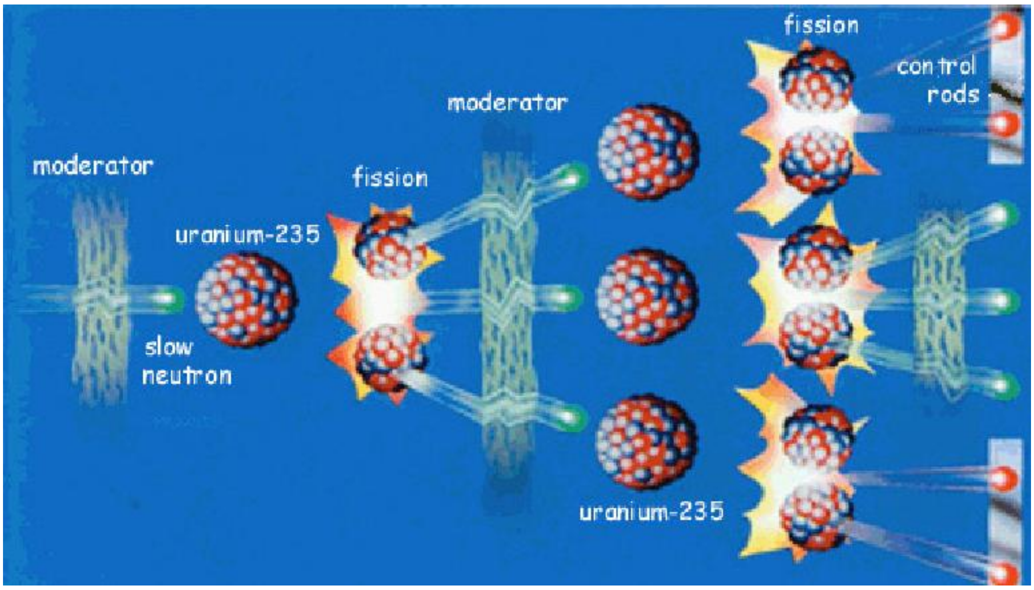

Figure 2.3: Schematic view of controlled chain reaction in the nuclear reactor, where the number of slow neutrons is reduced to the minimum required for a self-sustaining chain reaction using control rods. The position of the control rods can be adjusted to allow the reaction to remain critical only with the delayed neutrons emitted a few seconds after the initial reaction [89]

In a nuclear reactors large number of neutrons can be produced, making them useful for a wide range of scientific and industrial applications, including materials science, biology, and nuclear energy production. The Training, Research Isotopes General Atomic (TRIGA) reactors are the most prevalent kind of reactor-based neutron sources [9,12]. The TRIGA MARK II reactor LENA in Pavilia operates at 250 kW power [34]. It is capable of producing 1 × 10^{13} n/(cm^{2}s) inside the reactor core in the thermal regime during steady-state operation. In pulsed mode operation it can generate up to 1.1 × 10^{16} n/cm^{2}s) [35]. Pulsed mode is used to characterize reactor pulses in this context, which are significantly longer than the neutron pulses at an LDNS or a spallation source and are on the order of ms. These neutron sources have the drawback of producing nuclear waste and operating with the recognized dangers of nuclear reactors [9,35].

2.4.2 Spallation Neutron Sources

Spallation neutron sources are high energy accelerator-based system that can generates pulsed neutron beams by shooting a target with an intense proton beams ranging from hundreds MeV to a few GeV [32]. The target materials for spallation neutron generations includes thick high-Z target to induce endothermic reactions of threshold energy equals to 100 MeV. Common materials for spallation targets are Pb, W, U or Hg.

Among the most well-known spallation neutron source facility is the Los Alamos Neutron Science Center (LANSCE) [30]. In this mechanism, Secondary particles such as protons, neutrons, and α particles are released from the nucleus when the protons are accelerated to the GeV regime and directed onto a high-Z converter material and cause nuclear reactions in neighboring nuclei. This mechanism is known as an inter-nuclear cascade reaction of highly energetic hadrons such as p, n, and pions with energies greater than 20 MeV generates neutrons primarily via the evaporation of the nucleus; as a result, between 20 and 30 neutrons are released for every incoming proton [9]. This reaction channel emits neutrons with a spectrum by following the Maxwellian distribution [9], and is characterized by two main components. First, strongly forward-collimated neutrons with energies up to 100 MeV are generated by direct hadronic interactions between impinging protons and target nuclei. Second, hadronic bombardment creates a pre-equilibrium excited nucleus. Using pre-equilibrium fission, the nucleus may dispose of extra energy if its fission barrier is comparable to its temperature. If not, the nuclear evaporation process activates, and results in emission of particles of energies lower than 20 MeV. In this process, an isotropic distribution of 2 MeV neutrons are produced. Nuclear evaporation is complex and many process can occurs. In first place, light nuclei emits radiations such as β and γ rays. Some debris nuclides including ^{8}He, ^{9}He and ^{11}Li may β-decay, and emits monoenergetic neutrons of energies in KeV. Furthermore, photoneutrons may be produced by the interaction of γ radiation with ^{2}H and ^{9}Be present in the surrounding material. These photons originate from the de-activation of target nuclides or from β-decay of light spallation products. A schematic view of neutrons production in spallation process is shown in Fig. 2.4.

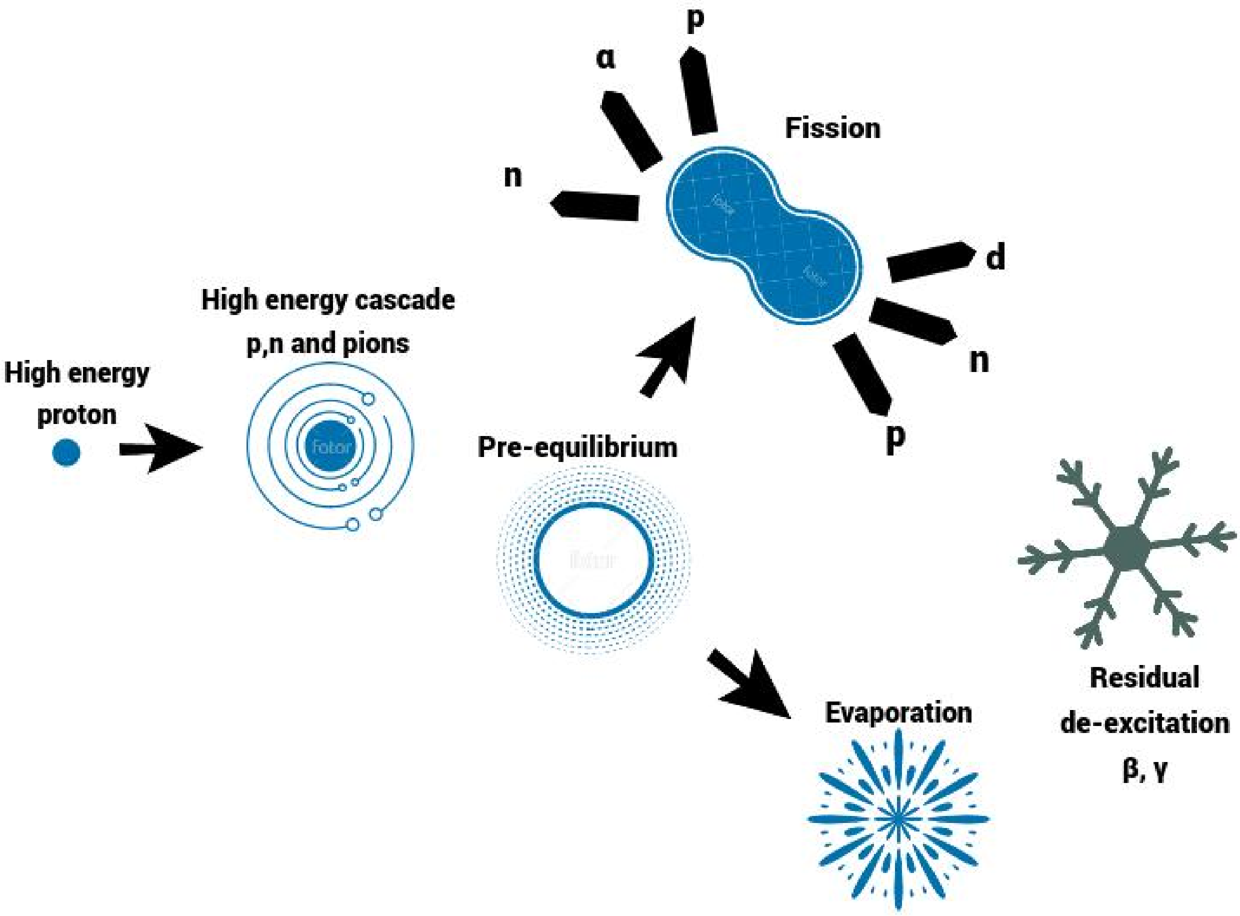

Figure 2.4: Schematic view of spallation process. Initial effect causes high energy nuclear cascades to the emission of particles with energies closer to the energy of incident particle. Later processes includes pre-equilibrium, fission and evaporation processes, which cause the emission of low energy particles and the formation of daughter nuclei.

These neutrons are hard to shield, hence a massive quantity of attenuation material is required. Several meters of concrete, high-Z materials for reflection and γ attenuation, and enormous amounts of moderation materials like as polyethylene or water are included. As a result, the size and expense of these sources significantly increases [9]. The most common form of neutron source is a spallation source. The thermal peak neutron flux at the source was about 10^{17} n/(cm^{2} s) [9]. The high investment and operating costs restrict the number of global operational spallation sources to a small number, and only crucial key experiments can be undertaken since the total amount of available beamtime is limited.

2.5 Other Neutron Sources

In addition to conventional neutron sources based on fission and spallation, there are several other mechanisms by which neutrons can be produced. These sources may offer advantages such as higher intensities, faster time scales, or smaller sizes.

2.5.1 Radioactive Isotope Sources

The radioactive isotopes are the smallest class of neutron sources [58]. By combining the element beryllium with the emitter polonium, neutrons were first discovered in the year 1936. For the purpose of producing neutrons using isotopes nowadays, most Americium-Beryllium (AmBe) or ^{252}Cf sources are employed for neutron production via isotopes. Californium is a natural neutron emitter, with a half-life of 2.645 years, governed by α emission of 96.9% (forming helium gas and the isotope ^{248}Cm) and provides neutron energy spectrum by 3.1% spontaneous fission of ^{252}Cf atoms. It emits 3.768 neutrons per fission on average. Decay process of ^{252}Cf is based neutrons, alpha particles, and gamma photons. Basic characteristics of ^{252}Cf are listed below in table 2.3.

^{252}Cf decay characteristics		
S.No	parameter	Value
1	Half-life (effective: α and SF)	2.645 y
2	Half-life (spontaneous fission)	85.5 y
3	Decay mode	α (96.91%), SF (3.09%)
4	Alpha energies	6.076 and 6.118 MeV

Table 2.3: ^{252}Cf decay characteristics.

The principal advantages of using ^{252}Cf neutron source is its availability with high-intensity, its dependability, and unlike a reactor, it can be operated cheaply for nondestructive testing applications of many materials using thermal and fast neutron transmission radiography technique with its small geometric size [37,38].

AmBe (Americium-Beryllium) neutron sources are a common type of sealed neutron source used for industrial and research purposes. They use a small amount of americium-241 and beryllium to produce neutrons through a (α,n) reaction. The sources typically emit neutrons with an energy of around 4-5 MeV. Here are some characteristics of AmBe neutron sources listed in table 2.4:

S.No	Parameter	Description
1	Neutron energy	4-5 MeV
2	Neutron yield	$\approx 10^7$ neutrons/s
3	Half-life	432 years
4	Shielding requirements	Heavy shielding required (e.g. steel, lead) to protect against gamma rays and neutron radiation
5	Typical applications	Neutron radiography, oil well logging, industrial process control, scientific research

Table 2.4: characteristics of AmBe neutron sources

Other common radioactive isotope neutron sources are listed in table 2.5 with there characteristics and applications;

S.No	Isotope	Half-life	Decay Mode	Application
1	Cobalt-60	5.27 years	β and γ	Radiation therapy for cancer treatment
2	Americium-241	432 years	α	Smoke detectors
3	Iodine-131	8.02 days	β and γ	Medical diagnosis and treatment of thyroid cancer
4	Cesium-137	30.17 years	β and γ	Industrial gauges and testing equipment
5	Carbon-14	5,700 years	β	Radiocarbon dating of organic materials

Table 2.5: Characteristics of radioactive isotope neutron sources

Overall, radioactive isotope sources can provide a relatively compact and portable source of neutrons, and can be well-suited for variety of applications, including industrial radiography, medical isotope production, and neutron activation analysis. However, they typically have lower neutron intensities than fission or spallation sources, and they require special handling procedures and safety protocols due to their radioactivity.

2.5.2 Inertial Confinement Fusion Neutron Sources

Inertial confinement fusion (ICF) is a process in which a small pellet of hydrogen fuel is compressed and heated by high-powered lasers or other sources, causing the hydrogen nuclei to fuse and release a large amount of energy, as well as neutrons. ICF neutron sources offer several advantages, including high neutron yields, short pulse durations, and relatively small size. They are currently being developed for a range of applications, including nuclear energy production and stockpile stewardship [90].

2.5.3 Electron Linear Accelerator Neutron Sources

Electron linear accelerators (linacs) can be used to produce neutrons through a process known as photonuclear reaction. In this process, high-energy photons are directed onto a heavy metal target, such as tungsten or lead, which then emits neutrons as a result of nuclear reactions. Linac-based neutron sources can offer high neutron intensities, relatively short pulse durations, and the ability to tune the neutron energy spectrum. They are currently being developed for a range of applications, including nuclear medicine and industrial radiography [91].

2.5.4 Spontaneous Fission Neutron Sources

Some isotopes, such as californium-252, and plutonium-240 can also emit neutrons as a result of spontaneous fission. These sources can offer high neutron intensities and relatively fast pulse durations, but they may also have high costs and safety concerns due to their radioactivity. These sources are employed in applications such as well logging and neutron radiography.

2.5.5 Laser-driven Neutron Sources

Laser-driven neutron sources are also being developed. Laser-driven accelerators can produce neutrons through a process called laser-driven nuclear fusion. High-intensity laser pulses are directed onto a target containing hydrogen or deuterium, causing nuclear fusion and the release of neutrons. These sources have advantages such as high neutron yields, short pulse durations, and potential for compact size. They are being developed for applications like cancer therapy and materials science.

2.6 Summary

In conclusion of the chapter, A short summary of the main characteristics of the above mentioned neutron sources is presented in table 2.6.

S.No	Name	Reaction	Neutron flux	Operational Mode (MeV)	$E_{neutron}$
1	Natural sources and Spontaneous fission	(α,n), (γ,n)	2.03×10^6 n/s/μg, 10^7 n/s, 10^{2-5} n/s/Bq	Continuous	0-5.5 MeV, 20 keV-1 MeV
2	Fission reactors	(n,f)	10^{13-15} n/cm^2/s	Continuous	up to 100MeV
3	Spallation sources	(p,n)	10^{15-16} n/cm^2/s	Continuous	up to 1GeV
4	Electron linear accelerator neutron sources	Photonuclear	10^{10}-10^{14}	Pulsed	0.1-30 MeV
5	Laser-driven neutron production systems	(p,n), (d,n), (γ,n), (d,d), (d,t)	10^{13-15} n/cm^2/s, 10^{13} n/s/mA, 10^{8-10} n/s	Pulsed	Wide spectrum up to tens of MeV, 2.45 MeV, 14.1 MeV

Table 2.6: Summary of neutron sources

.

Overall, there are many different mechanisms by which neutrons can be produced, each with its own advantages and limitations. Understanding the strengths and weaknesses of each source can help us to choose the most appropriate source for their specific application. The development of new and innovative neutron sources, such as laser-driven neutron production systems, is an active area of research and is expected to continue to expand the range of neutron applications in the coming years.

Chapter 3

Laser-Driven Neutron Generation: An Overview of Different Acceleration Schemes and Target Materials

This chapter is devoted to the description of the characteristics and working principles of laser-driven neutron acceleration systems. In such systems a super-intense laser pulse is delivered on a target, from which ions are accelerated and induces nuclear reactions, which leads to the neutron production. The physics of laser-target interaction will be discussed in section 3.2. Further discussion will be based on the laser-driven neutron acceleration schemes and ion-neutron conversion mechanisms with focus on both theoretical and experimental aspects of neutron production. Finally, information about the current state of the art in the field of laser-driven neutron acceleration along with other schemes are also given.

3.1 Introduction

The number of neutron sources around the world are steadily increasing, the new fission reactors and spallation facilities are insufficient. For this reason, we require most cost-effective small and medium-scale accelerator-driven neutron generators for neutron flux applications. The neutron energy spectrum, neutron flux, and source sizes are used to classify neutron sources. In fact, there are only two kinds of high flux neutron sources accessible for practical usage. The first one is nuclear fission sources that comes from nuclear reactors and from the use of fission chain processes. Spallation neutron sources, are considered as second generation neutron sources [7, 8].

Fig. 3.1 summarizes the neutron generating schemes and problems for laser-based neutron sources. It is divided into three steps. In first step we deals with particle beam optimization, increasing laser repetition rate, and decreasing laser size. Second step is based on the generation of neutrons from laser based systems, it involves the use of high energy particle beams in various laser acceleration mechanisms. The third step is based on the characterization of neutron sources and to design it for suitable application schemes.

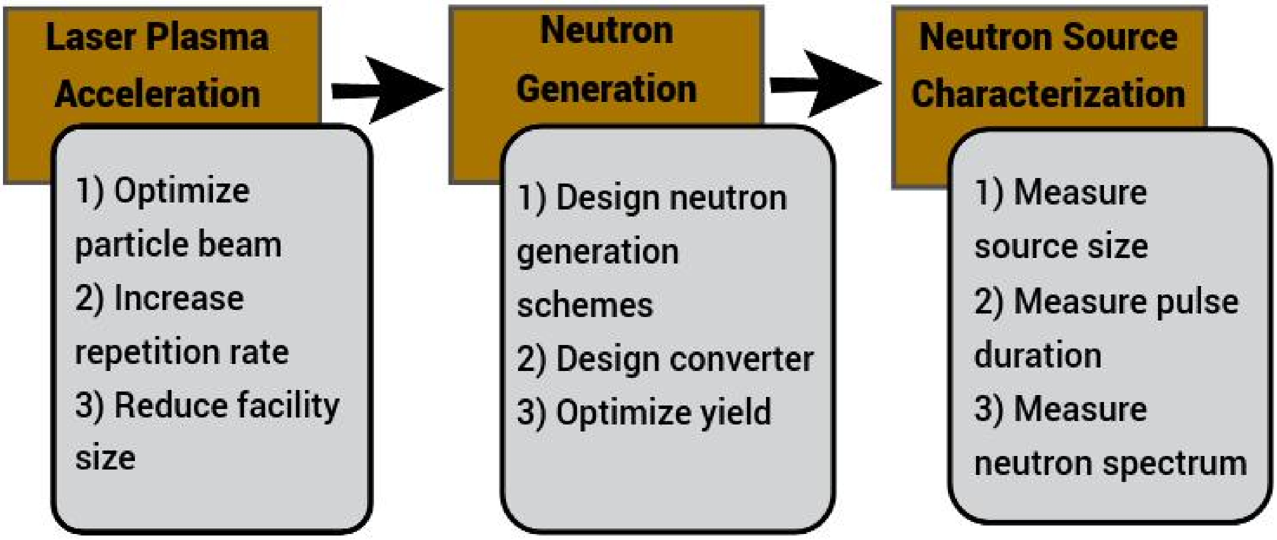

Figure 3.1: General scheme for laser-based neutron source

.

The first stage deals with particle beam optimization, increasing laser repetition rate, and decreasing laser size. Current experiments are highly unstable, and creates difficulties to optimize the particle beam. To address these challenges, controlling the experiment settings, particularly the laser and target parameters, has to be improved. Distortion effects are a main challenge to the precise focusing of high-intensity laser pulses. Stable laser energy output, improved laser focusing and shot placement is required to lessen the fluctuations in neutron emission between laser shots. The second stage accounts for neutrons production by three different schemes from laser-driven particle beams, it includes: the electron-driven, ion-driven and fusion-driven scheme. All these methods can produce high flux pulsed neutron sources each with different characteristics. The challenges at this stage includes the choice of suitable neutron generation schemes and designing neutron converters for optimal neutron yield, spectrum and beam directionality. The third stage deals with the challenges in characterizing and using neutrons due to their unique features. This problem is unlikely to be resolved by simply improving the neutron yield since it is constrained by the nature of laser-based neutron sources, and has an upper limit due to the total laser energy output. It will be necessary to develop new ways for exploiting laser neutron sources in the future. Significant efforts is required to address this problem [1,8].

To better understand the laser driven neutron acceleration schemes, first we will introduce the fundamental theoretical concepts and the required neutron interaction mechanisms with matter.

3.2 Physics of Laser-Plasma Interaction

Since 1980s, Laser technology has been advanced significantly with the invention of chirped pulse amplification (CPA) laser system [11]. For almost three decades, the laser focused intensities have been steadily increasing. In order to directly accelerate ions in a laser field, which requires intensities in range of 10^{24} W/cm^2, the existing laser system's intensities are of 5.5×10^{22} W/cm^2, are still insufficient [9,11]. Any material that is subjected to electromagnetic (EM) fields of this intensity will instantly ionize and become plasma, which may then accelerate ions by creating quasi-static electric fields. Laser-plasma accelerators for ions, electrons, and photons are based on the nonlinear behavior of such relativistic plasma in a very strong electromagnetic field. Therefore, a thorough explanation of dynamics laser-plasma is required to introduce the the fundamental features and laser plasma interaction parameters to provide some generic descriptions for the fundamental acceleration models relevant to our study.

3.2.1 Plasma

Plasma is a fourth state of matter and can be found rarely on surface of earth. More than 99.9% of visible matter in the universe is in this state [9]. This macroscopic fourth state is made up of partially or completely ionized matter with an equal amount of positive and negative charges. This ionization enables the material to exhibit collective behavior as the electromagnetic forces allows charged particles within the plasma to interact over larger distances [9, 10]. The plasma frequency, Debye Length, and critical density are the significant parameters of plasma which are vital to understand the laser plasma interaction, which is essentially a collection of ions and electrons. Therefore first we will provide short introduction into plasma physics.

Plasma Frequency

Plasma frequency ω_p is an essential parameter for an accurate description of plasma as it describes the motion of electrons [10]. There is a plasma frequency for each kind of charge particle within plasma. The electron frequency, on the other hand, is the highest and most significant, and is often referred to as plasma frequency. If a plasma in equilibrium state is subjected to an external force, local neutrality may be displaced on a microscopic scale. This will change the electron density and generates an electric field, which acts as a restoring force on imbalanced electrons. This force will disrupt electrons from their equilibrium position and creates an harmonic oscillation around their equilibrium point [9]. The frequency at which an electron oscillates around its stable position is known as plasma frequency. It can be determined using the Maxwell equation, with the elementary charge e, electron density and the permittivity of free space ϵ_0 and electron mass m_e [12]. A plasma frequency is defined to be proportional to the square root of the electron density n_e inside the plasma. When the plasma frequency surpasses the laser frequency, the laser field cannot penetrate the plasma owing to the quick response of electrons.

$$\omega_p = \sqrt{\frac{e^2 n_e}{\epsilon_0 m_e}} \tag{3.1}$$

Debye Length

Plasma do not have significant strong electric fields due to Debye shielding. Due to strong plasma conductivity, Debye shielding occurs when an external electric field is shielded from the inside of a plasma. Plasma electrons may freely travel in reaction to electric fields, resulting in polarization, which prevents the external electric field from entering the plasma. This shielding length scale is known as Debye length [11]. The electric potential of free charge carriers is inversely proportional to the distance r between neighboring particles, allowing interactions across long distances. In a plasma this long distance interaction is screened by the superposition of the potentials of neighboring ions and electrons. According to Elizer, it transforms the Coulomb potential into the Debye potential [13]. Debye length λ_D is defined as:

$$\lambda_D = \sqrt{\frac{\epsilon_0 K_B T_e}{e^2 n_e}} \tag{3.2}$$

Here, T_e is electron temperature of charge state Z, and K_B is the Boltzmann constant.

Critical Density

The density at which the plasma frequency ω_p becomes equal to the frequency of an electromagnetic electron wave in plasma is defined as critical plasma density. The dispersion relation of these waves is given by:

$$\omega = \omega_p^2 + \frac{3}{2}k^2 v_e^2 \tag{3.3}$$

ω is the frequency of an electron plasma wave, k being the wave number, and v_e represents the mean velocity od an electron in plasma. If perturbation is induced by electromagnetic waves entering plasma, the Maxwell equations can be used to obtain the corresponding dispersion relation [9, 13]:

$$\omega_L^2 = \omega_p^2 + k^2 c^2 \tag{3.4}$$

When $\omega_p > \omega_L$, k becomes imaginary and propagation inside the plasma reduces to an evanescent wave. For laser light with a particular wavelength λ_L, one may determine the critical density n_c using the formula; [10, 13]:

$$n_c = \frac{\epsilon_0 m_e \omega_p^2}{e^2} \tag{3.5}$$

Plasmas with $n_e < n_c$ are known to be an underdense, it allows laser propagation inside the plasma. When $n_e > n_c$ the plasma is said to be overdense and becomes opaque for a laser radiation [9]. The critical density for a widely used system, such as PHELIX laser, is about 1×10^{21} cm^{-3} [9], and solid state density of regular targets is about 3×10^{21}cm^{-3} [9]. It implies that these targets becomes opaque when they enter into plasma state [9].

3.2.2 Interactions of Laser with Electron

According to Einstein´s theory light only exists as discrete bundles of energy called photons. Its energy is defined by E = $\frac{hc}{\lambda}$ where h being the Plank constant where the λ represents photon wavelength. This energy ranges between 1 and 3 eV for a visible and infrared lasers. Single photon ionization is not achievable for most of the materials due to the photo-effect ionization threshold which ranges between 5 to 20 eV [11]. Increase in light intensity increases the likelihood that two or more photons may be absorbed simultaneously which can result in a phenomenon known as multi-photon ionization. With progressively increasing photon counts, this can start at an intensities of about 10^{10} W/cm^2 and ranges to 10^{12} W/cm^2, benefiting from an increase in absorption cross section [9, 11, 13]. These intensities are already possible with current short pulse lasers using amplified spontaneous emission (ASE), which builds a pedestal of several ps or ns before the primary pulse. These values can be attained by pre-pulses brought on by amplified reflections within a laser system that occur before the primary pulse. Both effects have the ability to ionize the target and send shock waves through the material, both of which can weaken or damage the target's structural integrity [9, 11, 13].

The laser electric field becomes powerful enough to ionize the target field at higher intensities. A potential suppression is consequently brought on by superposition of atom's boundary electric potential and the potential generated by the laser. As a result, the potential barrier for electrons in a nucleus' field is lowered. If the barrier is suppressed below the ground state, the atom is directly ionized, or the electrons can exit the atom via the tunnel effect. The first effect, known as tunnel ionization, is exhibited at intensities below 10^{13} W/cm^2, whereas the latter, known as barrier suppression ionization, is observed at levels over 10^{13} W/cm^2 [11]. A free electron can be accelerated directly in the laser field at an intensities of 10^9 W/cm^2 if it is already present in the target, whether it was produced by early pre pulses or by background radiation. The accelerated electron can then ionize nearby atoms to start a chain reaction [9,11,13].

Strong EM fields may be used to explore the interaction of powerful lasers with materials. This is useful when laser EM field dominates other potentials. This approximation is precise enough for most laser-plasma interactions to understand plasma dynamics. The electric field for a single mode laser pulse oscillating along x-axis and propagating along z-axis can be represented mathematically, [11].

$$E_{\vec{r},t} = E_0 s_{\vec{r},t} Cos(\omega t - kz) \tag{3.6}$$

whereby $\vec{r}$ is the position vector,E_0 is the strength of an electric field, and $s_{r,t}$ is the function that specifies the laser pulse's temporal envelope and spatial focusing. Using Maxwell equations, the relevant magnetic field representation is simply obtained. The Lorentz force describes the equation of motion for an electron with mass m_e and charge e under the influence of an EM field in the non-relativistic limit.

$$F = -e[\vec{E} + (\vec{v} \times \vec{B})] \tag{3.7}$$

An electric field $\vec{E}$, is the primary contributor for low and intermediate intensities. If the intensity is raised further to reach relativistic speeds. The magnetic field's influence cannot be neglected at this moment. This is true for electric field intensities exceeding 1.37×10^{18} W/cm^2 or amplitudes of $\mathrm{E}_0 > 3.2 \times 10^{12}$ V/m. For typical Ti:Sapphire laser, the threshold laser intensity is about 2×10^{18} W/cm^2 [11]. The amplitude of the dimensionless electric field is used to identify the kind of laser-matter interaction [11,13]:

$$a_o = \frac{e_0 E_0}{m_e \omega_L c} \tag{3.8}$$

When a_o is greater than one, interactions becomes relativistic. Within this particular domain of relativistic electron motion, inverse bremsstrahlung and resonance absorption are two factors that contribute to the heating of an electron. Heating of the vacuum occurs at higher intensities whenever a laser is used to produce an electrostatic wave at the critical density [9,11,13].

3.2.3 Ponderomotive Force

The charged particle is subjected to an electric forces when a laser beam travels through underdense plasma, which causes them to move at quiver speed.. Ion mobility can be neglected due to their heavy mass, ions response time is longer than laser-plasma interaction. The electrons in laser field oscillates at a frequency similar to laser optical frequency because the electric field inside a laser pulse is oscillatory. The ponderomotive potential is defined as the average kinetic energy of an oscillating electron, and it is mathematically stated as:

$$U_p = \frac{e^2 E_0^2}{4 m_e \omega^2} = 9.33 \times 10^{-14} I[W/cm^2]\lambda[\mu m]^2 \tag{3.9}$$

In addition, The presence of a gradient in the amplitudes of the electric fields is implied by the intensity variation during the laser pulse. Electrons are propelled toward a negative gradient in intensity by this inhomogeneity in amplitudes, which is identical to the force applied to particles from a conservative potential field. This force is known as ponderomotive force. Mathematical expression of ponderomotive force is represented by spatial derivative of ponderomotive potential and can be obtained by deriving the electron fluid momentum equations in cold plasma approximation, given below:

$$F_p = -\frac{e^2 E_0^2}{4 m_e \omega^2} \Delta(s_{r,t}^2) \tag{3.10}$$

$$F_p = -\frac{e^2 E_0^2}{4 m_e \omega^2} \Delta(s_{r,t}^2) \tag{3.11}$$

Here F_p represents ponderomotive force, e being the charge of the particle, m_e is the mass of an electron, ω shows optical frequency of the field, and E shows the amplitude of an electric field. The physics model underlying the ponderomotive force, electrons that have been accelerated in a higher electric field intensity region will overshot in a lower electric field intensity region because the lesser electric field there cannot completely stop the motion. The collective effect is that, the electron will move along the gradient of intensity. In relativistic case, the ponderomotive potential and the relative ponderomotive force will become:

$$U_p = \gamma m_e c^2 = m_e c^2 (\sqrt{(1 + \frac{a_0^2}{2}}) \tag{3.12}$$

$$F_p = -m_e c^2 \Delta(\sqrt{(1 + \frac{a_0^2}{2}}) \tag{3.13}$$

Here, γ being the relativistic factor, and a_0 is the normalized vector potential [11].

3.3 Laser-driven Neutron Acceleration Schemes

The development of high-intensity laser-based particle sources has paved the way to study laser plasma neutron sources. This notion was introduced more than 20 years ago, but proof-of-concept research is still ongoing. Laser driven neutron sources are of particular interest due to the higher acceleration gradient of laser plasma interactions than that of conventional accelerators [11]. Conventional accelerators can only accelerates at a gradients of 100 MV/m because the material in chamber breaks down under high electric field. Strong acceleration gradient indicates that laser plasma accelerators need a thousandth of the acceleration length to accelerate particles to the same energy level, potentially making these sources to be portable [11,14]. In addition, laser driven neutron sources can be versatile, implies that we can obtain high energy ion, electron, x-rays, and neutron beams. All of them have significant important applications in research and industry.

Accelerator-driven low-energy neutron sources are accelerator facilities for neutron production generating particles with energy less than 100 MeV operating at a power level below 100 kW. The limits set on the power level of the machine and on the maximum energy of the accelerated particles remark the distinction between these devices and high-power systems such as spallation sources and nuclear reactors. These accelerators can produce ultra high intensity of lasers of 10^{18} W/cm^2, their electric fields and magnetic fields are high enough that that charged particles achieves an energy regime where the production of neutrons occurs through various different nuclear reactions. When lasers achieves intensities in this range, it enables us to differentiate them in between two types of laser system. One is know as table-top lasers, these are femtosecond laser and are based on short pulses in energy range of few joule J. These systems have smaller size which can be installed in a room and are low cost, suitable for small research centers and universities. The second system is based on large laser infrastructures that can deliver energies in hundreds of J per shot in ps or ns. These facilities includes laser confined fusion based experiments.

Laboratory scale neutron sources provides high flux of neutrons but they are large, expensive, and sometimes even prohibited. Ions acceleration by laser has become the most promising laser acceleration mechanism that are currently accessible for neutrons generation [9]. Therefore, for generating neutrons, the laser driven neutron processes induced by three different acceleration schemes: It includes laser driven ion beam, thermonuclear fusion by trigger fusion reactions and photo-induced nuclear reactions [14]. Neutrons can also be produced using an ultra-intense laser systems that are either based on the acceleration of low Z atomic nuclei i.e., hydrogen isotopes or by the generation of γ-rays to induce nuclear reactions [14]. The laser ion driven neutron sources includes the nuclear reactions i.e., (p,n), d(d,n)^{3}He, d(t,n)^{4}He, Li(p,n), Li(d,xn), (γ,n) and (γ, fission) [14, 15]. Other neutron generation schemes are t(d,n) fusion reaction or more exotic reactions like Li(p,n) [16]. The reaction cross-section and center-of-mass energy for the neutrons produced from these reactions are more favorable than fusion reaction d(d,n)^{3}He [14,15]. Each of these techniques can also produce high flux of neutrons each with different characteristics. For instance, isotropic monoenergetic neutrons can be produced in short bursts using laser-driven fusion neutron sources. Electron driven neutron sources can produce short pulse broad spectrum neutrons at high repetition rates. Ion-driven neutron sources have substantially greater conversion ratio and the directionality of neutron beams depends upon the incident ion energy, converter material, and the converter profile [11]. Current challenges includes; selection of optimal neutron production systems and developing neutron converters to maximize neutron yield, spectrum, and beam directionality.

Furthermore, to better characterize the laser-driven neutron sources, advancement is required in detector technology. Currently, no devices can precisely measure the neutron pulse duration and temporal characteristics. Direct measurement is challenging because of the short pulse of order of sub-ns, which is thousand times shorter than the shortest spallation neutron source. On the other hand, fast neutrons cannot produce measurable phenomenon in a short period of time because they carry no charges and barely interacts with other particles. Therefore all current experiments, lacks the precise information on the size of the source and the duration of the neutron pulse [11, 13]. Experimental methods can only measure neutron fluence in neutrons/sr. However, the intensity of neutron sources is an important parameter to describe in terms of neutrons/sec/cm^2/sr rather than fluence [11]. The neutron pulse duration was estimated from flight time of ion beam passing through the interaction region, ut this approach has not been verified experimentally. To accurately calculate neutron flux, accurate measurements of neutron pulse length and surface emission size are necessary. These data can also guide the research on laser neutron sources in order to achieve higher flux.

Laser-induced procedures for generating neutrons are comparable for both kinds of ultra-intense lasers, three aspects must be considered:

- Total amount of neutrons produced in laser-ion acceleration, follows a laser energy squared relationship, it means that large systems often generate three to four orders of magnitude more neutrons than table-top systems (10^9-10^{10} n/shot).

- Due to the illumination setup and total laser energy needed, neutron production by implosion of fusile capsules can only be generated in big facilities with tens or hundreds of laser beams.

In large facilities, the laser repetition rate is restricted to a few shots per hour, however in small systems, the shot rate is generally 1-10 Hz. Keeping these distinctions in mind, in next section we will discusses experiments using one of the two laser types.

3.4 Neutron Production by Laser Ion Beam

Laser-plasma ion acceleration is a technique in which ions are accelerated from a thin solid target as a consequence of irradiation with a super-intense laser pulse. The main feature of super-intense and ultra-short laser pulses is that, when impinging onto a target, they rapidly ionize matter, turning it into a plasma. The creation of a plasma is necessary for ion acceleration: indeed, plasmas are able to sustain electric fields of the order of some TW/m, which enable the acceleration of charged particles over length scales of the order of a few µm.

The principle on which plasma-driven ion acceleration relies was first formulated by Veksler in 1957 [51] and is called coherent acceleration. According to this mechanism, the magnitude of the accelerating field is proportional to the number of particles being accelerated. Although Veksler's idea dates back to 1957, up to 1980's the development of ultra-high-intensity laser systems was hindered by the impossibility of sufficiently amplifying the ps- and ns-long laser pulses due to unwanted non-linearities and optics damage.

In laser-driven ion acceleration experiments the target is commonly a thin foil, which, when irradiated, turns into a plasma with density values typical of a solid. Ionizing a thin solid target requires laser intensities greater than 10^8 W/cm^2. If the intensity is further increased, relativistic effects become non-negligible, above all on the electrons dynamics. An immediate way to understand whether relativistic effects on the electrons motion are negligible or not is to evaluate the magnitude of the normalized vector potential a_0, which is defined as:

$$a_0 = \frac{e|A_0|}{m_e c^2} \lambda[\mu m] \sqrt{\frac{e^2 \lambda^2 I_0}{2\pi m_e c^2}} = 0.85\lambda[\mu m]\sqrt{I_0[10^{18} W/cm^2]} \tag{3.14}$$

where A_0 is the amplitude of the vector potential of the electric field, while I_0 is the peak intensity of the laser pulse. Relativistic effects cannot be neglected if $\mathrm{a}_0 = 1$, i.e. when intensities larger than 10^{18} W/cm^2 are delivered on the target. Therefore, when current super-intense lasers interact with matter, a plasma characterized by a relativistic electron dynamics is produced. If intensities of the order or 10^{24} W/cm^2 were reached, the ion dynamics would become relativistic as well; however, such intensities are still inaccessible with the currently available technology.

Since several years, various laser technologies methods have been demonstrated to accelerate the ions from laser plasma interactions. The radiation pressure acceleration (RPA), the laser breakout afterburner, and the target normal sheath acceleration (TNSA) mechanism are few of them [11, 14]. The most popular of them is laser accelerated ion beams usually deuterons or protons with TNSA mechanism. In TNSA process, a high-intensity laser pulse is focused on solid target i.e., thin metal foil. The ponderomotive force of strong electromagnetic field accelerate electrons to the relativistic energies at the focusing spot and creates hot plasma. Due to their low mass, electrons expand far faster than ions and absorb the most of the energy from laser. When these powerful electrons leaves the target via the rear surface, it creates a strong sheath of electrostatic field (TV/m) on both front and back surfaces of metal foil, which escapes and accelerates ions from the target. This electrostatic field is dependent on the duration of the laser pulse and the mobility of the electrons. It is directly proportional to the duration of ion bunch which results in the short ion pulse of few pico seconds [14, 15]. This process has been found efficient in generating neutrons [11].

To produce and accelerate high energy ion beams, many of which are related to fusion reactions and neutron production such as from solid CD_2 target, deuterated plastic targets, and heavy water (D_2O) sprayed targets are the most typical cases. In most of these cases, the experimental setup for the production of neutrons is known as the pitcher-catcher configuration, shown in Fig. 3.2. They are made of materials with high neutron generating cross-sections to knockout neutrons by nuclear reaction. An ultra intense laser pulse is used to irradiate an object with H or D content. H or D ions are accelerated from the back side by TNSA and collide with a second target, where the nuclear reaction and neutron production take place. Neutrons can also be produced from an ion beam acceleartion in TNSA mechanism from gaseous or cluster targets with D content in which coulomb explosion plays an important role towards acceleration of ions which triggers the neutron production by interaction with other D ions and neutral atoms from neighboring clusters. Experimentally design for generation of neutrons by laser irradiation of clusters is shown in Fig. 3.3 [14, 15].

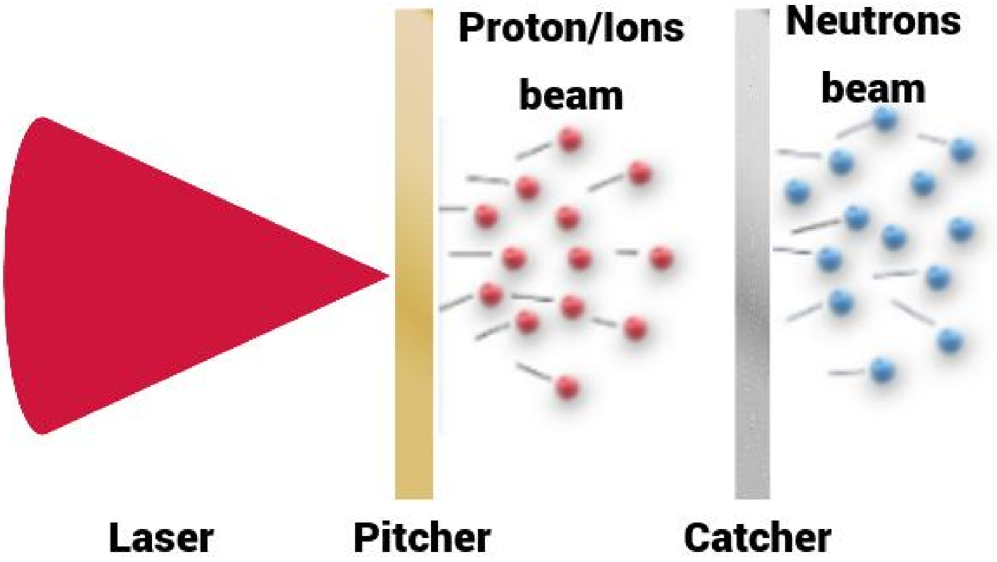

Figure 3.2: Sketch of laser-driven (ion,n) nuclear reaction using TNSA mechanism in a pitcher–catcher configuration producing neutrons [21]

.

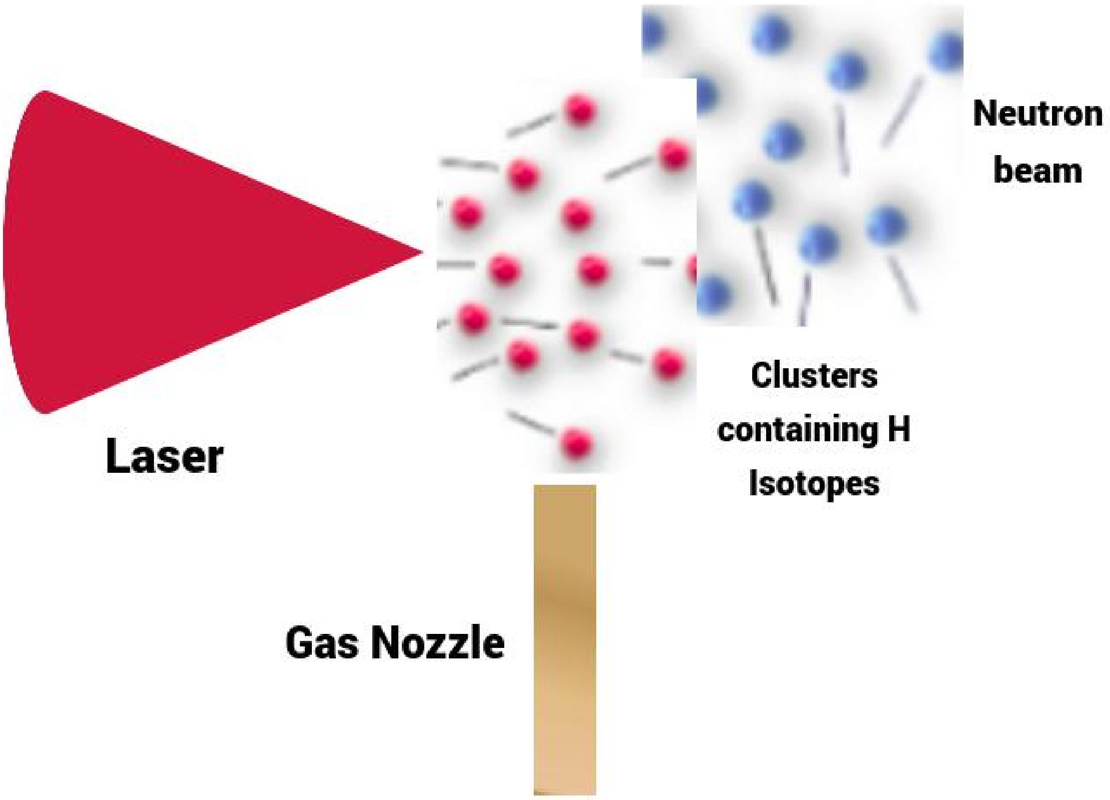

Figure 3.3: Sketch of laser-driven (ion,n) nuclear reaction using TNSA mechanism by irradiation of gas phase targets (clusters) based on Coulomb explosion for producing neutrons [21]

.

Laser-driven nuclear fusion produce a high neutron flux with a small, controllable source [17]. The introduction of high-intensity lasers, as well as a novel technique known as Chirped Pulse Amplification [18], has made it possible to produce neutrons in a considerably more compact setup. In high-energy physics, this innovative approach has the ability to meet the demand for small and energetic neutron sources [14, 15]. Efforts to develop and improve ultra high-intensity laser neutron sources have received a lot of attention and several approaches have been tested on laser systems with scales ranging from milli-Joules [19] to kilo-Joules [15]. Among them, the most promising method is the laser ion-driven neutron source scheme because of its high efficiency and high neutron yield. Many experiments have shown a maximum yield of neutrons around 10^{10} n/sr/shot [8] in a so-called “pitcher-catcher” arrangement. These ions then collide with a low-Z metal “catcher” target on a centimeter scale, performing nuclear processes and creating neutrons. In comparison to 4×10^8 n/J in TNSA acceleration for laser-driven neutron generation and 4×10^6 for laser-electron driven neutron source, this approach can achieve laser-to-neutron energy conversion efficiency of roughly 6×10^8 n/J [14, 20]. Light ions (protons and deuterium) accelerated by the TNSA mechanism in either d-d or p-Li reactions can also be used to investigate the high neutron fluxes.

Neutrons produced by ion-fission and spallation processes using ions driven by a laser are less desirable due to the high energy ions needed for it (hundreds of MeV, far beyond the present energies of laser driven ions) and it also needs severe safety procedures and complexity of employing fissile materials.

3.4.1 Neutrons Production from Light Ion Nuclei - Proton or Deuteron Induced Reactions

In a laser-driven neutron source exploiting pitcher-catcher configuration for neutron production occurs in CANS (Compact Accelerator Neutron Sources). In these accelerators ion beam impinges on a target made of converter material in which neutron production reactions takes place. As explained in previous section, neutrons can be produced from a large number of ion-induced nuclear reactions that are categorized into different categories according to the particle inducing the process. Light ion-induced nuclear reactions for neutron generation is one of them.

In this scheme, neutrons are produced from lighter ion-induced nuclear reactions. Generally light converter material such as lithium or beryllium is bombarded by protons or deuterons with energy ranging from 2 to 50 MeV. The generated neutrons possess characteristics that strongly depends on the kinetic energy of accelerated ions and nature of the induced nuclear reaction. In principle, a high neutron flux can be obtained by accelerating all the ions up to an energy corresponding to a peak in the cross section of the neutron-generating reaction and bombarding the converter material at the highest possible frequency. However, in practice, the accelerator performance in terms of duty cycle and power is always limited by mechanical and heat disposal constraints on the converter [79].

When charged ions penetrates into matter many processes can occurs. it includes:

- Ions decelerate inside matter and deposits their kinetic energy in the form of heat. This can induce local melting of converter, for which a cooling system is required to be designed.
- The radiation damage that can produce defects in the crystalline structure induced by the impinging ions must be taken into account.

Therefore, converter design should be made in order to handle problems when in contact with air and water such as inflammability, toxicity, and stability. Since, the choice and design of a perfect converter material is a pre-requisite for obtaining large ion-to-neutron efficiency in the considered energy range ion. For example, in case of low-energy neutron sources lighter elements such as lithium or beryllium are employed.

3.4.2 Materials choice for (p,n) and (d,n) reactions

Analyzing the cross section of the possible reactions is the first step in figuring out the suitable process for generating neutrons. In fact, for choosing competitive neutron source, the selection should be based on the reactions resulting with high neutron yield. In general, higher neutron yield comes from nuclear reactions whose cross section peaks at low energies. This is because at a certain point in the process of slowing down, all the ions cross the energy value that corresponds to the peak of the cross section, increases reaction probability. Due to this reason, choices are made from the reactions induced by deuterons or protons on low Z materials like beryllium or lithium in the framework of laser-driven neutron sources. For these materials, the cross section of (p,n) and (d,n) reactions is shown in Fig. 3.4. Cross sections for (p,n) and (d,n) nuclear reactions on a set of medium Z materials are also shown in Fig. 3.4. Some of isotopes of these elements have cross sections for ion-induced neutron production that reach a peak at higher energies than low Z elements. Since these materials have a large cross section at peak energies, they could be used in experiments with very energetic ions or in unusual designs for converter design [79].

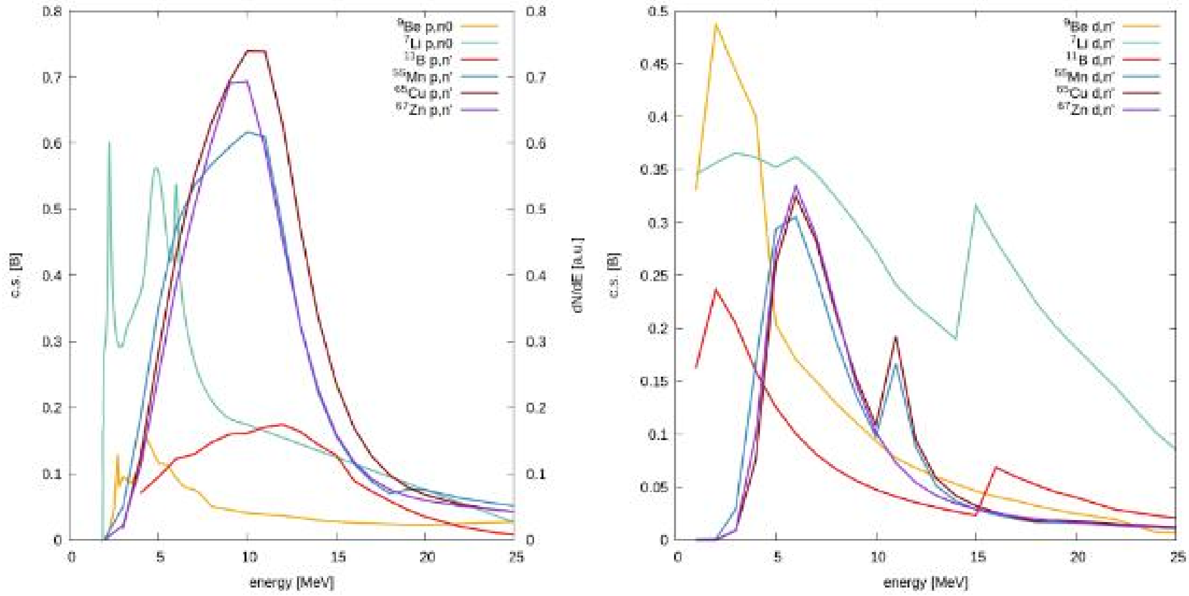

Figure 3.4: Cross section for (d,n) (on the right) and (p,n) (on the left) reactions on a set of converter materials [79]

.

The Q-value and threshold energy for (p,n) and (d,n) reactions on lithium and beryllium are listed in table 3.1. The Q-value is positive for (d,n) reactions while it is negative for (p,n) reactions. Therefore, deuterons produce the most energetic neutrons. In particular, the Q-value of (d,n) reactions on lithium and beryllium is equal to 15.03 MeV and 4.362, respectively. Furthermore, being exothermic, (d,n) reactions donot possess threshold energy this implies that, in principle, all ions produced by laser-plasma interaction are available for reaction. Wherever, it can be seen from Fig. 3.4 that no data for the cross sections are reported at energies below 1 MeV.

S.No	Element	Reaction	Q-value (MeV)	E_{th} (MeV)
1	Beryllium	(p,n) and (d,n)	-1.85 and +4.36	2.06 and 0
2	Lithium	(p,n) and (d,n)	-1.64 and 15.03	1.88 and 0

Table 3.1: Q-value and E_{th} for (p,n) and (d,n) reactions on beryllium and lithium

.

Aside from the amount of neutrons produced and the amount of energy required, the directionality of the neutron beam could also be a consideration for applications. The higher the fluences that can be reached, the more collimated the neutron beam is. In particular, the neutron beam divergence from a laser-driven pitcher-catcher source in the laboratory frame will be a mix of the divergence of the input ion beam and the neutron beam divergence expected for a collimated ion beam. Reactions with light ions, such as ^{7}Li(p,n)^{7}Be, ^{9}Be(p,n)^{9}B, ^{13}C(p,n)^{13}N, and d(d,n)^{3}He, produces narrow cone beam of neutrons, which makes it possible to get a high peaked flux of neutrons. Among the candidate reactions, those that happen in lithium give off the most collimated neutron flux from (p,n) reactions for proton kinetic energies just above the production threshold in the direction of the proton beam.

On the other hand, the neutrons generated by the (d,n) reaction on lithium is characterized by a degree of anisotropy increasing with the impinging ion energy. This behaviour is displayed in Fig.3.6 for deuterons impinging on lithium with different kinetic energies. At values of the order of a few tens of MeV this behaviour is mainly due to stripping reactions, which implies that capture of the deuteron's proton when the nucleons pass near the target nucleus along with the scattering of neutron occurs at small angles. This process is common for the typical shape of the energy spectrum of neutrons produced by (d,n) reactions on different class of materials. On the other hand, the (d,n) reaction on lithium produces neutrons with a degree of anisotropy that increases with the increase in energy of impinging ion. This behaviour is displayed in Fig. 3.4 for deutrons impinging on lithium with different kinetic energies. At energies of the order of a few tens of MeV, this behavior is mostly caused by stripping reactions. This means that the proton of the deuteron is taken by the target nuclei, when nucleons pass close to it, scattering of neutrons occurs at small angles. This is a common process for (d,n) reactions on different kinds of materials to produce neutrons with typical shape of energy spectrum.

It is crucial for the feasibility of a laser-driven neutron source to discuss problems related to the technology of a converter materials properties. Since, the most commonly used materials as converter for neutron productions are lithium and beryllium. The problems associated in utilization of these elements in laser-driven neutron mechanism as well as in CANS, are:

- Low melting temperature is the limiting factor for maximum energy to be delivered on the target and, in turn, for the maximum energy of.
- Mechanical stresses: It can be induced by temperature gradients throughout the materials used as converter or by the flow of a coolant needed for negating the material melting.
- Hydrogen embrittlement induced by blistering: the collection of a gaseous hydrogen at a depth corresponding to bragg peak of ions in converter material. The name of this phenomenon resemnles to the damage appearing on the target surface, known as blister. It leads to the destruction of target after a certain period of time.

When it comes to deal with prescriptions, idealy converter should be easily employable. This means that it should be strong enough to be moved around, less dangerous and less likely to react with oxygen and water, and it should not produce any long-lived radioactive nuclides. In table, we have given some examples of low Z converter materials that have already been used in accelerator-based neutron production, shown in table 3.2. In our work, we studied the role played by the proton and deuteron ion beam on lithium for neutron emission in the case of laser-driven neutron sources.

S.No	Reaction	$E_{projectile}$ (MeV)	E_{th} (MeV)	$E_{neutron}$ (MeV)	Neutron yield (n/mA/s)
1	^{7}Li(p,n)^{7}Be	2.50	1.88	0.60	9.09×10^{11}
2	^{9}Be(p,n)^{9}B	4.20	2.06	1.60 - 8.0	$0.50\text{-}1.20\times10^{12}$
3	^{9}Be(d,n)^{10}B	1.50	0	1.66	3.30×10^{11}
4	d(d,n)^{3}He	0.15	0	2.45	2.09×10^{9}
5	t(d,n)^{3}He	0.15	0	14.10	5.0×10^{10}

Table 3.2: Neutron-generating reactions in compact accelerator-based systems [79]

.

3.4.3 Target Normal Sheath Acceleration (TNSA)

The primary interaction of high intensity short laser pulse with a solid target depends upon the contrast of the laser pulse. It is defined by the ratio of unwanted, preceding laser light to the main pulse. At intensities greater than 10^{20} W/cm^2 with a contrast of 10^6 can excites a plasma that expands towards the input laser pulse. It is said to be a amplified spontaneous emission or unwanted laser pulses which is caused by a limited polarization separation in regenerative amplifiers. When this primary pulse interacts with the target, the ablative plasma creates an ideal environment for a wide range of uncontrollable phenomena. Due to relativistic effects and ponderomotive force, the laser beam undergoes self-focusing and significantly increases the intensity that can results in break up into many filaments, and can cause instabilities that could eventually leads to the creation of intense electrons and are usually called hot electrons. In addition, the target can be destroyed before the main pulse arrives due to the shock wave on the target, launched by the ablative pressure of blow-off plasma caused by the incident laser energy [21]. Their generation, as well as the understanding of the underlying mechanism, is of crucial importance for ion acceleration.

Ion acceleration by laser from solid objects is a complex multidimensional process. It encompasses relativistic and nonlinear effects, as well as collective and kinetic effects. Theoretical models for the different physical phenomena involved in TNSA ranging from basic analytical techniques over fluid models to fully relativistic, collisional three-dimensional computer simulations. Most methods to TNSA neglect the complex laser-matter interaction at the target's front side, as well as electron transport through the foil. These plasma expansion models begin with a hot-electron distribution that causes the increase of an initial ion distribution. The expansion of plasma into free space is often characterized as an isothermal rarefaction wave. The expansion models used to explain TNSA are quite identical. The description of plasma expansion dates back to 1954. Since then, many refinements of the models have been developed, with increased activity after the discovery of TNSA. This is similar to the general characteristics of TNSA. Furthermore, plasma expansion models are one-dimensional, but observations clearly reveal that TNSA is at least two-dimensional. Hence, these models can only reproduce one-dimensional properties, such as the particle spectrum of TNSA process [21].

Target normal sheath acceleration (TNSA) acceleration mechanism was first proposed by Wilks et al. in 2001 [58]. TNSA has been found a robust mechanism. It can produce a continuous, and exponential spectrum with a broadband energy and wide angular divergence [11, 21]. TNSA accelerates the lightest ions, such as protons, since they have the highest charge-to-mass ratio [22]. Due to the substantial presence of hydrogen as contamination on solid targets, the TNSA mechanism is not suited for accelerating other ion species unless specific target cleaning processes were performed prior to firing the laser pulse [9, 21]. The general scheme of target normal sheath acceleration is illustrated in Fig. 3.5.

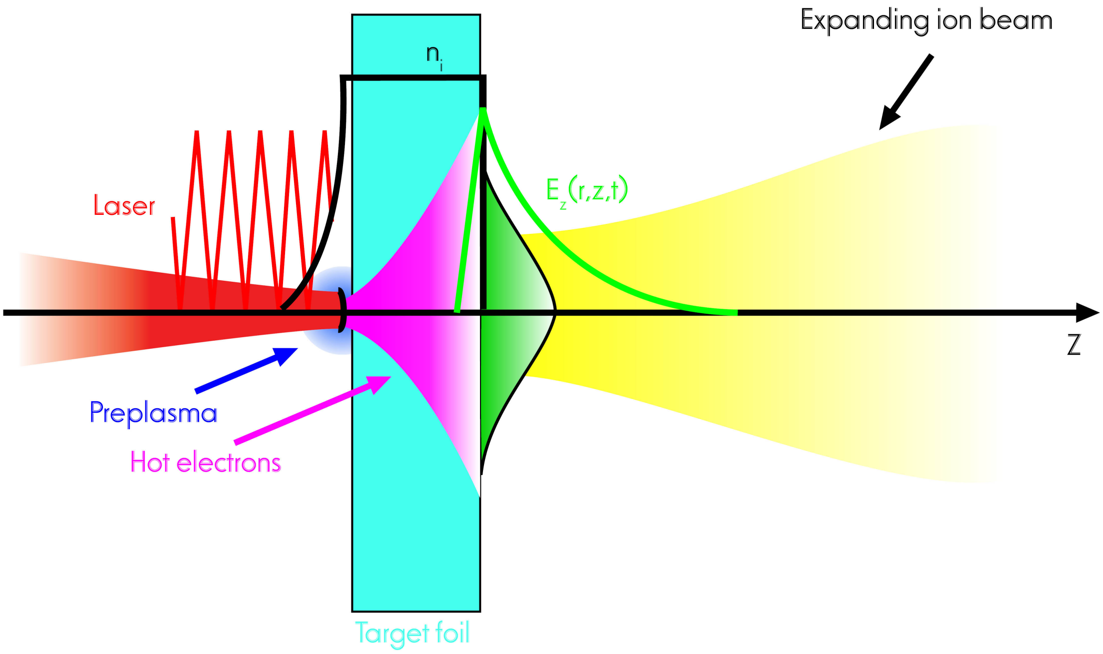

Figure 3.5: Illustration of target normal sheath acceleration (TNSA)

TNSA is driven by the electric field generated at the back side of target by very fast electrons that escapes from the target back surface and go into vacuum. Plasma is created by ionizing solid target and have a higher plasma density than critical density [21]. At the critical density surface, laser light will be reflected because it cannot pass through overdense plasma. When laser light is reflected, it forms an electric field perpendicular to the surface. This electric field, together with the p component of the input laser light, drives electrons away from the plasma surface. After the vacuum side of the laser field completes half of an oscillation cycle, the electrons are smashed back into the plasma, where the kinetic energy is thermalized by collision and the electrons at the front surface are heated. Brunel suggested this idea of electron heating up at the plasma border in 1987. When the laser intensity is high, the oscillation component of ponderomotive force contributes to the J × B heating, and play role in heating of the front surface electrons. [21]. Electrons absorbs energy on the same scale as the energy of oscillation in an external field. This causes high-energy, hot electrons to be created at the front of the target, which eventually reach the to rear side. The unbalance of charge generates a sheath field normal to the rear surface as these hot electrons cross the rear side boundary and escape to vacuum. Hot electrons form this sheath field, also prevents the electrons from escaping, and the induced electric field E becomes directly proportional to the electron temperature T_e, and the inversely proportional to the length scale of the sheath field, it can be expressed as:

$$E = \frac{T_e}{L} \tag{3.15}$$

Therefore, the energy of the ions driven inside this sheath field increases linearly with the electron temperature produced in typical experiments of the order of MeV, E is of the order of some MV/m, i.e. some TW/μm, while L can be estimated by using the electrons Debye length (a few μm) [21, 22]. This mechanism is suitable laser based neutron generation in terms of ion energies and conversion efficiency. With an increase in intensity, contrast, and target thickness, it is feasible to enter an acceleration phase that is more efficient for neutrons production.

Ions accelerated by TNSA are characterized by a typical decreasing exponential energy spectrum with a certain cutoff energy. In this regard, scalings can be very useful for predicting the performance of ion acceleration at laser intensities which exceed present-day capabilities. For example, in Fig: 3.6 the maximum proton energy against the laser irradiance I_r for some existing laser facilities is shown. As it can be seen, two different trend lines are present, which are attributed to different strategies for obtaining super-intense pulses. Indeed, lasers delivering highly powerful pulses shows a $\approx I_r - 1/2$ scaling, while less powerful ultra-short systems scale as I_r.

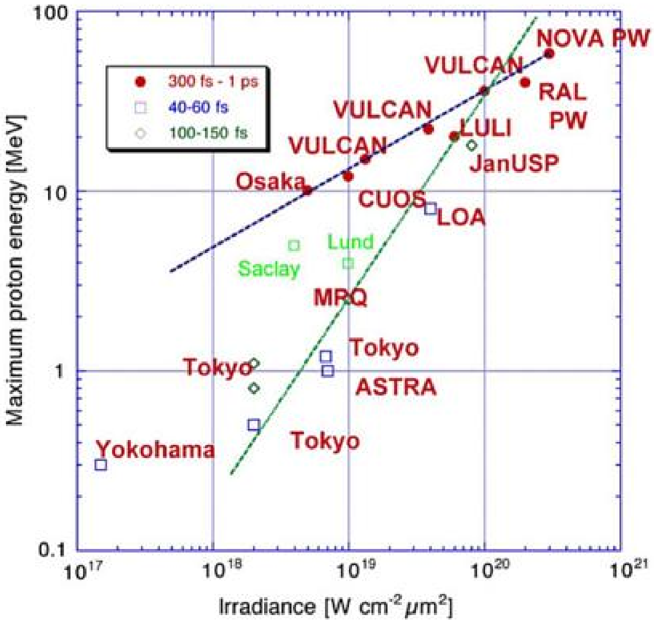

Figure 3.6: Maximum proton energy as a function of the irradiance for three possible ranges of laser pulse duration.

At present, it is not guaranteed that the ion energy scaling observed so far will be maintained with growing laser intensities. Furthermore, the availability of lasers of increasing power unveiled the existence of many different laser-ion generation mechanisms, such as radiation pressure acceleration (RPA), collisionless shock acceleration, break-out afterburner (BOA), Coulomb explosion, hole boring (HB) and relativistic transparency (RT). A TNSA component of acceleration is always present, even when trying to suppress it for studying alternative acceleration mechanisms.

3.4.4 Compact Accelerator Neutron Generator (CANS)

CANS exploits nuclear fusion reactions in so-called "Sealed Tube Neutron Generators (STNGs)". The main feature of such system includes ion source, accelerator, optics elements and target that are enclosed within a vacuum-tight enclosure, which constitutes a "neutron sealed tube". A scheme of the architecture of a STNG is shown in Fig. 3.7.

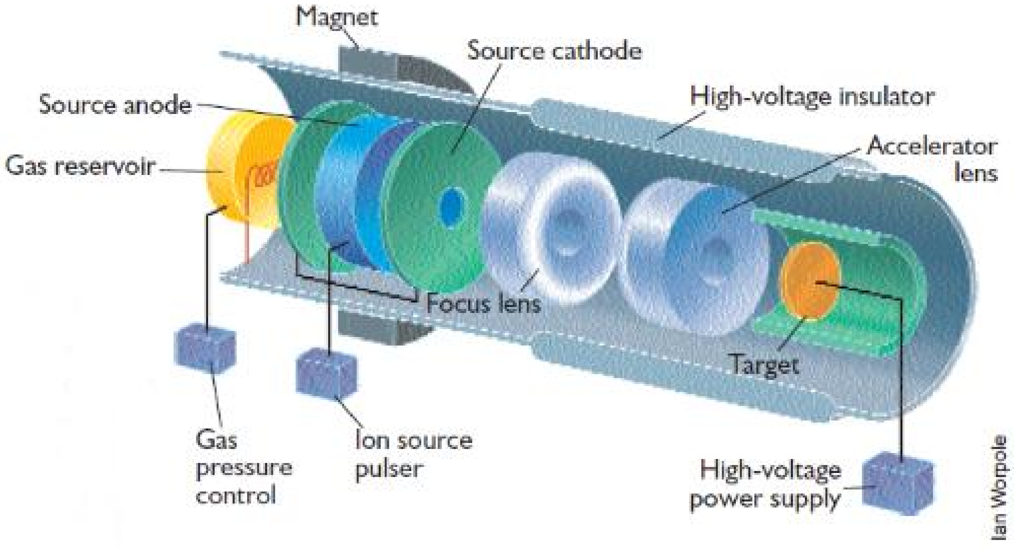

Figure 3.7: Illustration of structure of Sealed-Tube Neutron Generator(SGNT) [79]

STNGs accelerating system provides voltage up to kV. The ion source in these devices is Penning ion source, it consists of hollow cylindrical anode with a cathode plates at each end. When gaseous deuterium is passed through the anode region with a pressure of few mtorr, the electric field between anode and cathode ionizes the gas. The generated ions are successively guided to the acceleration section by a coaxial magnetic field (of several hundred Gauss) provided by a suitably shaped external magnet.

In this scheme, neutrons are generated by means of deuterium - deuterium (DD) or deuterium - tritium (DT) fusion reaction to create neutrons. The reaction of $D + D \rightarrow {}^{3}He + n$ yields neutrons with an energy of 2.45 MeV and $D + T \rightarrow {}^{4}He + n$ emits neutrons of energy of 14.1 MeV. Deuterons are accelerated up to kinteic energy of few hundreds of keV and made them to collide with a target nuclei rich in deuterium or tritium ions. Design of devices that uses nuclear fusion to produce neutrons are similar to that of other partcle accelerators. This apparatus consists of a source for the production of positively charged ions, one or more structures for acceleration, and a target for converting the ions into neutrons. All neutrons generated with this system are produced with energy approximately equals to 14 MeV.

This portable neutron generators can produce neutrons with a source strength of 10^{11} n/s [23]. The fusion reactions have the advantage since their cross sections are high at relatively low energy of about 50 to 100 keV, negating the need for large acceleration facilities. This enables them to be compact as compared to other sources, however their maximal flux and lifetime are limited [23]. These sources have the benefit over reactors or radioactive isotopes in that they may be switched on and off as needed. The neutron emission from these tube generators are mono-energetic and they can be used either in continuous operation or short pulse bursts with a duration of 5 µs [9].

For their low cost, STNGs are competitive in framework of small laser-driven neutron sources, makes them suitable to be used in both commercial and university laboratories. The model of TNSA fusion-based neutron system focused on an ion beam technology in a pitcher-catcher configuration is shown in Fig. 3.8.

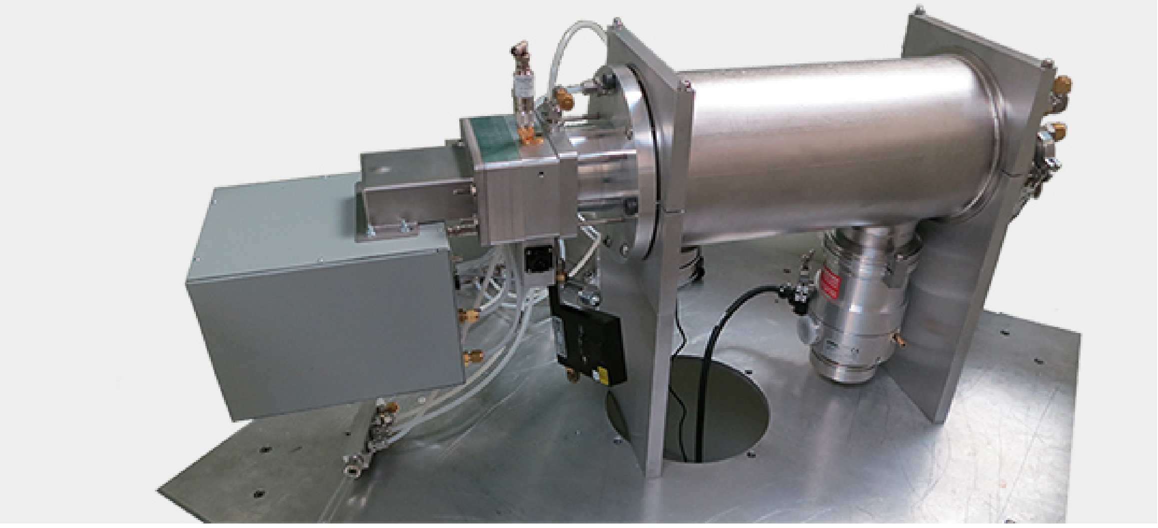

Figure 3.8: DD109 Neutron Generator

Advances in the technology of sealed-tube neutron generators are aimed at the development of systems that combine improved performance (e.g., greater neutron production, longer lifespan), better mobility (reduced dimensions and weight), and lower cost. Another critical challenge is the advancement of generator design and power supply in order to achieve reduced energy usage and hence longer off-grid operation.

3.4.5 A Look into Neutron Generation with Laser-driven Ion Beams: A Literature Review

Since 1998, the production of neutrons using super-intensive lasers has been a topic of investigation, starting with the groundbreaking work by Norreys and his team [80]. Their experiment used a laser pulse lasting 1.3 ps that was directed at a deuterated target, resulting in neutron production through the D(d,n)^{3}He nuclear reaction. Since then, progress in this area has been made on two fronts, due to factors such as the lower cost and reduced radiation protection compared to traditional neutron sources. Efforts have been made to improve the design of experiments and theoretical investigations through the use of various numerical simulations of laser-plasma interaction and Monte Carlo codes to study ion-neutron conversion. The literature contains both experimental and theoretical work on laser-driven neutron sources, providing an overview of the current state of the field.

The production of high-intensity laser pulses capable of delivering large amounts of energy to a target depends on pulses that provide a few joules of energy in a very short duration of a few hundred femtoseconds, focused on a small area. An example of the laser technology used to produce such short pulses is the Ti:Sapphire laser, which can have durations as short as tens of femtoseconds. However, building and operating large-scale super-intense laser facilities is very expensive and requires significant infrastructure, so there are only a few of them in existence, mainly devoted to the study of nuclear fusion. Super-intense lasers used in laser-driven neutron sources can be divided into two categories: TW-class and PW-class lasers.

TW-class lasers are compact and known as table-top lasers, with currently limited power to a few tens of terawatts. These systems are characterized by their small size (taking up the space of a room) and relatively low cost, making them suitable for use in research centers and universities, in addition to having limited radiation protection issues. Further reduction in size could lead to the development of portable neutron-generating devices using these lasers. On the other hand, PW-class laser systems are capable of producing 10^{10} neutrons per shot, while table-top lasers produce only a few orders of magnitude less. PW-class lasers have a low repetition rate of only a few shots per day, but it requires a large amount of power. In contrast, TW-class lasers can operate at high repetition rates up to the kHz, which is crucial for producing sufficient neutron flux for applications.

The vast majority of experiments on laser-driven neutron sources in literature have been conducted using PW-class lasers, due to the desire for high neutron fluxes for applications and the availability of large laser facilities equipped to handle the radiation protection issues related to neutron production. Most of the reported experiments on laser-driven neutron sources in the literature use PW-class lasers for the production of high neutron fluxes. However, some experiments using table-top lasers have also been conducted, mainly at the University of Michigan's "HERCULES" and "Lambda cube" laser facilities [81, 82]. The "HERCULES" laser can operate in both a table-top mode, delivering 1-1.5 J on target with a frequency of up to 0.1 Hz, and as a large laser facility with beams of 300 TW in power [16]. The "Lambda cube" laser, a table-top Ti:sapphire laser, was used in experiments aimed at creating a high-frequency pulsed neutron source of intensity 5×10^{18} W/cm^2. The laser was focused on a channel of flowing heavy water (D_2O), leading to neutron production via the d-d nuclear fusion reaction. With an intensity of 10^{19} W/cm^2 and laser pulses of about 40 fs, the laser was operated at a frequency of up to 2 kHz, delivering 6-18 mJ of energy on the D_2O-channel per shot. This resulted in the production of neutrons with a maximum energy of 2.45 MeV and a flux of about 10^5 n/s, comparable to other table-top laser-based neutron sources [83, 84].

In the previous section, we talked about laser-driven neutron sources with two different approaches used in ion-based acceleration, which are the "pitcher-catcher" and "bulk" schemes. In the majority of experiments in the field, the "pitcher-catcher" approach is utilized. This approach involves a specific structure for the acceleration of charged particles, as depicted in fig: 3.2. In this configuration:

- For proton or electron acceleration, common target materials include plastics such as mylar, polyethylene, and polystyrene, or metals such as aluminum, gold, and copper. However, the acceleration of protons requires a layer of hydrogen-rich contaminants on the rear of the target.
- If the aim is to accelerate energetic deuterons, deuterium-rich targets must be used. Deuterated polyethylene and polystyrene have been reported in literature. Alternatively, a layer of deuterated contaminants can be applied to the rear of a normal or deuterated plastic target. This can be achieved through various deuteration techniques such as using a deuterated paint or creating a layer of deuterated ice on the rear of the target [16].

In some cases, the bulk scheme has also been used in experiments [15, 17, 85]. For this approach, a target typically made of deuterated plastic is directly hit by the laser, and neutron production results from the d-d nuclear fusion reaction. The d-d fusion reaction produces neutrons with an energy of 2.45 MeV, which is much lower than the 14.1 MeV produced in d-t fusion reactions. However, tritium has not been utilized in laser-driven neutron sources due to its radioactivity.

The TNSA (Target Normal Sheath Acceleration) scheme is the most commonly used method for accelerating ions in laser-driven neutron sources, as discussed in section 3.2.1. The maximum neutron energy obtained with TNSA is about 40 MeV. The choice of the converter material is crucial for optimizing the neutron spectrum for a specific application. When protons or deuterons are accelerated, the most frequently used converters are beryllium and lithium with thicknesses ranging from 0.5 mm to 2 cm, which have been discussed in section 3.2.4. In literature, researchers have also explored the possibilities of using medium Z materials such as copper, zinc, and manganese as converters [reference]. One study by Zagar and his team reported on the production of neutrons using lead as the converter and analyzed the energy spectrum for a proton beam accelerated by the VULCAN laser with an intensity of $\times10^{20}$ W/cm^2, a pulse energy of 400 J, and a pulse duration of 0.7 ps [87, 88]. The resulting neutron spectrum showed that 2×10^9 neutrons per laser shot were generated with a maximum energy of $\approx$35 MeV. However, these results could only be achieved using highly energetic protons, as the cross-section of lead for (p,xn) reactions is significant only for energies greater than 15 MeV [79].

In an experiment conducted by Brenner and colleagues, a bilayer converter consisting of 1 mm of copper and 4 mm of lithium was used [86]. The results showed an increase in neutron yield and stability of the neutron energy spectrum when copper was used, which generated neutrons via the ^{63}Cu(p,n)^{63}Zn reaction. The maximum neutron energy obtained in laser-driven neutron source experiments is related to the maximum kinetic energy of the incident ions and the Q-value of the nuclear reactions. A summary of the studies conducted on laser-ion beam neutron generation experiments is given in table 3.3.

Main features of laser-driven generation experiments		
1	Acceleration schemes	TNSA, BOA, RT
2	Target material	For protons: CH_2, polystyrene, mylar, (Al, Au, Cu)+ H rich contaminants. For deuterons: deuterated polystyrene, CD_2 , D_2O flow
3	Target thickness	hundreds of µm 1 mm
4	Laser pulse duration	40 fs up to few ps
5	Laser energy delivered on target	mJ - 400 J
6	Distance between pitcher and catcher	≈5 mm
7	Converter material	For ion conversion: Li, LiF, Be mainly Au, W, Cu
8	Converter thickness	0.5 mm up to ≈2 cm
9	Maximum energy of neutrons	TNSA≈40 MeV, BOA or RP≈150 MeV, photoneutrons ≈ 4MeV
10	Maximum neutron flux in forward direction	10^{7-9} n/s

Table 3.3: Summary of the main features of laser-driven neutrons generation experiments reported in the literature [79]

.

3.5 Neutrons production by Laser Implosion

Implosion, whereby fusion reactions are triggered by lasers, is the second approach. Deuterium (D) or tritium (T), a cluster of gas jet targets are shot with a high-intensity laser. Through absorbing the energy of the laser pulses, the deuterons are able to surpass the Coulomb barrier and trigger fusion reactions in order to produce fusion neutrons. Plasma's positively charged ions store the coulomb potential energy produced from the laser. Explosions of highly charged clusters are caused by this unstable potential energy, which produces multi-keV deuterium ions. The resulting deuterons have sufficient kinetic energy to fuse inside the cluster jet of gas, generating a burst of monoenergetic neutron pulse with an average energy of 2.45 MeV [11].

Neutron source from laser triggered fusion reactions was first pioneered by T. Ditmire in 1999. Neutron sources can also be created by Inertial Confinement Fusion (ICF) mechanism. The energetic lasers of 2.1 Mega-joules in the world has been employed by this mechanism at National Ignition Facility (NIF) laser in Lawrence Livermore National Laboratory (LLNL) of about 30 kilo-joules to compress deuterium-tritium (D-T) mixed gas targets encapsulated in spherical shells of high atomic number through plasma shock waves [11].

Experimental evidence for neutron generation by laser implosion has been shown in a variety of single-shot lasers, with much greater neutron production per pulse compared to other laser-driven cases. Therefore, in theory, the implosion neutron source is the most powerful among the many laser neutron sources [14, 16]. This method is based on two process, The direct drive and indirect drive implosions. The surface of a target is directly bombarded by laser beams in the direct drive implosion. Indirect-drive implosion, on the other hand, converts the driver energy into soft x-rays that fill a cavity as quasi-black body radiation. A pellet's surface absorbs soft x-rays, generating ablation pressure that drives the implosion [21]. Fig. 3.9 depicts their concepts in schematic form.

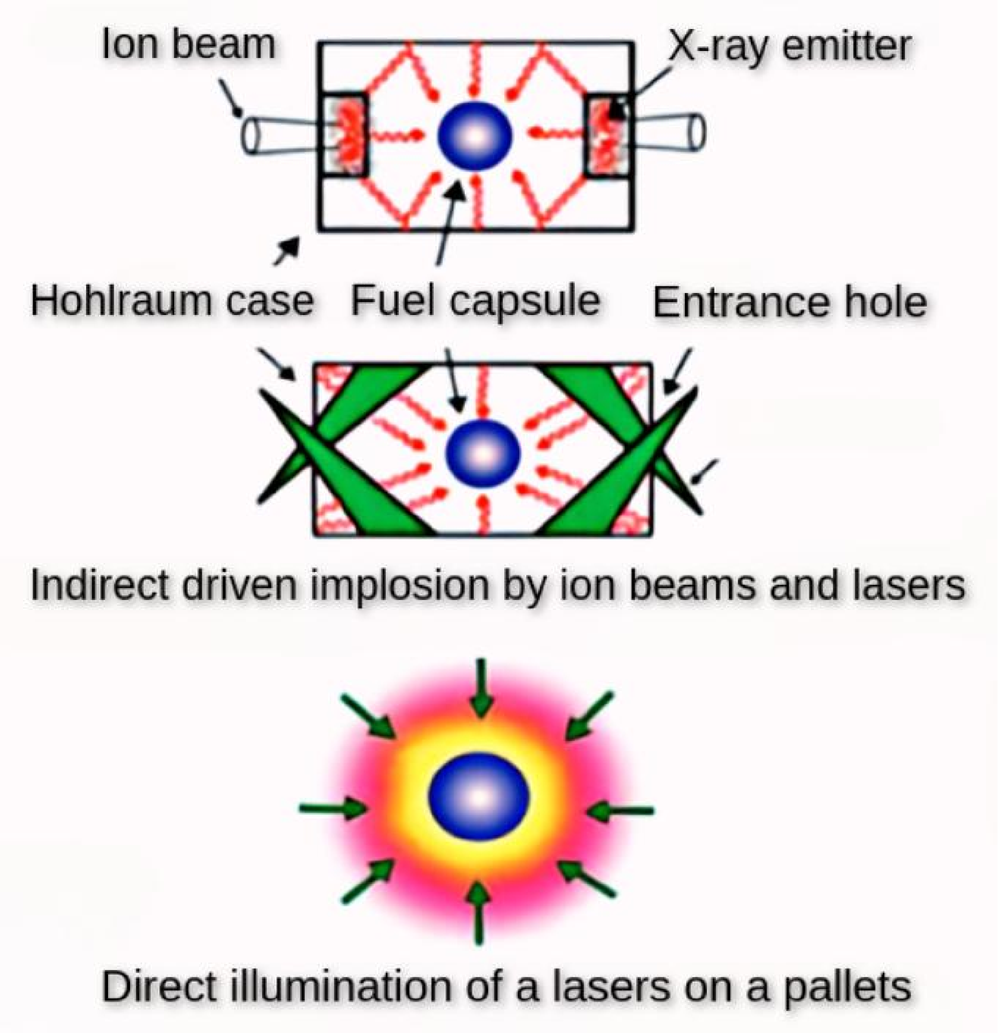

Figure 3.9: Laser generation Implosion schemes: Direct drive implosion and Indirect-drive implosion [14]

.

In a thermo-nuclear mechanism, the fuel number density n is depleted by nuclear reaction as:

$$\frac{dn}{dt} = -n^2 \frac{\langle \sigma v \rangle}{2} \tag{3.16}$$

Here, σ is fusion cross section and $\langle \sigma v \rangle$ is the average over the energy distribution of D and T. For a constant $\langle \sigma v \rangle$ over time, the expression for the fuel density can be written as:

$$n = \frac{n_0}{1 + \frac{n_0 \langle \sigma v \rangle}{2}} \tag{3.17}$$

Therefore, the burning fraction Φ is given by:

$$\Phi = 1 - \frac{n}{n_0} \tag{3.18}$$

By inserting n, it will become:

$$\Phi = \frac{\frac{n_0\langle\sigma v\rangle}{2}}{1 + \frac{n_0\langle\sigma v\rangle}{2}} \tag{3.19}$$

The duration of sustaining plasma confinement determines the fusion reaction time, t. For Inertial Fusion Energy (IFE), where R is the plasma radius and C_s is the speed of sound, given as t = $\frac{R}{4C_s}$. Burning fraction as a function of ρR is gievn as:

$$\Phi = \frac{\rho R}{A + \rho R} \tag{3.20}$$

Here A is a function of temperature and it is approximately equals to $10/(\mathrm{T}/10keV)^2$ g/cm^2 for DT reaction. It gievs the neutron yield of:

$$Y = \frac{N\Phi}{2} \tag{3.21}$$

where N is equals to $\frac{n_0}{\frac{4\pi R^3}{3}}$. If the energy of laser pulse which heats the DT fuel is E_L and η is the energy coupling efficiency of laser to the reacting plasma, Mathematically it can be written as $\eta E_L = 3NT$. When $\rho R <<$ A, and Y becomes equal to $\frac{N\rho R}{A}$ and is proportional to $(\frac{E_L}{T})^{\frac{4}{3}}$ $(\frac{\rho}{\rho_s})^{\frac{2}{3}}$. Here ρ_s is the initial DT denisty and T shows temperature.

3.6 Neutrons Production by N-γ Processes

Bremsstrahlung radiation and photo-induced nuclear (γ, n) and (γ, fission) processes can be employed to produce neutrons using relativistic electron beams from laser-driven accelerators [21, 58]. This approach is similar to ion-driven neutron sources, depending on the initial acceleration of electrons from gas targets to relativistic speeds. It can be acheived through the laser wakefield acceleration (LWFA) [25] and direct laser acceleration techniques [26]. Bremsstrahlung radiation in the MeV range is generated when relativistic electrons are decelerated by interacting with the bulk material. The emitted x-rays may cause photo-induced nuclear reactions, whereby the neutrons are produced by the excited nuclei in the vicinity. [14]. The overall view of this scheme is summarized in Fig. 3.10.

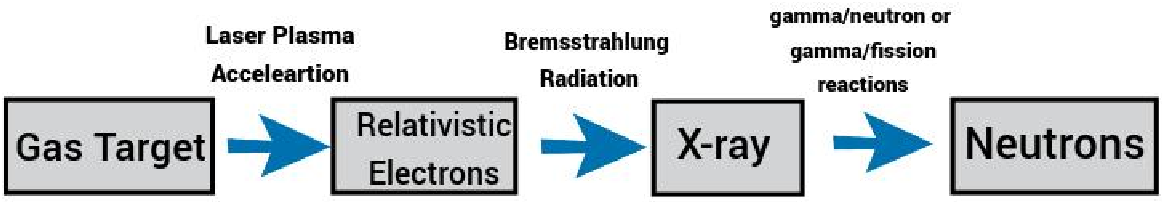

Figure 3.10: General view of electron driven neutron source production
.

In this process, electrons accelerated from LWFA to multi tens of MeV are transferred to the converter made of high-Z nculei. The high-Z material in the converter scatters high energy electrons, which emits X-rays with an energy scale equal to that of electrons. The nuclei will absorb the X-rays, which typically have energies higher than the nuclear binding energy, which will trigger photon neutron (γ,n) reactions and results in production of neutrons from nuclei. This method, however, is significantly less effective than the ion-driven neutron process. The efficiency of converting laser energy to photon via Bremsstrahlung is less than 1%, whereas the efficiency of converting laser energy to proton can be as high as 10% [21]. Furthermore, cross-sections for (p,xn) reactions are larger than those for (γ,f) or (γ, xn) reactions [14,25]. Therefore, this method of producing γ rays and neutrons has been set aside and other ways are being studied such as inverse Compton scattering [14,15].

3.6.1 Laser Wakefield Acceleration (LWFA)

LWFA is the most efficient mechanism for accelerating electrons using laser among all other laser-plasma acceleration techniques [25]. It is based on an idea proposed even before the invention of the laser. In 1956, Akhiezer and Polovin were the first to describe the evolution of these plasma waves. In 1979, Tajima and Dawson presented the concept of accelerating electrons using a laser-excited plasma wave [11]. In this mechanism, electric field of an intense laser pulse of about $10^{17} W/cm^2$ interacts with a gas target, suppressing the nuclear electric field in atoms and free the electrons from their bound states by a process called as barrier-suppression ionization [25].The fluctuating laser pulse intensity causes ponderomotive force in free electrons in the laser field. High-intensity laser pulses liberate a significant number of electrons from their envelopes as they move through ionized gas, exciting enormous amplitude Langmuir waves in the plasma, called the laser wakefield [11]. Due to inhomogeneous electron density distribution in the wave, a strong electrostatic field is created inside the wakefield; Electrons trapped inside the wake are accelerated by the electrostatic field and continue to propagate at speeds near to the speed of light until the laser energy is depleted [11,14]. Fig. 3.11 illustrates the principle of laser wakefield electron acceleration.

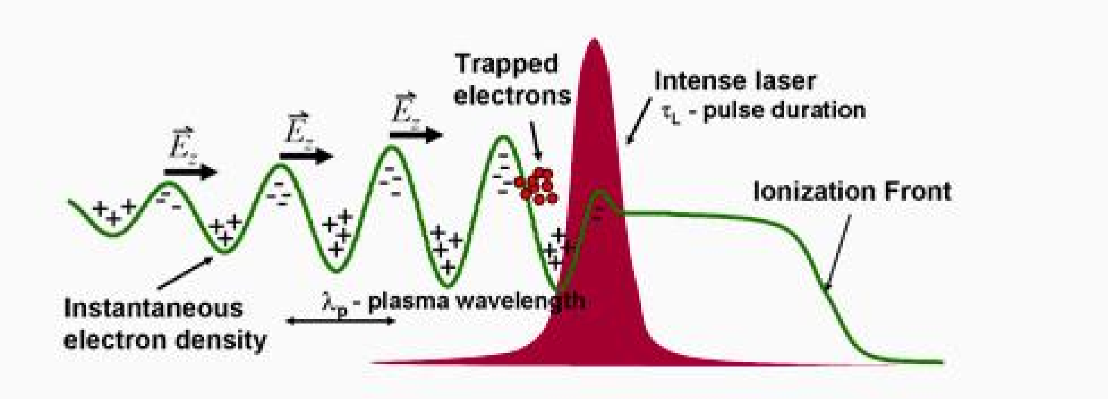

Figure 3.11: Schematic view of stong laser pulse interaction with the low-atomic-number gas i.e., hydrogen or helium. Gas is ionized with the foot of pulse and the wakefield is produced behind the laser. In the proper phase, trapped electrons may be accelerated to extremely high energies. The plasma wave is stimulated efficiently when the plasma wavelength is equal to the laser pulse duration. Image from:https://cuos.engin.umich.edu/ researchgroups / hfs / research / laser-wakefield-acceleration

.

Earlier, the quality of accelerated electron bunch was not very promising for practical applications. The exponential distribution of the accelerated electron beams have short, high-energy tail that extends over 100 MeV. When quasi-monoenergetic electron bunches with high charge of >100 pC, high energy of >100 MeV, and low divergence of around < 10 mrad were created in the 2000s [11]. Currently, a single short laser pulse of high intensity is used to drive the typical LWFA in an under dense plasma environment. It became possible upon adjusting the laser and plasma parameters to match the acceleration length to the dephasing length. This technqiue is under rapid development and have not been exploited in practical applications. However, Center of Ultrafast Optical Science (CUOS) researchers are among the first ones to observe quasi-monoenergetic electron beams up to 300 MeV emerging from the laser wakefield with longer laser pulses of 30 fs by suing a 40 TW Ti:sapphire Hercules laser with an intensity of 10^{19} W/cm^2 onto a supersonic 2 millimeter He gas jet [27–29]. The schematic of the experiment is presented in Fig: 3.12.

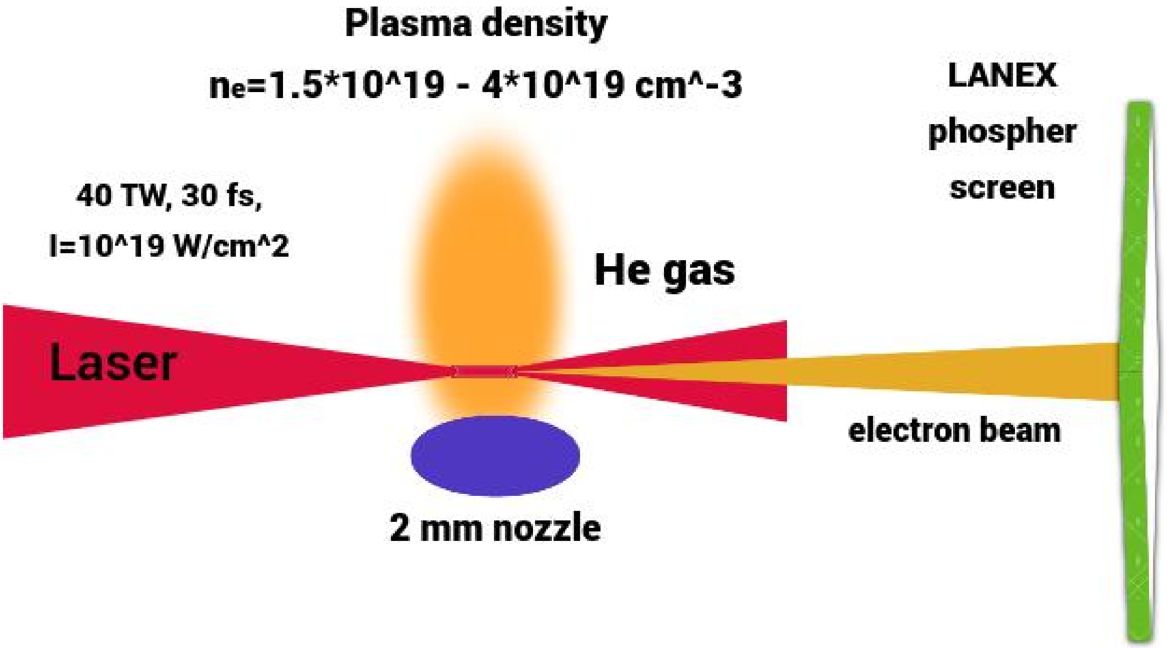

Figure 3.12: Experimental setup of laser wakefield electron acceleration from gas jet target. Image from:https://cuos.engin.umich.edu/researchgroups/hfs/research/laser-wakefield-acceleration

.

Chapter 4

Scintillation Detectors

4.1 Introduction

Scintillators are radiation detectors used to detect radiation in many nuclear technology applications such as high energy physics (HEP), medical imaging, and homeland security. Scintillators produces scintillations of light when ionizing radiation passes through the scintillation material, allowing the high-energy section of the spectrum to be determined. A scintillator was the first solid substance to be employed as a particle detector. William Crookes was the first to observe scintillations caused by alpha particles impinging on a ZnS screen in 1903. In Rutherford's experiment setup in 1910, alpha particles collided with a zinc sulfide screen and created scintillations, which were counted with or without the use of a microscope, a very inefficient, inaccurate, and time-consuming method. After a 30-year the approach was revived when upgraded electronics enabled the amplification of the light emitted by the scintillator [4].

The absorbed photons or particles activate the detector's material to luminescence (emission of visible or near-visible light photons) in scintillation detectors. The amount of light generated by the scintillator is very small. Therefore, it is amplified before being recorded as a pulse. The light from the scintillator is amplified or multiplied using a device known as a photomultiplier tube (PMT). PMT receives a small amount of light, amplifies it many times, and outputs a strong pulse. Many commercial photomultiplier tubes, have amplifications on the order of 10^6. A detection system that uses a scintillator is shown in Fig. 4.1. The operation of a scintillation detector may be divided into two broad steps [39]:

1. The scintillator absorbs incident radiation energy and produces photons in the visible region of the electromagnetic spectrum.
2. The output pulse is produced when the light is amplified by the photomultiplier tube.

Scintillator-based detectors are made up of a scintillator material and a photodetector, which can be a photomultiplier tube or a photodiode. Inorganic crystals and organic scintillators are the two most used types of scintillators. These two types of scintillators have different scintillation mechanisms. Despite this, there is no perfect scintillation substance that encompasses all characteristics. Inorganic scintillators has slow time response than organic scintillators, but they provides the best light output and linearity. While in organic scintillators the light production is lower but the time response is faster. When choosing a scintillator, you always have to give up some features for others. The type of particle to be found also affects the choice of detector. Due to their high atomic number and high density, inorganic scintillators are more often used to detect photons. On the other hand, organic scintillators are more often used to detect fast neutrons because they contain a large ratio of hydrogen. [4].

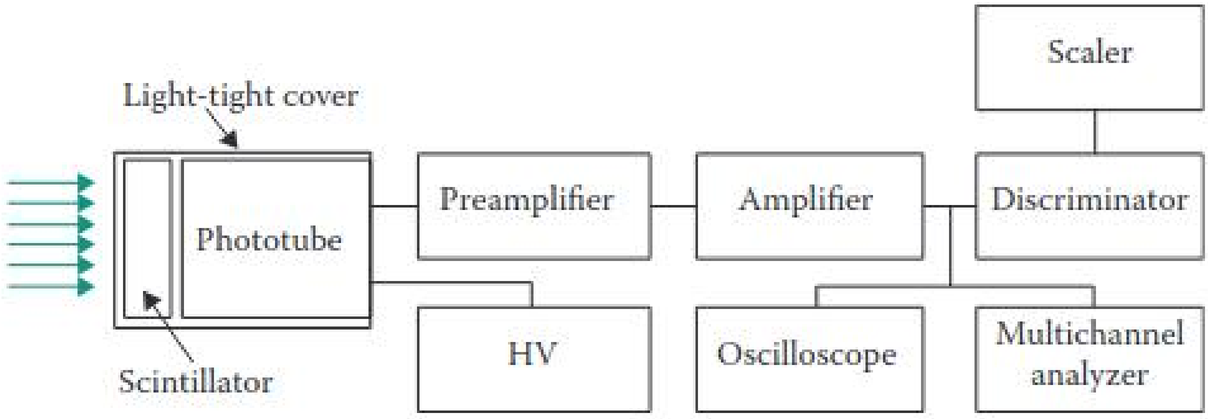

Figure 4.1: A detection system using a scintillator [39]

.

Photomultiplier Tube (PMT)

A photomultiplier is an electronic device that converts incident photons from a scintillator into an electrical signal. The photoelectric effect allows photomultiplier tubes to absorb the light emitted by the scintillator and re-emit it in the form of electrons. PMTs can generate electrical pulses from a few hundred visible photons. The photomultiplier photocathode generates nearly the same number of photoelectrons as the crystal's enormous number of low-energy photons. Since the development of photocathodes and secondary emission multipliers (dynodes), PMTs have made tremendous progress. Fig. 4.2 shows the schematic construction of a photomultiplier tube.It is made up of an anode, dynodes, and a photocathode. When light from the scintillator hits the photocathode, the photoelectric effect causes photoelectrons to be made, which are then sent to the first dynode by a potential difference. When photoelectrons hit the dynode, they make the dynode give off more electrons, which are then sped up to the next dynode, and so on, until the electrons are amplified enough to reach the cathode. Finally, all of these electrons are collected in the photomultiplier's anode, generating a current that the electronic nuclear chain can process [40, 41].

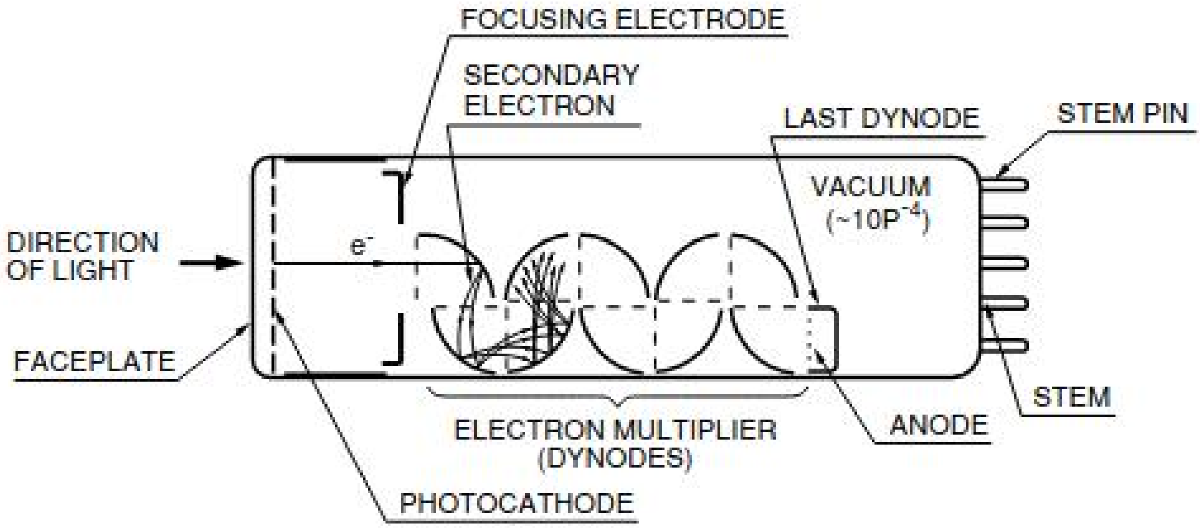

Figure 4.2: Schematic construction of a photomultiplier tube (PMT) [40]

.

4.2 Organic Scintillators

Organic scintillators follows the passage of a charged particle or a photon, provides the measurable photons in the visible range of the light spectrum. These scintillators belongs to the class of aromatic compounds. They are composed up of planar molecules with benzenoid rings such as Toluene and anthracene structures, shown in Fig. 4.3. They are categorised as unitary, binary, ternary, depending on the number of chemicals in the mixture. The chemical with the highest concentration is the solvent and solute. A ternary scintillator has a solvent, a primary solute, and a secondary solute, whereas a binary scintillator just contains a solvent and a solute. The most often used compounds in organic scintillators list in given table. 4.1 [39].

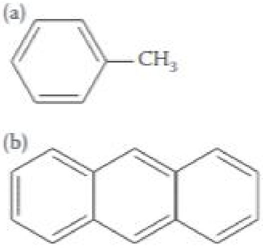

Figure 4.3: Molecular structure of (a) toluene and (b) anthracene [39]

.

4.2.1 Scintillation Mechanism In Organic Materials

Scintillation mechanism in organic materials is determined in many respects by initial conditions of exited states generation. This process depends on aspects of interaction of ionizing radiation with organic materials and conditions of generation and energy exchange of charge states [3]. Organic scintillators are usually used as activated and pure single crystals, or as objects with amorphous structure (i.e. plastics and liquid scintillators). The radioluminescence mechanism for organic crystals, plastics and liquids is different [42].

Organic scintillators are made up of organic molecule crystals with *pi*-electron configurations that are weakly bound by Van der Waals forces [5]. The structure of an organic molecule is determined by the electronic configuration of the carbon atoms; the electronic configuration of the ground state of a carbon atom is $1s^2\ 2s^2\ 2p^2$, and when carbon is combined with other elements to form compounds, one of the electrons in the 2s shell is excited into the 2p shell, which results in the following configuration: These four valence electron orbitals, $1\mathrm{s}^2\ 2\mathrm{s}^1\ 2\mathrm{p}^3$, may be combined to generate a wide variety of different configurations. When two lobes of an orbital on one atom overlap with the two lobes of another atom laterally, a covalent chemical bonding occurs in the *pi*-electron structure of a molecule [42].

The luminescence in material is caused by the excitation of these *pi*-electrons systems. Fig. 4.4 shows the *pi*-electronic energy levels of a molecule. The system is composed of two states, the singlets state where the spin is equal to zero $(S_0, S_1, S_2,...)$ and the triplets states where the spin is equal to one $(T_0, T_1, T_2,...)$. The energy spacing between S_0 and S_1 is around 3 or 4 eV, and each electronic configuration is subdivided into vibrational states $(S_{00}, S_{01},..)$ of the molecules, where the spacing energy is of the order of 0.15 eV [43].

Organic Scintillator Compounds			
S.No	Compound	Formula	Application
1	Benzene	C_6H_6	S
2	Toulene	$C_6H_5CH_3$	S
3	p-Xylene	$C_6H_4(CH_3)_3$	S
4	1,2,4-Trimethylbenzene	$C_6H_3(CH_3)_3$	S
5	Hexamethylbenzene	$C_6(CH_3)_6$	S
6	Styrene monomer	$C_6H_5C_2H_3$	S
7	Vinyltoluene monomer	$C_6H_4CH_3C_2H_3$	S
8	Napthalene	$C_{10}H_8$	S',C
9	Anthracene	$C_{14}H_{10}$	C
10	Biphenyl	$C_{12}H_{10}$	S'
11	p-Terphenyl	$C_{18}H_{14}$	C,PS
12	p-Quaterphenyl	$C_{24}H_{18}$	C
13	trans-stilbene	$C_{14}H_{12}$	C
14	Diphenylacetylene	$C_{14}H_{10}$	C
15	$1,1',4,4'$-Tetraphenylbutadiene	$C_{28}H_{22}$	SS
16	Diphenylstilbene	$C_{26}H_{20}$	SS
17	PPO(2,5-diphenylloxazole)	$C_{15}H_{11}NO$	PS
Source: Brooks, F., Nucl. Instrum. Meth. 162:477;1979.			
S-primary solvent; S'-secondary solvent; PS-primary solute; SS-secondary solute; S-crystal scintillator			

Table 4.1: Organic Scintillator Compounds [39]

.

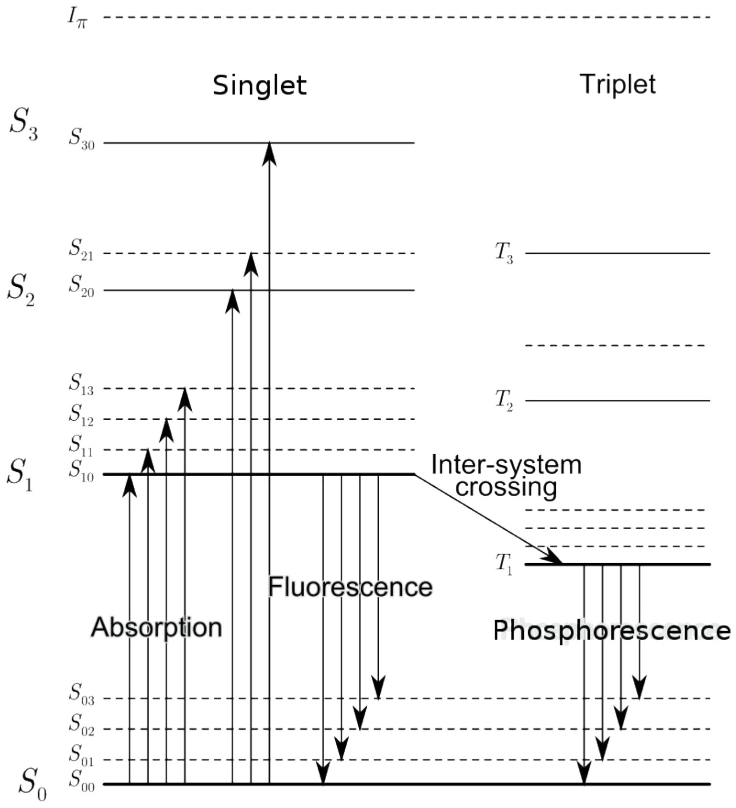

Figure 4.4: Energy levels of an organic molecule with π-electron structure [43]

.

When a charged particle passes through the scintillator, part of its kinetic energy is released in the material and is absorbed by the molecules, causing electrons to be excited to higher states S_1, S_2, S_3. After some picoseconds, the singlets are de-excited into the S_{10} state through internal transitions where no light is emitted, and then the fluorescence is obtained when all these electronic states go from to S_{10} to any vibrational state of the ground state (S_{00},S_{01},S_{02}). The intensity of this prompt fluorescence at a time t can be obtained with the following expression:

$$I = I_0 e^{-t/\tau} \tag{4.1}$$

where as τ represents the fluorescence decay time for the S_{10} level.

In most organic scintillators, there is a transition known as “intersystem crossing”, which involves spin orbit coupling. In these scintillators, the triplet state (T_1) is populated by transitions from the S_{10} state in order of a few nanoseconds and are fast. The light emitted from the T_1 to the singlet ground state is called phosphorescence. The phosphorescent light can be discriminated from the scintillation light on the basis of timing and wavelength. The light emitted when a molecule in the triplet state (T_1) acquires enough thermal activation energy over time to decay return to the singlet state S_1 and eventually decay to the singlet ground state is known as delayed fluorescence. The emission of this type of luminescence depends on the characteristic of the particle detected, therefore a particle discrimination technique consists of the analyses of the proportion of delayed fluorescence and prompt fluorescence. Most all the fluorescence transitions have lower energy than the energy requires for the absorption (excitation), therefore the light emitted by fluorescence passes directly through the scintillation medium [43].

The efficiency with which a scintillator converts particle energy into visible light is known as its scintillation efficiency. However, only a tiny fraction of the kinetic energy deposited by a particle in the material is converted to light; the remainder is generally squandered as heat or lattice vibrations. All dissipation processes that result in a loss of the particle's kinetic energy are referred to as quenching. As a result, it is critical to eliminate contaminants (such as oxygen) that might cause alternative quenching processes for the excitation energy during the production of organic scintillators. The kind of particle and its energy will always have an impact on the conversion of particle energy to light yield. When the energies above 125 keV, the electron response in most organic scintillators is linear. The response of heavy charged particles, on the other hand, is not linear; it is always less than the incident energy. This is why the absolute light yield is stated in a unique way. MeVee (MeV electron equivalent) is a unit of measurement for the quantity of light emitted by different particles in a scintillator. For example, a 1 MeV electron will create 1 MeVee of light if it deposits all of its energy in the detector, while an heavy charged particle will require more energy to do so [43, 44].

When no quenching occurs, the light response of an organic scintillator to charged particles is proportional to the energy loss, as shown by the following relationship:

$$\frac{dL}{dx} = S\frac{dE}{dx} \tag{4.2}$$

where $\frac{dL}{dx}$ is the fluorescent energy emitted per unit path length, $\frac{dE}{dx}$ is the charged particle's particular energy loss, and S is the typical scintillation efficiency.

The energy loss ($\frac{dE}{dx}$) is sufficiently small, when the material is excited by fast electrons: mathematically, it can be written as:

$$\left.\frac{dL}{dE}\right|_e = S \longrightarrow L = \int_0^E \frac{dL}{dE}\, dE = SE \tag{4.3}$$

This backs up the statement that the light sensitivity of the electrons in organic scintillators is linearly proportional to the particle's energy. When there are quenching effects, on the other hand, the Birks formula can be used to characterize these situations:

$$\frac{dL}{dx} = \frac{S\dfrac{dE}{dx}}{1 + kB\dfrac{dE}{dx}} \tag{4.4}$$

where B is a proportionality constant and k is a fraction that represents the particles that pass through the quenching effect. The energy loss $\left(\dfrac{dE}{dx}\right)$ in the case of alpha particles very high, therefore a saturation occurs, and the Birks formula becomes the following way:

$$\left.\frac{dL}{dx}\right|_a = \frac{S}{k_B} \tag{4.5}$$

k_B can be determined by:

$$k_B = \frac{\left.\dfrac{dL}{dE}\right|_e}{\left.\dfrac{dL}{dx}\right|_\alpha} \tag{4.6}$$

whereas, k_B determines the response of an organic scintillator to an electron and an alpha particle of the same energy [43].

4.2.2 Types of Organic Scintillators

Organic Liquid Scintillators

Kellman and Reynolds et al. codiscovered liquid scintillator counting in 1950. In the life sciences, it has been extensively employed with radioactive tracers research. Organic liquid scintillators are made up of a suitable solvent mixture containing one or more solutes. Xylene, toluene, and hexamethylbenzene are examples of solvents that have worked well (see Table 4.1). Liquid scintillators can be made up of just the two components, or three, a third contitutent called a wavelength shifter is sometimes added to tune the emission spectrum to better match the spectral response of standard photomultiplier tubes [4, 39].

Liquid scintillators are very useful for neutron and gamma rays detection using wavelets, classical versus evolved quenching parameters and procedures in scintillation measurements. They also provide low-cost alternatives to other scintillators when a large-volume detector is required to boost efficiency. Different base materials create Pulse Shape Discrimination characteristics, high flash points, low or high temperature performance, and other qualities. To boost neutron or photon cross-sections, certain liquid scintillators are filled with organo-metallic compounds.

In the same way as solid scintillators, liquid scintillators are sealed in clean, dry, chemically inert gas containers. They are deoxygenated before usage to ensure that the scintillators achieve their optimum performance. These scintillators are commonly used to count radioactive materials that dissolve in the scintillator solution. In this case, all radiations released by the source pass through some section of the scintillator which results in 100% counting efficiency. Low-level beta activity, such as that from ^{14}C or tritium, is commonly counted using this technique. Counting low-activity -emitters (^{3}H and ^{14}C in particular), cosmic ray detection, and measurement of the energy spectrum of neutrons in the MeV range using the scintillator NE 213 are just a few examples [4, 45].

Liquid scintillators can be obtained and used in large volumes (kiloliters), it can also be used to create a detector of desired size and shape in a suitable container. We have listed some of the most often used liquid scintillators, along with their uses in table 4.2

Liquid organic scintillators			
S.No	Scintillator	Distinguishing Features	Principal Applications
1	BC-501A	excellent PSD properties	$\gamma > 100$ keV, fast n spectrometry
2	BS-505	highest light output, transmission, high flash point	γ, fast n for large volume detectors
3	BC-517L	standard formulation	γ, fast n, cosmic, charged particles
4	BC-517H	high light output standard formulation	γ, fast n, cosmic, charged particles
5	BC-517P	lowest cost, highest H content, high light transmission, highest flash point	γ, fast n, cosmic, charged particles
6	BC517S	highest light output of mineral oil based scintillators	γ, fast n, cosmic, charged particles
7	BC-519	PSD properties	γ, fast n; n-γ descrimination
8	BC-521	Gd loaded	neutron spectrometry, neutrino research
9	BC-523A°	^{10}B loaded; PSD properties	total absorption neutron spectrometry
10	BC-525	Gd loaded; mineral oil base	neutron spectrometry, neutrino research
11	BC-533	for low temperatures, high flash point, low cost large volume detectors	γ, fast n
Source: Brooks, F., Nucl. Instrum. Meth. 162:477;1979.			

Table 4.2: Most common used liquid scintillators and their applications [45]

.

4.3 Inorganic (Crystals) Scintillators

Ionic solid crystals are the most common inorganic scintillators, and they have a high density and temperature. They are divided into two types: single-crystal ceramics and polycrystalline ceramics. In sectors requiring radiation detection under harsh conditions (high radiation, temperature, humidity, vibrations, etc.), single-crystal inorganic scintillators are used, such as well logging, HEP, nuclear reactor monitoring, and space exploration. The reduced optical properties of polycrystalline ceramics limit their use to lower energy radiation detection, where smaller scintillators can be used. Scintillation occurs more slowly in inorganic crystals than in biological crystals. Due to their high density and atomic number, which gives a high electron density, they have a high efficiency for detecting gamma rays and can handle high count rates. The well logging industry uses inorganic crystal scintillators in search of new fuel sources. Inorganic crystals are widely used in medical imaging to detect X-rays or gamma rays [4, 39].

Lithium iodide (LiI), sodium iodide (NaI), cesium iodide (CsI) are examples of inorganic scintillators. The majority of inorganic scintillators are alkali metal crystals, particularly alkali iodides, that contain a minor amount of an impurity. NaI(Tl), NaIL, and CsI(Tl), are among examples. The impurity or activator is the element in parentheses. Although the activator has a low concentration and responsible for the crystal luminosity [39, 43].

NaI Inorganic (Crystals) Scintillator

In scintillation-based radiation detection physics, NaI is one of the inorganic scintillators used for gamma-ray and neutron dual detection. This scintillation detector is appealing because it can be scaled up to enormous proportions, has modest spectroscopy, and is inexpensive. NaI is an Sodium Iodide crystal. It has been found effecient for gamma detection as compared to the other well-known gamma-ray scintillators i.e, CLYC and CLLB [46].

4.3.1 Scintillation Mechanism in Inorganic Scintillators

The luminescence mechanism in inorganic scintillators can be explained in terms of electronic bands (allowed and forbidden energy bands) of a crystal. The electronic structure of an atom consists of energy levels called bands represented as discrete lines, shown in Fig. 4.5. The valence band is full of electrons and corresponds to the ground state of the crystal, then the conduction band which is the uppermost allowed band represents the free electrons, and the band gap is a forbidden region for the electrons [4, 39].

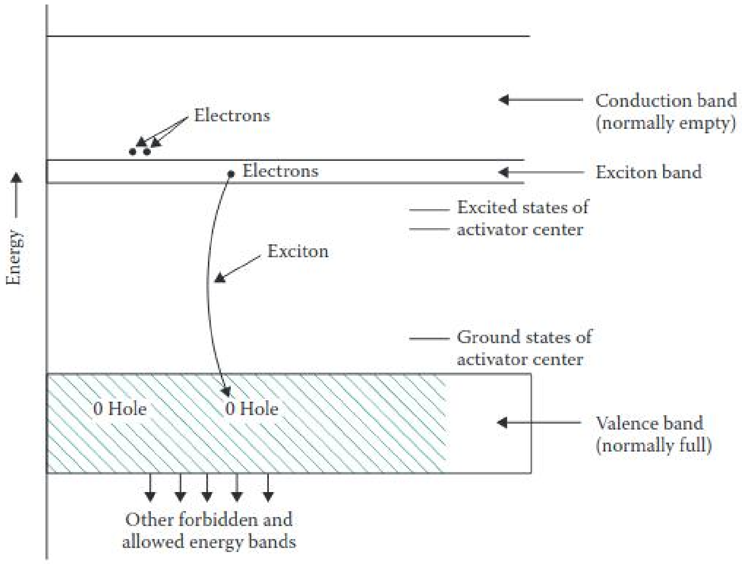

Figure 4.5: Allowed and forbidden energy bands of a crystal [4, 39]

.

When an electron gains enough energy from incoming radiation, it travels from the valence band to the conduction band in the lattice. This electron electron leaves a hole in the valence band that may travel as well. The energy delivered to the electron may not always be sufficient to bring it to the conduction band. Instead, the electron in the valence band stays electrostatically bonded to the hole. The resulting electron-hole pair is known as an exciton. The exciton relates to an electron being elevated to a state higher than the valence but lower than the conduction band in terms of energy states. As a result, the exciton states form a narrow band, the upper level of which coincides with the lower level of the conduction band. The width of the exciton band is around 1 eV, whereas the gap between the valence and conduction bands is about 8 eV. [39].

With this configuration the process of de-excitation is inefficient, and the resulting light would have a wavelength out of the visible spectrum, therefore it can be later reabsorbed by the same material of the detector. Because of crystal defects or impurities, energy states may be generated between the valence and conduction bands, increasing photon emission. Doping with activator atoms such as thallium produces imperfections or impurities. The activator atom may exist in either its ground or excited states. Elevation to an excited state may occur as a consequence of photon absorption (e.g., through photoelectric effect), capture of an exciton, or sequential capture of electron-hole pairs. The transition of the impurity atom from the excited decays to the ground state (valence band) occurs in the emission of a photon with a wavelength in the visible spectrum, which contributes to scintillation in times of the order of 10^{-8} s [4, 39]. The inorganic scintillators have the highest light output in compassion with the organic scintillators but the decay times are longer. Information about the important properties of some inorganic scintillators are given in table: 4.3.

Properties of Certain Inorganic Scintillators					
S.No	Material	λ of Max. Emission (nm)	Relative Scintillation Efficiency %	Decay Time (ns)	Desity (10^3 kg/m^3)
1	NA(TI)	410	100	0.23	3.67
2	CaF_2(Eu)	435	50	0.94	3.18
3	CsI(Na)	420	80	0.63	4.51
4	CsI(TI)	565	45	1.00	4.51
5	$Bi_4Ge_3O_{12}$	480	8	0.30	7.13
6	$CdWO_4$	530	20	0.90	7.90
7	^{6}LiI(Eu)	470	30	0.94	3.49

Table 4.3: Properties of certain inorganic scintillators [39]

.

4.4 Digital n-γ Pulse Shape Discrimination (PSD) in Organic and Inorganic Scintillators

γ rays are constantly present in neutron fields, it is critical to distinguish neutrons from γ rays while detecting neutrons. Pulse shape discrimination (PSD) approaches can distinguish between neutrons and gamma rays. Detectors that combine sensitivity to fast neutrons with n/γ discrimination capabilities can currently detect three forms of radiation simultaneously, namely γ-rays, fast neutrons, and slow neutrons. The use of organic scintillation detectors and inorganic scintillators for neutron and γ-ray pulse shape discrimination (PSD) is a commonly used technique in domains such as nuclear nonproliferation, international safeguards, nuclear material control and accountability, and national security [47, 48].

The liquid scintillators are the most common detectors of in organic scintillators, including the EJ-309B5, which has exhibited the best performance in a mixed field of fast and slow neutrons and gamma-rays, according to Swiderski L. et al. [49]. However, in some applications, the employment of liquid scintillators is deemed risky, owing to the risk of uncontrolled leaking of potentially toxic and/or combustible compounds. F. Brooks first discovered plastic scintillators with n/γ discrimination capability by obtaining pulse shape discrimination (PSD) in plastic scintillators in 1960. The most advanced work was done by groups from Lawrence Livermore National Laboratory (LLNL), CEA Paris- Saclay (France), and the National Academy of Sciences of Ukraine's Institute of Scintillation Materials. It includes PVT-based plastic scintillator, i.e, EJ-276 and EJ-276G. Simultaneously, inorganic neutron scintillators have advanced in order to improve the separation of slow neutron events from those caused by gamma-rays and fast neutrons. Although ^{6}Li loaded scintillators, such as NaIL and CLYC inorganic scintillators, have recently been developed, they are still not readily available from manufacturers [47, 49].

4.4.1 PSD in organic scintillators

The emission of light and the time it takes for it to decay in organic scintillators is determined by the type of the incoming particles. The light is emitted by a prompt fluorescence process with a short decay period of a few nanoseconds, while the rest is emitted by delayed fluorescence with a longer decay time of several hundred nanoseconds. The nature of the exciting particles influences the emission of this slow component which helps to discriminate and differentiate between neutrons, gammas, and heavy charged particles with a technique known as Pulse Shape Discrimination (PSD). The pulse shape generated when fast neutrons and gammas are detected using an organic scintillator is shown in Fig. 4.6, where the fast neutrons are detected through elastic collision with hydrogen atoms, while Photons, are detected by electrons produced by the Compton effect, Therefore, gamma detection results in a lower intensity delay fluorescence than rapid neutron detection . [43, 44]

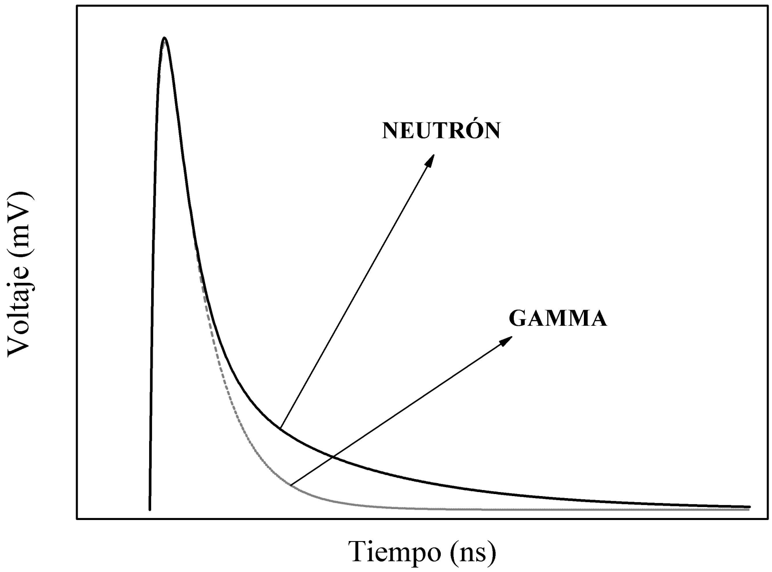

Figure 4.6: Typical pulses shape recorded for neutrons and photons in an organic detector with a PMT. Figure taken from [44]

The delayed fluorescence is produced by excited molecules that attain the triplet state (T_1), collect enough thermal activation energy over time and return to the singlet state S_1, and then decay to the singlet ground state. Density of excited molecules in the triplet state (T_1) is directly proportional to the intensity of delayed fluorescence generated by a single ionizing particle, and is also directly proportional to the density of excited molecules in the singlet state (S_1). Moreover, The excitation of molecules to the singlet state is dependent on energy loss $\left(\frac{dE}{dx}\right)$ of the ionizing particle along the trajectory, the rate of energy loss $\left(\frac{dE}{dx}\right)$ is proportional to the delay fluorescence [43, 44].

4.4.2 Pulse Shape Descrimination (PSD) Characteristics

In a scintillator, the pulse shape discrimination (PSD) helps in the detection of neutron capture and γ emission, as well as the determination of FOM, efficiency, and energy calibration.

4.4.3 Figure of Merit (FoM)

A figure of merit (FOM) parameter calculation can be used to quantify the quality of separation between energy ranges of neutron and gamma produced plumes in the scintillator. A histogram, also known as a PSD plot in Fig. 4.7, that displays the ratio between the two charge integrations of each pulse and can be used to calculate the FOM parameter. Each event indicates a different type of particle identified in the same scintillator (i.e., photons and neutrons). The FoM parameter can be calculated using the following equation: [50]

$$FoM = \frac{m_2 - m_1}{FWHM_n + FWHM_\gamma} \tag{4.7}$$

where m_2 and m_1 are the corresponding discrimination index (centroids of the peaks) for neutron and gamma peaks from a normal distribution fitting of the data and FWHM is the full-width at half-maximum for both particles. An example is shown in Fig. 4.7.

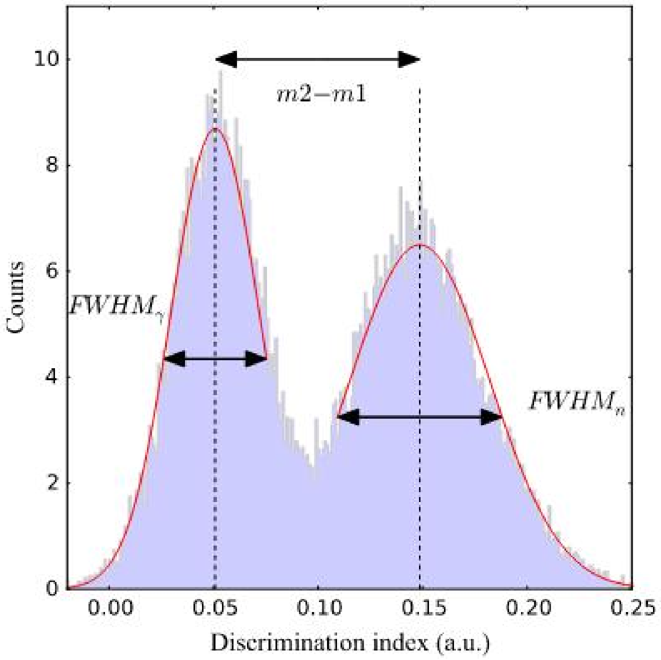

Figure 4.7: Illustration of FoM for pulse shape discrimination, PSD plot for both neutron events (the right hand distribution) and gamma events (the left hand distribution). The peak separation of the two normal distributions is divided by the sum of these two FWHM values [50]

.

The larger the FoM value, the better the system discrimination. It is considered that if the FoM is greater than 1 a good discrimination is obtained, and if it is greater than 1.27 a complete discrimination is achieved, the 1.27 comes from doing the difference of the centroids equal to 2σ, therefore the FoM becomes $FoM = \frac{3\sigma}{2.35\sigma}$=1.27.

4.4.4 n-γ Efficiency

The detection efficiency of a detector system is determined by a number of factors, and multiple efficiency definitions are employed to account for those factors. Absolute and intrinsic efficiencies are the two forms of efficiencies. Both efficiencies are primarily determined by the detector material, radiation energy, and detector thickness in the direction of incident radiation [43].

The absolute efficiency

Absolute efficiency illustrates the relationship between the number of counts recorded by the detector and the number of particles (photons or neutrons) released by the source in all directions; it's impacted by the detector's properties and shape. Mathematically,The absolute efficiency is defined by the following equation:

$$\epsilon_{abs} = \frac{Area_{neta}}{t_{life}.\gamma.A(t)} \tag{4.8}$$

whereas, $Area_{neta}$ is the area under the spectrum curve, t_{life} is the counting time, and $A(t)$ is the source's activity at the time of the experiment. [43].

The intrinsic efficiency

The detector intrinsic efficiency is measured as the ratio of the number of pulses recorded to the number of particles striking the detector [43]. The relationship between the absolute and intrinsic efficiencies in the case of an isotropic source can be represented as follows:

$$\epsilon_{int} = \epsilon_{abs}.\frac{4\pi}{\Omega} \tag{4.9}$$

where Ω presents solid angle of detector seen from the position of the source.

Full-energy peak (or photopeak) efficiency

Phtopeak efficiency is achieved by creating full-energy peak gamma ray bursts. Since plastic scintillators are composed of C and H atoms, and the detector's volume is inadequate, there is no full energy absorption peak in the spectrum, and photons largely interact through Compton Scattering. The detector's response depends on the Compton distribution of recoil electrons. The Klein Nishina formula can be used to forecast the distribution of Compton events [43].

$$\frac{d\sigma}{dT} = \frac{\pi r_e^2}{m_e c^2 \alpha^2}\left(2 + \frac{s^2}{\alpha^2(1-s)^2} + \frac{s}{(1-s)}(s - \frac{2}{\alpha})\right) \tag{4.10}$$

Here, T is the kinetic energy of scattered electron,and r_e the classical electron radius, $\alpha = h\nu/m_e c^2$, $s = T/h\nu$ and $h\nu$ is the initial energy of photon [51].

Depending on the detector's energy resolution, the maximum value in the Compton events distribution can be moved to lower or higher energies. When multiple dispersion is not taken into account, and the gamma rays have only one type of energy, the Compton distribution looks like the curve (a) in

Fig.4.8, no Gaussian smooth is applied in this case. Therefore the area under the curve (a) in Fig. 4.8, defined to be the sum of all the counts recorded by the detectors, and it is equivalent to the absolute efficiency for Gamma-rays, for a given incident energy.

Similar to gamma rays, neutrons also produce a fluorescent response in organic scintillators. For mono-energetic neutrons, the distribution should range from zero to the incident energy of the neutrons, and this is dictated by the recoil protons generated in elastic collisions between the neutrons and the hydrogen atoms. This means that the sum of all the events is equal to the absolute efficiency for neutrons with a given incident energy [44].

4.4.5 Energy resolution and energy calibration

As the gamma-ray response in organic scintillators is proportional to the Compton distribution induced by the recoil electrons, the energy resolution and energy calibration are intimately connected. The Compton edge for incident gamma-ray energy is calculated using the famous equation:

$$E_{Compton} = \frac{E_\gamma}{m_e c^2/2E_\gamma + 1} \tag{4.11}$$

where E_γ is the incoming gamma-ray energy and $m_e.c^2$ is the electron's rest energy Nonetheless, when the detector's resolution is weak, the distribution may be pushed to lower energies. This impact is shown in Fig. 4.8, where the theoretical Compton distributions are presented for a given incident energy and with various Gaussian smooth functions. The Gaussian smooth functions replicate the detector's total pulse height resolution.

Since the displacement of the Compton distribution and the detector's resolution are related, it is possible to figure out the detector's energy resolution by fitting the spectrum to a theoretical Compton distribution. First, the pulses of a radioactive source with known gamma energies are measured with a high degree of accuracy. Then, a set of theoretical Compton distributions with different values of σ are re-produced. Finally, a χ^2 analysis can be used to find the σ that fits the data the best.

Following expression is used to define Gaussian function:

$$G(E) = \frac{1}{\sigma\sqrt{2\pi}}.e^{-\frac{(E-E_0)^2}{2\sigma^2}} \tag{4.12}$$

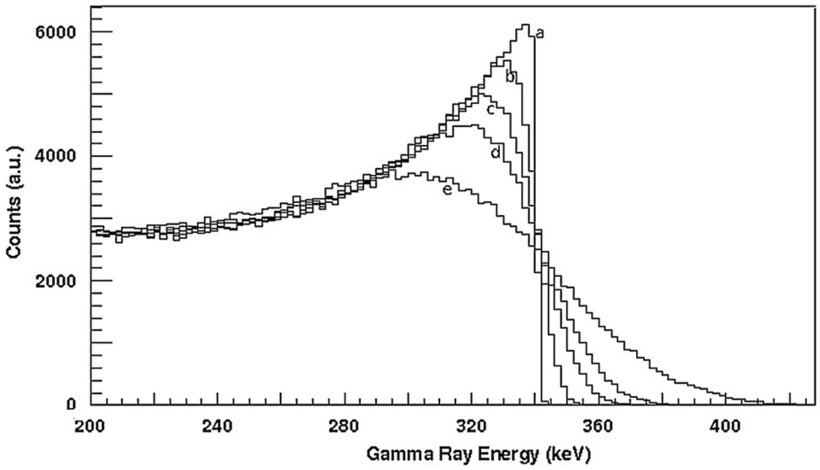

Figure 4.8: Compton scattered event distributions computed without (a) and with various Gaussian smoothes corresponding to pulse resolutions of 5 keV (b), 10 keV (c), 15 keV (d), and 25 keV (e). Figure taken from [51]

.

Chapter 5

Experimental Setup

5.1 Experiments and Methods

In this chapter, we explain all the materials, instrumentation system, and the electronic chain used in laboratory for the readout and the characteristics of the sources, and calibration tests of both organic liquid scintillator EJ-309, and inorganic $LaBr_3$ scintillators. The schematic view of these scintillators is shown in Fig: 5.1. The characteristics and properties of these scintillator are also described in this lesson.

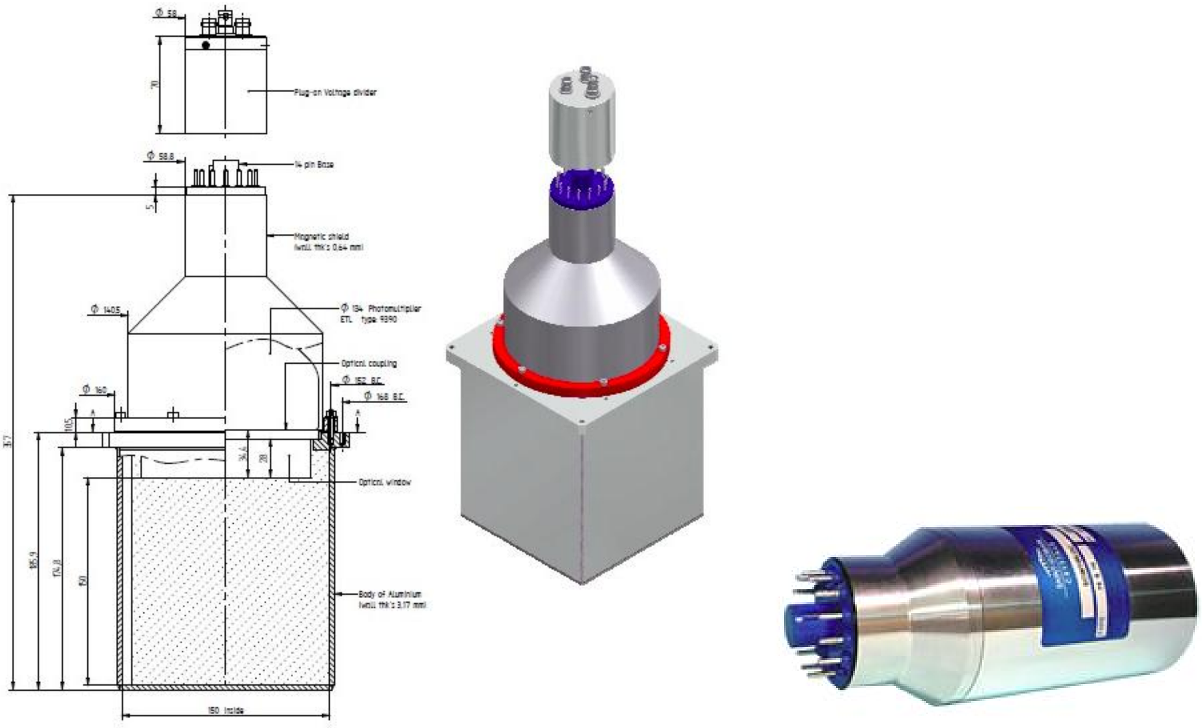

Figure 5.1: Schematic view of (a) 6”×6” active volume EJ-309 liquid scintillation detector (b) Lanthanum Bromide, or $LaBr_3(Ce)$, of 2”×2” a new generation of inorganic scintillation gamma-ray detector.

5.1.1 Organic Liquid scintillators EJ-309

A large organic liquid scintillator EJ-309 (from Scionix Holland B.V. Netherlands) of 6”×6” with good capability discrimination between gamma-ray and neutrons was tested with ^{252}Cf neutron source. The EJ-309 scintillator is shown in Fig: 5.2. It provides an excellent pulse shape discrimination (PSD), for fast neutron spectrometry. The EJ-309 liquid scintillator has a poorer PSD performance but it has been developed with some chemical properties that allows its use in places with difficult environmental conditions. These properties include: low vapor pressure, high flash point, low chemical toxicity, and compatibility with cast acrylic plastics. The main properties of this scintillator are given in Table 5.1 [39, 52].

S.No	Characteristics	EJ-309
1	Light output (% Anthracene)	70
2	Scintillation efficiency (photon yield/MeV e-)	11500
3	Wavelength of maximum emission	423 nm
4	Density (15°C)	0,964 g/cc
5	No. of H Atoms per $\mathbf{cm^3}$ ($\mathbf{x10^{22}}$)	5.44
6	No. of C Atoms per $\mathbf{cm^3}$ ($\mathbf{x10^{22}}$)	4.36
7	No. of Electrons per $\mathbf{cm^3}$ ($\mathbf{x10^{23}}$)	3.15
8	Decay Time, Short Component (ns)	~ 3.5
9	Flash Point (°C)	144
10	Boiling Point (°C at 1 atm)	290-300
11	Vapor Pressure (mm Hg. at 20°C)	0.002

Table 5.1: Characteristics of EJ-309 liquid Scintillator [52]

.

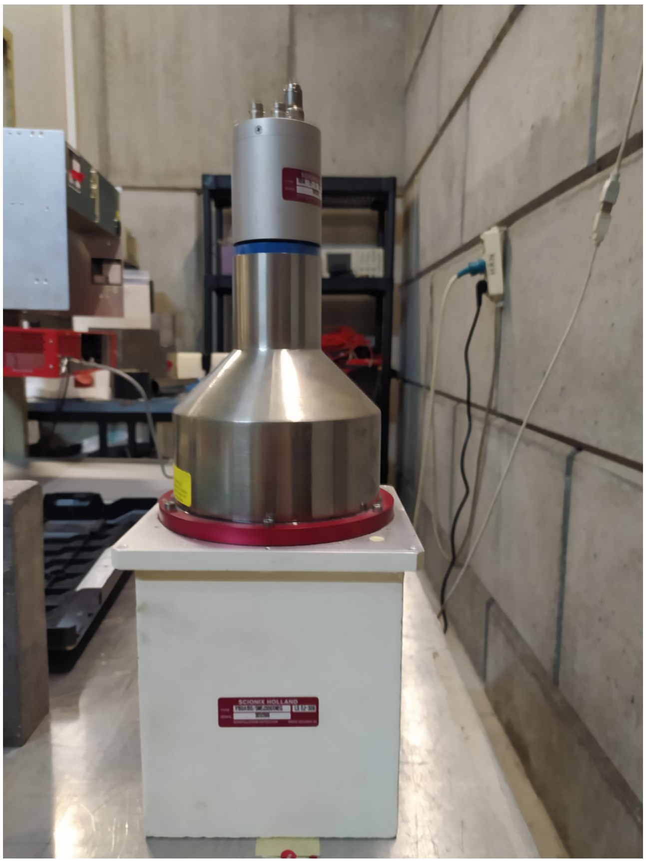

Figure 5.2: 6”×6” EJ-309 liquid scintillator

.

5.1.2 Inorganic Scintillator $\mathbf{LaBr_3}$:Ce

The energy calibration of LaBr was determined by performing measurements in coincidence with a EJ309 detector. The Lanthanum bromide detector is an inorganic scintillator, which has a good timing resolution and energy resolution, also it provides almost a linear response of the signal, mainly for gamma rays with energy values greater than 60 keV. This detector is commonly doped with 0.5 % cerium, and for that percentage of doping the timing resolution is 260 ps, the energy resolution is 3% at 662 keV, and has a light output of 60,000 photons/MeV [4]. The experiment was then performed with the setup shown in Fig. 5.3 to obtain the characteristic gamma emission from graphite with LaBr scintillator. The EJ-309 scintillator was used to obtain the input neutron dose.

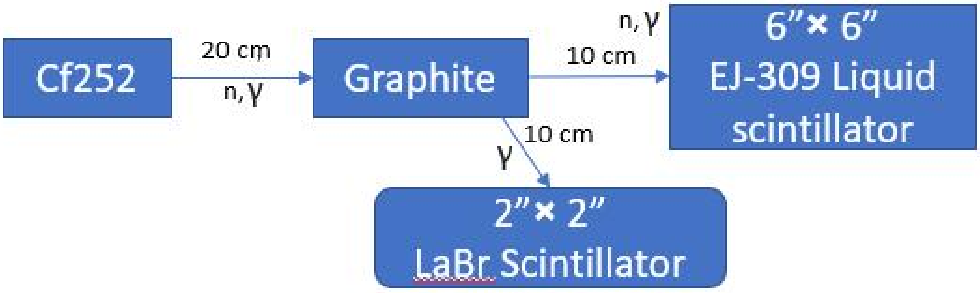

Figure 5.3: Design of experimental setup with 6"×6" EJ-309- 2"×2" LaBr scintillator

5.2 Electronic Instrumentations

5.2.1 High Voltage (HV) Supply

The CAEN model V6533M power supply module type VME [2] 6U, shown in Fig. 5.4 was used to deliver the HV of the PMT ($\sim 1200V$). With an energy range of 0 to 4kV, it is a module that houses 6 HV Power Supply Channels. The three channels have positive output polarity, whereas three of the other channels have negative output polarity. An overvoltage or undervoltage alarm alerts the user when the output voltage is different from the programmed value, and if the current exceeds the programmed limit, an overcurrent detection takes place and the system turns off after a programmed amount of time. The characteristics of this module can be set and the module can be operated remotely thanks to the fact that it can be managed from a computer (through a USB port) [53].

Figure 5.4: HV Power Supply Module CAEN model V6533M

5.2.2 Controller - A USB Port

The Power Supply Module is powered by a tiny micro crate (model VME8004B) made by the CAEN firm, and the USB Port is a CAEN type V1718 that serves as an optical bridge between them, as illustrated in Fig. 5.5. The computer is linked to the module by an optical fiber cable. Five output channels and two input channels are present in this module. Its function is to connect the computer to the electronic nuclear modules with speed of 30 MB/s. For each module in the electronic nuclear chain, the controller V1718 uses a library of particular instructions to translate commands into VMEbus language [53].

---

[2] VME means VERSA Module Eurocard, and corresponds to a standard data transfer architecture of the International Electrotechnical Commission.

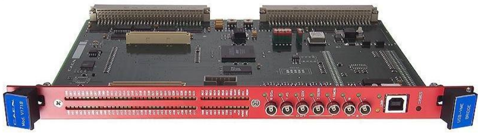

Figure 5.5: USB Port CAEN model V1718

5.2.3 Digitizer

An electronic acquisition tool known as a digitizer captures analog waveform signals, transforms them using analog-to-digital converters (ADC's), and then transfers the sample data to a buffer where it can be saved and later processed and analyzed by a computer. Different modules are needed for traditional digitizers in order to process the signal before extracting the information. Prior to being converted to digital signals, the signals must first be pre-amplified, divided, delayed, and discriminated. There is a need to limit the number of modules since this module chain takes up more space and is more expensive. Additionally, when the signals pass through numerous processes, there is some distortion, loss of linearity, and attenuation.

Modern digitizers can perform the ADC conversion very close to the detector thanks to technological advancements; they are based on programmable FPGAs (Field Programmable Gate Arrays), an integrated programmable circuit that allows for configuration at any time by simply changing the source code; this method is known as DPP (Digital Pulse Processing). The two primary parts of the new digitizers are the ADC (Analog-to-Digital Converter) stage and the FPGA [54, 55].

Analog-to-Digital Converter (ADC)

The analog-to-digital conversion is carried out constantly in the waveform digitizer, and when a trigger event exceeds the threshold, a specified number of samples are kept in the buffer's memory. Two overlapping windows will be created and two different events will be stored in the buffers if a trigger happens while some acquired samples are being saved from another event. High counting rates may be measured using this, and unlike standard digitizers, there is no dead time or lost events [55].

Field Programmable Gate Arrays (FPGA)

The timestand, the baseline, the total (Q_{long}), and he partial (Q_{short}) integrations charges are the outputs of the algorithm performed through FPGA for each triggered event. A level of input at which there is no noise is represented by the baseline. The baseline is subtracted from the integration before the events are stored in the buffer. The integration is the total of the samples found within the integration window. Adjustable parameters include the pre-gate, which affects trigger position, and the integration window (Gate width); a pulse with these parameters is shown in Fig. 5.6. PSD can determine the discrimination parameters using the values of the integrations. Since the pulse tail of a fast neutron is thicker than the tail of a gamma ray, the PSD parameter for a fast neutron is larger than a γ-ray, with the fast neutron [54, 55].

$$PSD = \frac{Q_{long} - Q_{short}}{Q_{long}} = \frac{Q_{tail}}{Q_{total}} \tag{5.1}$$

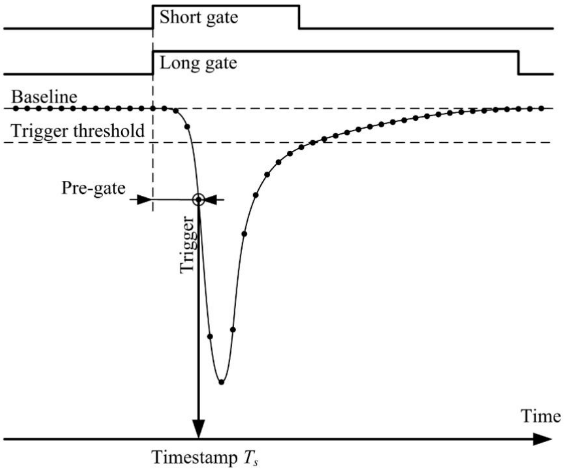

Figure 5.6: Illustration of the acquisition parameters on a digitized pulse [39]
.

5.3 Radioactive sources

Various radioactive sources were employed to characterize the detectors. Gamma-neutron sources were used to optimize the discrimination capabilities, whereas, gamma sources were used for energy calibration. The information about the sources used for laboratory tests are shown in table 5.2. In the process of neutron emission with ^{252}Cf source, the nucleus undergoes two types of decays, i.e., alpha decay (96.91%) and spontaneous fission (3.09%), through the spontaneous fission several photons and neutrons are emitted. The neutrons emitted are fast neutrons with energies in few MeV, and the energy spectrum follows the following distribution [4]:

$$\frac{dN}{dE} = \sqrt{E}.e^{E/t} \tag{5.2}$$

For the spontaneous fission of ^{252}Cf, the constant t has a value of 1.3 MeV.

Table 5.2: Information of the radioactive sources used

S.No	**Source**	**Activity (kBq)**	**Date**	**Emission**
1	^{60}Co	383	01/06/2015	gamma
2	^{22}Na	384	01/06/2015	gamma
3	^{137}Cs	386	01/06/2015	gamma
4	^{252}Cf	2000	03/12/2014	neutron-gamma

5.4 Data Acquisition System - ABCD

The system used to get the data for this work was made for the C-BORD project. It is a newly designed distributed system with the capability of carrying out online analysis and for obtaining digitalized data. The results of an ADC are read by a DAQ, which also provides the ability to adjust high voltage, power supply, temperature, and a variety of other variables. In most cases, data acquisition (DAQ) software is installed on a single computer and is constrained by the hardware of that computer. This new DAQ model is equipped with a system that partitions all of the processes so that they may be executed on separate computers. In this manner, there is no load on the computing system. The processes are referred to as "servers," and they are able to operate on their own. This system has a lot of flexibility, as different tasks can be activated, deactivated, or altered without the need to turn off the whole system. Through the use of network socket, communication may be established between processes. Each process works for a certain task, such as:

- abcd: server for communicating with the CAEN digitizer.
- HIVO: where the high voltage can be regulated.
- lmno: send the impulses to the graphic interface
- EFG: graphic interface, which is in a web server
- spec: module that is in charge of doing 2D-PSD plots, etc.

Different servers can be used to read the data from the different digitizers at the same time. In this work in particular, the two digitizers (CAEN DT5725) each have their own servers, which are hosted on the same machine. The HV power supply server is hosted on another computer. The CAEN digitizer communicates signals through the ABCD server. By changing the parameters in the server (Q_{long}, Q_{short}, *pregate* and *pretrigger*), it is possible to get access to the charge integration of the pulses or the waveform of each pulse.

---

[3] Effective Container Inspection at BORDer Control Points

Chapter 6
Geant4 Simulation

In this chapter, we talked about simulation process for the experiment, performed in laboratory with the purpose to complement the experimental results and simulate the laser-driven fusion neutron sources.

6.1 Introduction

Geant4 is a computer method that focuses on making repeated random samples in order to solve a problem that entails a probability distribution. In order to obtain the expected result, it requires a significant number of iterations of the calculation. The Monte Carlo simulation is used extensively in a wide variety of sectors, including research, the supply chain, engineering, and finance, amongst others. The conventional approach to solving the issue is not very effective, however the system with a high degree of degree of freedom is quite useful.

The Monte Carlo method has been found to be the best way to simulate the radiation movements through matter. Random steps are used to replicate the particle's history, these steps are interrupted by the particle's interaction with matter, which results in a change in the particle's direction and energy loss. Finally, secondary particles are created. The photoelectric effect, Compton effect, and pair production are the main interaction mechanisms involved in it. The cross-section predicts the probability of each of these interaction mechanisms. Therefore, every interaction process and every type of particle involved in the interaction must be accurately modeled in the simulation.

The Geant4 simulation method is easy to use with systems that have complex geometries and different kinds of materials. This allows us to make a simulation that looks like the real experimental system. Assembling a radiation configuration entails identifying the radiation source, the irradiated sample, the detecting devices, and the procedures involved.

In general, different simulation codes have been developed and are available to users working in different fields. The most popular of them are in the field of particle and nuclear physics: [58].

- MCNP and MCNPX: MCNP is a general Monte Carlo N-Particle Transport Code that was developed at the Los Alamos National Laboratory (LANL). Later, LANL developed MCNPX, which is an extended version of MCNP.
- Geant4 is a set of tools made by the Geant4 collaboration for simulating particles movement through matter.
- FLUKA is a general-purpose tool for calculating particles movements and interaction with matter. It was created by European Organization for Nuclear Research (CERN) and National Institute for Nuclear Physics (INFN).

- PENELOPE is a Monte Carlo code for photons and electrons movement together over a large range of energies, from a few hundred eV to about 1 GeV.
- BEAMnrc Monte Carlo code was developed at NRC that is used to model radiotherapy sources.

6.1.1 Geant4

Geometry and Tracking version 4 (Geant4) is a set of tools that can be used to simulate how particles move through matter. In contrast to the other Monte Carlo programs, Geant4 is not a software that can be run on a computer. As an alternative, it is a collection of C++ class libraries that include preset C++ classes. In order to run a simulation using Geant4, users need to create their own code in C++, which must then be compiled into an executable file. The development of a computer software that can replicate a detector while also catering to the requirements of high-energy physics experiments was the objective of the Geant4 project. Geant4 has evolved into a very effective Monte Carlo tool because to the contributions of both physicists and software developers. Its capabilities now extend well beyond those for which it was first designed. Geant4 is currently widely used in a variety of domains, including the following:

- Space science and astrophysics
- Medical physics, nuclear medicine
- Radiation protection
- Accelerator physics
- Detector design
- Food irradiation
- Security, etc

A large group of researchers from Europe, Japan, Canada, and the United States are working together to improve the code and add to its capabilities. Geant4 is getting better and being used by more and more people. Geant4 is written in C++ and uses object-oriented technology to build its whole code system. Fig. 6.1 shows the Geant4 class tree. Each class is responsible for a different task, such as building geometry, defining sources, registering physics processes, keeping track of particles, and so on. Through internal interfaces, different classes can talk to each other.

6.1.2 Construction of Simulation In G4VUser Class

In order to perform a simulation with Geant4-style C++ codes, which include a main function and sub-classes of three important interface classes, G4VUserDetectorConstruction, G4VUserPhysicsList, G4VUserStepping Action, and G4VUserPrimaryGeneratorAction, have to be reimplemented.

G4VUserDetectorConstruction

Detector construction was performed in G4VUserDetectorConstruction class. The class defines the problem geometry, material, position, magnetic field and so on. Here physical and logical volumes are defined used to be defined. The physical volume describes located inside the logic volume. G4VSolid is used to define the shapes and sizes of the objects (such as G4Box and G4Tubs), G4LogicalVolume is used to construct the logical volumes, which is also where the material, attributes, and sensitivity of the detector are specified, and finally, G4VPhysicalVolume is used to construct the physical volumes, which is where the volume is actually placed and parameterized. A logic volume is a representation of an element that has a position, composition, and the ability to retain many volumes inside its own

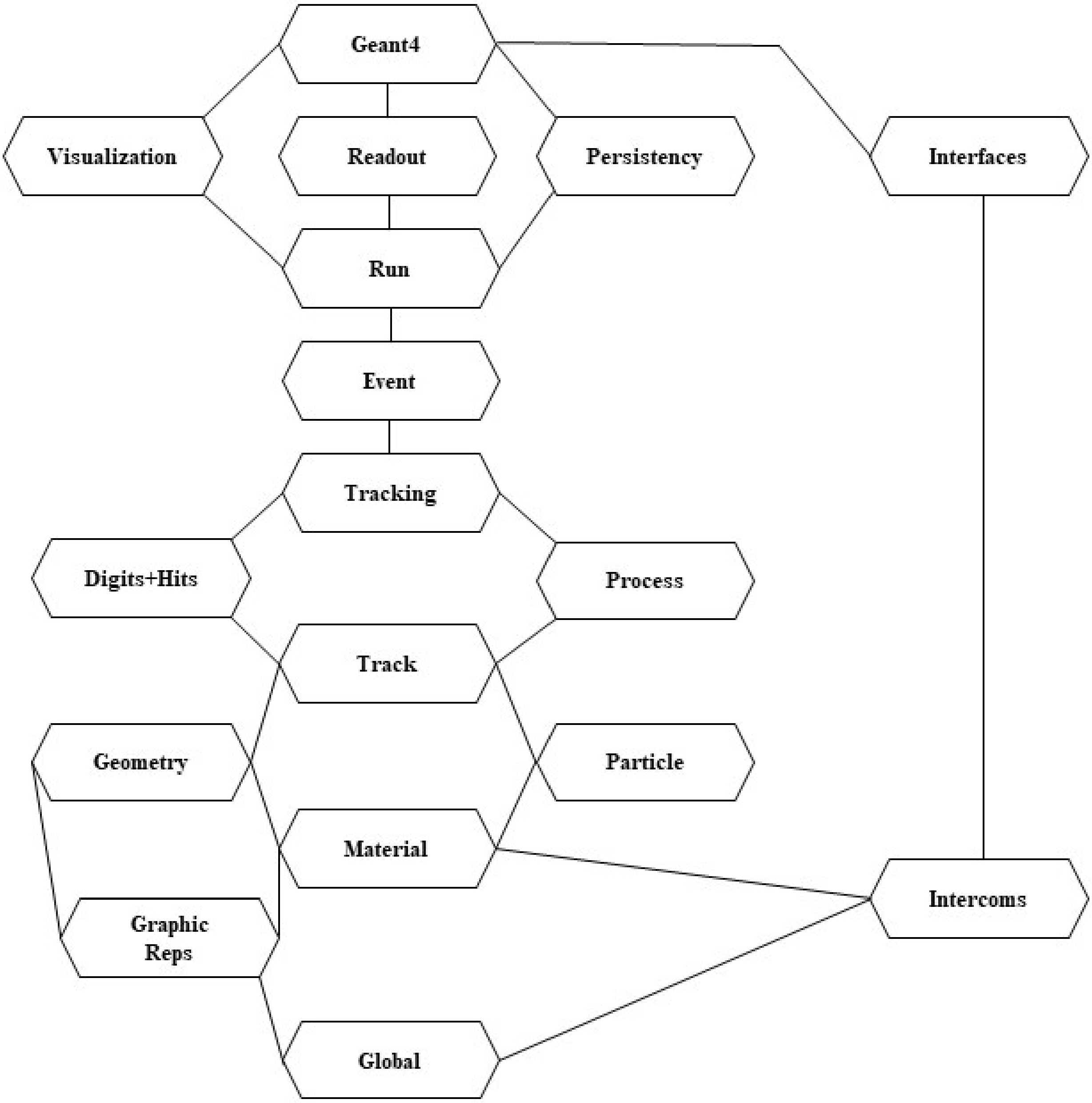

Figure 6.1: Geant4 class categories (Geant4 Collaboration, 2011).

boundaries. In this work, first we build world volume with air having a size of 100 × 100 cm^2, then the graphite, nitrogen, and water materials were build with a square shape with a dimensions 10 × 10 × 10 cm^3. Finally, the mesh box was constructed surrounding the material with a size of diameter of 10 × 10 × 10 cm^3. The composition of the detector was described by the density and its elemental concentration. NaI detector was constructed with dimenisons of 25 × 12.5 × 12.5 cm^3.

G4VUserPrimaryGeneratorAction

The G4VUserPrimaryGeneratorAction class generates source particles with the specified energy, type, direction, position, and weights, among other parameters. The primary particles are created using the G4VuserPrimaryGeneratorAction class; based on the features of the primary particles, a corresponding class must be invoked. The setup of the G4GeneralParticleSource (GPS) class is done in macro where an isotropic source may be configured; the position of the source was set in front of one of the detector's faces. Depending on the source of interest, the number of events, energy, and types of particles may be specified. For instance, we used neutron beam.

G4VUserPhysicsList

The G4VUserPhysicsList class registers all particle types and physics processes that are relevant to the problem and gives each process cross-section data and a model; In the G4UserPhysicsList class, the particles and how they interact were defined. In this class, two different libraries were used to simulate photons and neutrons: G4EmLivermorePhysics and G4HadronPhysicsQGSP BIC HP. For gamma, the G4EmLivermorePhysics library had the photoelectric effect, the Compton scattering, the Rayleigh scattering, and the pair production. The G4HadronPhysicsQGSP_BIC_HP library is set up for neutron collisions that are elastic, inelastic, neutron capture, and fission.

G4VUserStepping Action

Employing additional classes is a viable option for acquiring the required knowledge. The G4UserSteppingAction class is responsible for recording the events that occur in each step, while the G4UserTrackingAction class is responsible for recording the positions of the particles at a certain moment and storing this information. With these two classes, it is possible to get information about how much energy each particle in the detector has left behind. With the G4UserEventAction and G4UserRunAction classes, it is then possible to reconstruct the energy spectrum.

In the main function, a G4RungManager class instance is defined. Classes that are required to run must register with the G4RunManager class. This class starts a simulation, initializes all classes, sets conditions for calculations, and starts the simulation. When the source code is ready, the user needs to compile it. This is usually done with a make file in the Geant4 style, which can be found in the Geant4 package's examples. If the compilation goes well, an executable file will be made. With the help of Geant4 libraries, the executable program can run on UNIX-like systems or on a Windows system with a Cygwin Linux-like environment.

Geant4 has a system for visualizing information. This system is based on graphic libraries like OpenGL and QL. In a 2D or 3D view, the system let us to see geometries, particle paths, and volume overlap errors. To make the visualization, the main function can use classes that are based on relevant interface classes.

To use Geant4, a user needs to know not only enough about physics, but also enough about C++ to make a simulation. Physics processes should be added by hand through C++ programming based on Geant4. So, the user should know all the processes that should be included. Processes, Cross section data, and physics models can be put together in different ways to solve different problems. Through integrated interfaces, people can get to the information they want based on their needs.

Geant4 is built with required classes, doesn't give the standard information that a simulation produces. All information of interest should be manually extracted. If a detector class is given in Geant4, "sensitive" can be set for volumes. User-defined detectors can be used. Most of the time, standard information can be gotten from predefined detector classes such as number of particles passing a surface, total energy deposition in a cell, etc. The following classes and functions can be used to find out more or get data in a different way:

G4UserRunAction

- At the start of a run, the BeginofRunAction method is used.
- At the end of a run, the EndofRunAction method is used.
- They may, for example, be used to book or save histograms at the start or end of a run (depending on the number of particles).

G4UserEventAction

- The BeginOfEventAction method is called at the start of particle event.
- At the end of a particle event, the EndOfEventAction method is called.
- For example, one may choose to store information at the start of an event and analyze it at the conclusion of the event.

G4UserStackingAction

- When a new particle track object is placed onto a stack, the ClassifyNewTrack function is used.
- Before invoking the BeginOfRunAction method of the G4UserEventAction class, the PrepareNewEvent function is called at the start of each event.
- They may, for example, be used to specify the priority of a track or to halt its movement.

G4UserTrackingAction

- At the start of each track, PreUserTrackingAction method is used.
- At the end of each track, PostUserTrackingAction method is used.
- For instance, it can be used to decide if a trajectory should be stored.

By using the member of methods interface classes, internal pointers can be used to get almost all simulation information, such as the energy, charge, position, direction, mass of a particle, and other numbers that are important to the problem. Users can make their own tallies and outputs based on the data extracted. Geant4 can also be set up on Windows with a Microsoft Visual C++ compiler and a cygwin environment, on Linux and Mac OS X with a gcc compiler, and on Mac OS X with a gcc compiler. For parallel computing, interfaces are given that are based on the Task Oriented Parallel C/C++ (TOP-C), the Distributed Analysis Environment (DIANE), and MPI. To parallelize a Geant4 application, only a few changes need to be made to the main function. The communications will be taken care of in the background by the interface classes.

6.2 Design of Simulation - Experiment

An experiment was performed with the Geant4 to simulate neutrons interactions with the materials carbon,nitrogen, and water.In this work, version 10.06 of GEANT4 was used. This is a well-known tool that simulates how radiation moves through matter and is written in C++. The code includes all parts of the simulation, such as the geometry of the system, the materials used, the fundamental particles, the creation of primary particles, the tracking of particles through materials, the physics processes, the response of the detector, the creation of event data, and a visualization of the detector and particle paths. In Fig 6.2 we have shown the design of simulated experiment comprised of target sample in front of neutron source, while the large NaI scintillator of size ”25 × 12.5 × 12.5” cm is used to detect the emission of gammas.

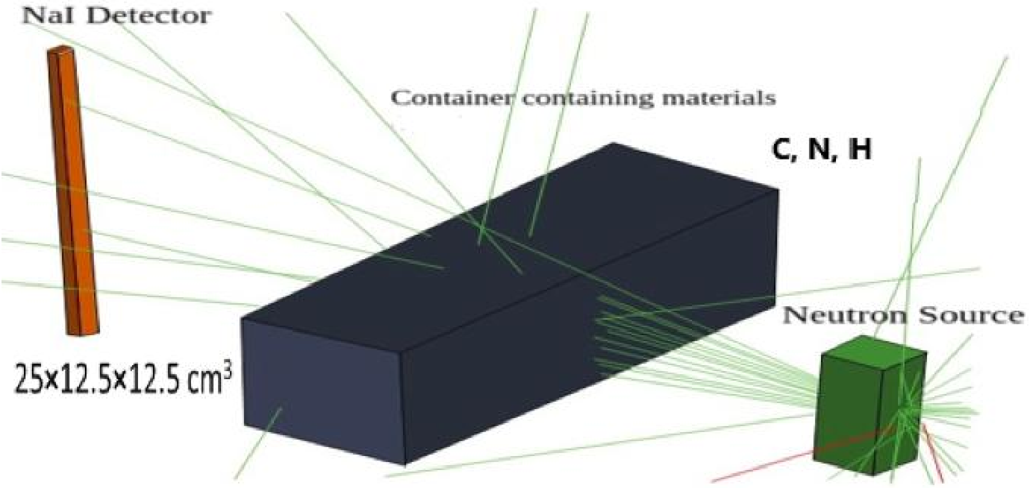

Figure 6.2: Design of experiment using GEANT4

Chapter 7

Results and Discussion

In this chapter, we validate the predictions made from experimental tests with ^{252}Cf neutron source and simulations with fusion neutron sources. In the first step, we compare the experimental results and simulated measurements with ^{252}Cf radiological neutron source up to 10 MeV. In the second step, a simulation was performed with a fusion neutron sources. ^{252}Cf source emits high energy correlated gammas and neutrons which is useful as an interrogating source. They cannot be shut off, which is a serious issue since neutrons are always being emitted from this source. This restricts their applicability to small experiments, and depends upon constant neutron flux without pulsed emission. Therefore, it may be desirable to switch the interrogating radiation on and off and because they have no intrinsic gamma-neutron correlations, a d-d neutron source is nearly ideal.

7.1 Experimental Tests

This section is dedicated to the dedicated tests performed in a laboratory with EJ-309 LaBr scintillator detectors. The experiments design was focused on the analysis of the response of these detectors to gamma and neutrons radiations from the ^{12}C sample bombarded by ^{252}Cf neutron source. The analysis performed using these detectors includes energy calibration, energy resolution, and optimization of the pulse shape discrimination parameters in order to differentiate between gamma and neutrons.

Californium-252 is the most versatile neutron source yet developed because of its many possible forms and applications. It has been found as a useful neutron source for its many potential uses in chemical analysis, neutron radiography, nondestructive inspection, and neutron flux enhancement [37]. The versatility of ^{252}Cf in our work is illustrated by the neutron transmission for nondestructive inspection techniques that has already been found [38]. The neutron emission rate of ^{252}Cf allows dimensionally small, transportable sources to be fabricated. Neutrons transmission complements X-radiography, it reveals the presence of hydrogenous or low-atomic number materials within high-atomic-number materials by means of gamma emissions [37, 38].

In the laboratory, first, we calibrated our detectors EJ-309 and LaBr with sources mentioned in table 7.1 and 7.2. A calibration analysis and measurements are explained in further sections. Then, with the calibrated detectors and ^{252}Cf we tried to see the gamma emission of characteristic energies from the ^{12}C sample. The design of the experiment is presented in Fig 5.3. Since our ^{252}Cf source was weak its neutrons could not react strong enough that makes a gamma rays emission from ^{12}C, which could be possible by the strong neutron source, for example, Americium - Beryllium (AmBe).

7.1.1 Energy Calibration of EJ-309

To characterize the EJ-309 liquid scintillator, we studied the parameters of gamma energy calibration, energy resolution, and gamma efficiency. In addition, due to the specialized uses of the MULTI-SCAN3D project, tests have been performed in order to see gamma radiation from the graphite sample. Particular attention has been paid to the system's capacity to discriminate between neutrons and gamma rays. The response of gamma rays in organic scintillators is determined by the Compton distribution generated by the recoil electrons, there is no photo-peak that provides a relationship between the channel and the energy of the gamma ray. Thus, the energy of the Compton edge is utilized to calibrate the energy. The Compton edge for each gamma-ray was determined using Eq. 4.11. See in Table 7.1 the Compton edges of the gamma-rays used for the calibration.

Table 7.1: Compton edges and emitted gamma-ray energies of the ^{137}Cs and the ^{22}Na

Source	**Gamma-ray (keV)**	**Compton Edge (keV)**
^{22}Na	511	340.61
^{22}Na	1274.537	1062.71
^{137}Cs	661.657	477.34

The energy calibration of EJ-309 scintillator detector was performed using ^{137}Cs and the ^{22}Na sources. For energy calibration, simple method was used, which consists in assigning the Compton edges energy of each gamma-ray to the channel where the amplitude of the Compton plateau reaches to its maximum intensity. In Fig. 7.1 the spectrum of ^{22}Na is obtained with EJ-309 using the CAEN digitizer DT5725, without energy calibration (counts vs channel) where two Compton edges of the ^{22}Na can be seen, and the two points used for the calibration are indicated. Fig: 7.2 shows the energy calibration curve along with the slope, m, and intercept c values.

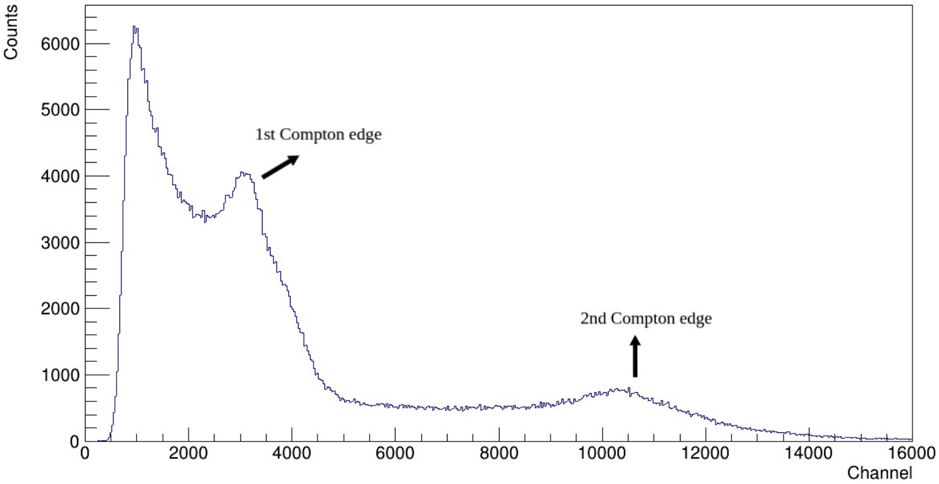

Figure 7.1: Energy spectrum of the 22Na without the energy calibration, using the EJ-309 detector.

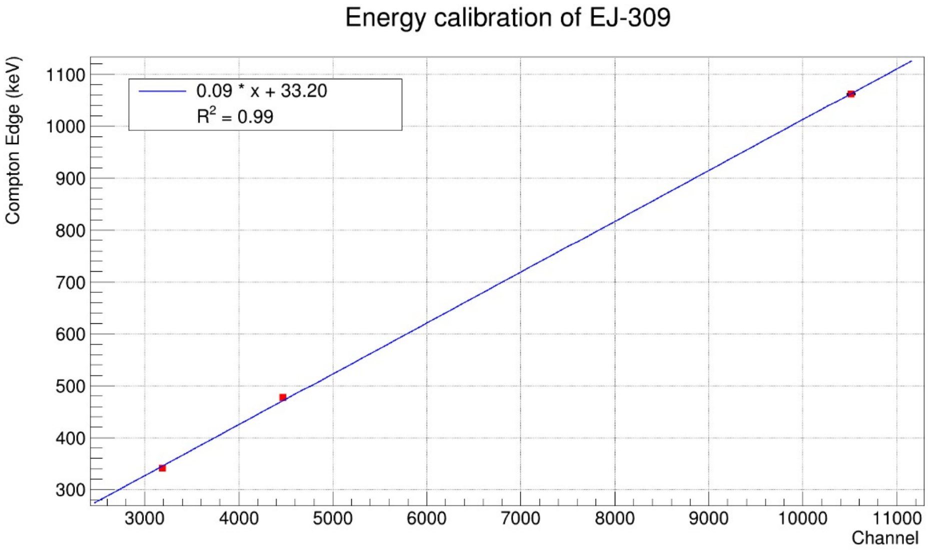

Figure 7.2: Liquid EJ-309 Energy Calibration Curve

7.1.2 Pulse Shape discrimination (PSD) for the best FoM Values

The second step towards the characterization of the scintillator is the optimization of Q_{short} and Q_{long} which are charge integration windows for the optimization of PSD. Then the discrimination parameter can be obtained with the values of the integrations, $PSD = \frac{Q_{long} - Q_{short}}{Q_{long}}$. The optimization consisted of measurement with neutron-gamma source ^{252}Cf for around 15 minutes. The readout was performed using the CAEN DT5725 digitizer. Digitized waveforms were recorded during the measurement, each waveform with an acquisition window of around 4 ns. The optimization of the integration windows consisted in doing an offline analysis as discussed in previous section. The events selected were in the energy range between 0.9 MeVee and 1.4 MeVee as shown in Fig 7.4.

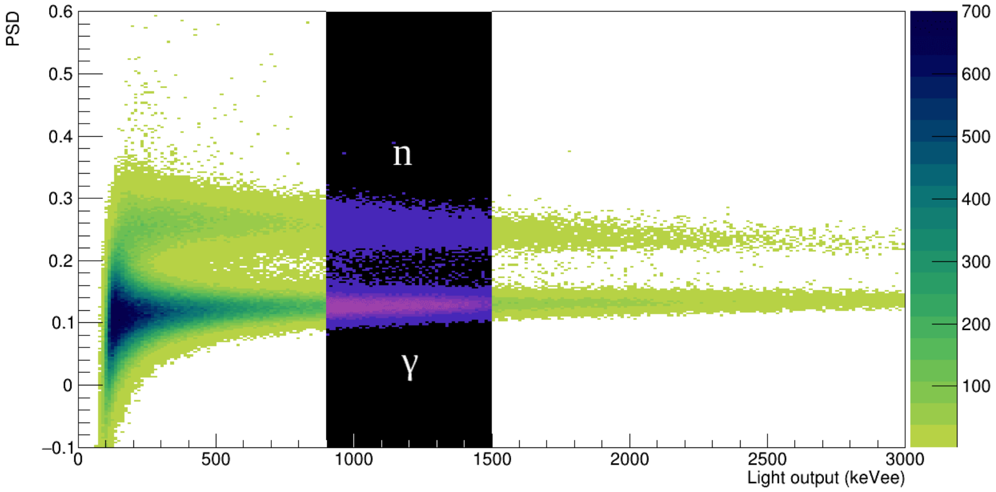

Figure 7.3: 2D PSD plot for gamma and neutrons from ^{252}Cf. The selected range (black strip) corresponds to the Compton tail of ^{22}Na gamma spectrum.

This selection of energy range corresponds to the Compton edge associated with the gamma-ray energy of ^{22}Na at 1274.537 keV. The events in this energy range are plotted as a function of PSD, then the FoM is computed by doing two Gaussian fittings for neutrons and gamma events shown in Fig: 7.4.

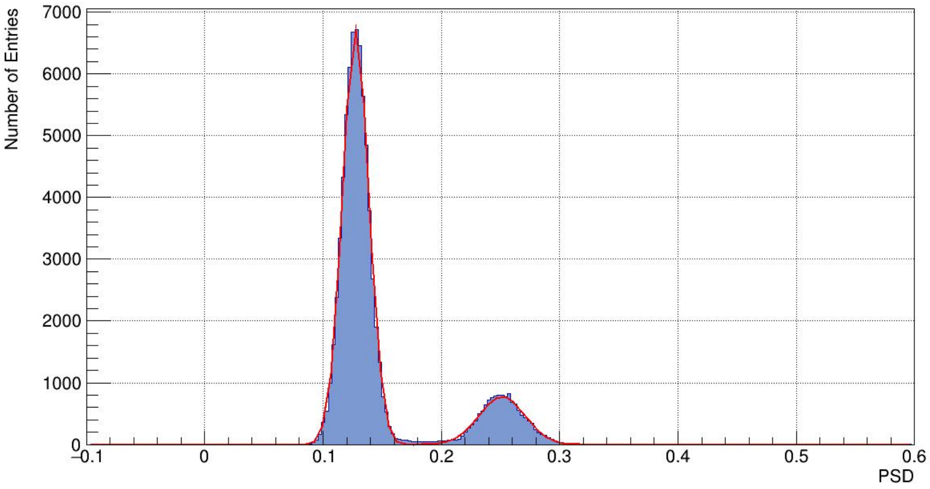

Figure 7.4: Gaussian fittings for neutrons and gamma events.

For the measurements, the pregate and pretrigger were set at 20 ns and 100 ns respectively. The optimized value of the FoM was found to be 1.77. This FoM value is good for the n/γ discrimination. The values for Q_{long} and Q_{short} for the corresponding FoM are 140 ns and 35 ns respectively. The uncertainty in FoM was also calculated.

For 2D PSD plots, In organic liquid scintillators in 2D PSD plots, the upper band corresponds to the neutron spectrum while the lower band corresponds to the γ spectrum shown in Fig 7.3.

7.1.3 Energy Calibration of LaBr

In order to calibrate the LaBr, we employed a novel method based on Compton coincidence technique [35]. This technique can be applied to measure in a wide energy range the position of Compton edge in organic scintillators. The experimental setup comprised an EJ309 liquid organic scintillator which was first tested and calibrated using gamma sources and the LaBr detector. The detectors were placed at distance from source. The gating on events backscattered in the EJ-309 and detected in $LaBr_3$ allowed measuring of photopeak for a given γ-ray energy in LaBr scintillator. Therefore this method provided a valuable tool for the energy calibration of gamma scintillators.

The energy calibration of scintillators used for γ-ray spectroscopy are usually based on the registration of full energy peak after absorption of γ-ray quanta in the detector. Unfortunately, light scintillators (e.g. plastics or liquids) do not show full energy peaks above a certain threshold, as they are not capable to absorb the entire γ-ray energy. This is due to the low density and low atomic number of light material-based scintillators. In table 7.2 the photo peaks of the gamma-rays used for the energy calibration.

Table 7.2: Phtopeaks and gamma-ray energies of the ^{137}Cs, ^{22}Na, and ^{60}Co

Source	**Channel**	**Photopeak (keV)**
^{22}Na	5413.73	511
^{22}Na	13619.1	1274
^{60}Co	12560.5	1173.2
^{60}Co	14311.7	1332.5
^{137}Cs	7036.9	661

This technique is a direct method to measure the photo peak position using in a compton coincidence method. The Lanthanum Bromide (LaBr) detector to register γ-rays backscattered in the tested scintillator (EJ-309), which was placed opposite to the LaBr. The calibration of LaBr was done using γ-rays from ^{60}Co, ^{22}Na and ^{137}Cs sources. Fig: 7.5 shows the energy calibration curve for the LaBr scintillator.

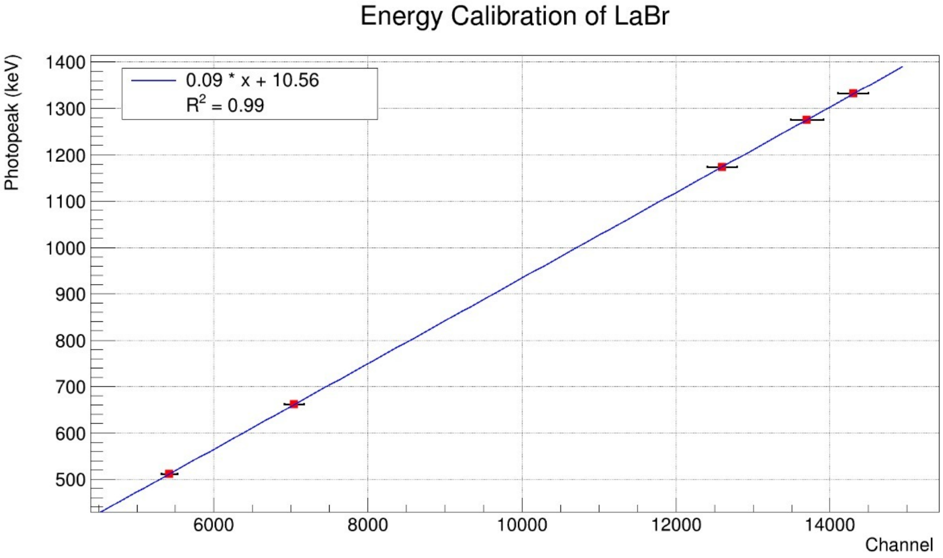

Figure 7.5: LaBr Energy Calibration Curve

7.2 Geant4 Simulation Tests

The simulation method has been discussed in the previous chapter. In the first step, the simulation was performed with a pure ^{252}Cf neutron source with an energy of 10 MeV. In the second step, fusion neutrons were simulated using the target normal sheath acceleration (TNSA) mechanism. It includes monoenergetic and uniform neutrons productions from d-d fusion reactions which can be produced in "Sealed Tube Neutron Generators" with a source strength of 10^8 n/s, as discussed earlier. In the third step, the measurements were also performed from the production of neutrons at ultra-high intensities using exponential laser-based acceleration mechanisms which are referred to as femtosecond lasers, and are, therefore, known to be a prerequisite for the development of compact and portable laser-driven neutron sources, reported in [16]. Femtosecond lasers can also be achieved by exploiting target normal sheath acceleration (TNSA) with thin film targets. For this purpose, we studied neutrons creation from two nuclear reactions, $^7_3$Li(d,n)$^8_4$Be reaction (d-Li), and $^7_3$Li(p,n)$^7_4$Be reaction (p-Li), reported in [16]. NaI detector was used for the detection of γ production and the input neutron flux. The target materials were made composed of carbon, water, and liquid nitrogen. These elements are the most useful markers of the elemental composition of material content shown in table 7.3. The ratio of abundance of HCNO in the samples helps in identification process, as our environment contains many of these organic nuclei. All these organic elements resonate at their characteristic frequency, but H has the tendency to absorbs neutrons than other elements [60]. It is difficult to utilize signal strength due to the stochastic nature of gamma emission, the fluctuation of gamma attenuation with distance and time on target, and the presence of organic clutter (in food, fertilizer, dirt roads, etc.). The ratio of signal intensities from organic components has a major influence on the reliability of distinguishing one explosive substance from another. The large nitrogen content in explosives becomes obvious when the elemental ratios are separated out in a three-dimensional (3-D) space map. Design of the simulated experiment is presented in Fig. 6.2.

Elemental composition of explosives, drugs and illicit materials								
S.No	Materials	C	H	N	O	Cl	N/H	N/C
1	TNT	37	2.2	18.5	42.3	0	8	1
2	Water	0	11.1	0	88.9	0	0	0
3	PETN	19	2.4	17.7	60.8	0	7	1
4	Heroin	68.2	6.3	3.8	21.7	0	0.04	4.2
5	RDX	21.9	3.6	34.4	40.1	0	10	2
6	Cocaine	67.3	6.9	4.6	21.1	0	0.05	4.2

Table 7.3: Elemental composition of drugs and selected materials [38,61].

7.2.1 ^{252}Cf Neutron Source

We modeled pure element acquisition with the Geant4 computer codes to obtain peak identification in the gamma-ray spectra from target samples. Our observed spectra have inconsistent relative pulse heights, absence of peaks, unattended peaks, or even no gamma-ray production data at specific energies is evidence that a complete numerical calibration of the system is not possible. However, We performed dedicated measurements to allow a quantitative simulation shown in Fig. 7.7. The calculated γ-spectra are represented from a qualitative point of view because only the spectrum shape is of interest in order to classify organic goods in special materials, explosives, or narcotics mentioned in table 7.3. A quite satisfactory agreement in net spectra of γ-ray production results from a 10 MeV radioisotopic neutron source interactions with ^{1}H, ^{12}C, and ^{14}N. The spectrum of neutron source is shown in Fig: 7.6, when a neutron enters the target material and enters the NaI scintillator placed in front of a target material, while a gamma Compton scatters off an electron. The scattered particles excite the surrounding nucleus and create an emission of light and transformed it into an electric signal. The gamma rays spectra showed several gamma lines of energy varying from 1 to 4.5 MeV.

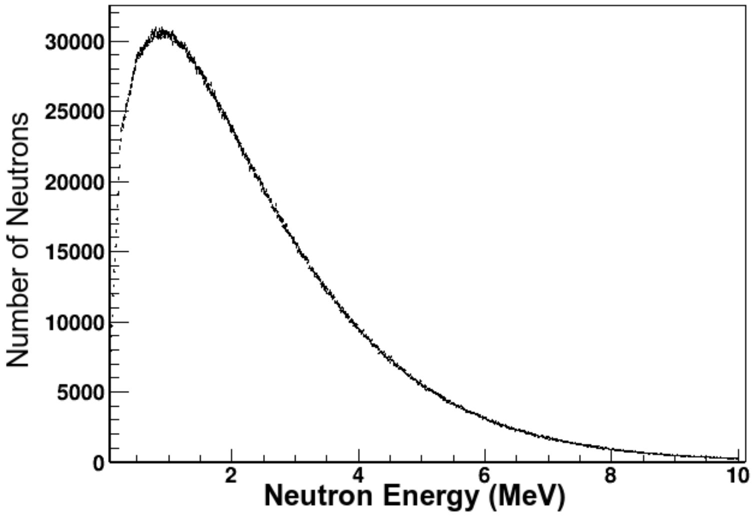

Figure 7.6: Simulated neutron spectra from ^{252}Cf up to 10 MeV.

Characterizing the gamma peaks is crucial for determining the optimal operating conditions. In this manner, a lot of gamma photons are needed to produce the same amount of light as a single neutron, which varies from 10^3 for 0.6 MeV gamma rays to 10^1 for 1 MeV gamma rays. In particular, at spallation sources or reactor facilities, gamma rays are primarily produced by radiative neutron capture and activation. The peak at 0.511 MeV may be due to electron-positron annihilation following pair production. The process can occur when gammas with energies above 1.02 MeV are produced in neutron interactions during inelastic neutron scattering. In figure 7.7 (a), gamma rays of 2.1 MeV and 4.4 MeV emitted from a carbon nucleus following the inelastic neutron scattering (>1.02 MeV) from carbon which may be useful in estimating the carbon content in "sinter mix," a mixture of coke, iron, and flux prepared as feed for blast furnaces in the steelmaking process. From table: 7.4, we know that the nuclear-based explosive materials (i.e., Melamine powder contains high nitrogen content) can also be identified from the presence of elemental components of nitrogen. Therefore, we used ^{14}N (liquid nitrogen) having a density of 0.808 g/cm^3 for detecting prompt gamma-ray spectra following thermal neutron capture reaction. However, the study of γ-radiation resulting from neutron bombardment of ^{14}N is quite complicated using a NaI scintillation detector, since several states of ^{14}N in the fast neutron N^{14}(n,n')N^{14^*} reaction may results in excitation to higher states. The excited states of ^{14}N are shown in table. 7.4. All these states decay either directly to the ground state or through cascades with γ-emission. From the information given in table, the energies of the gamma radiations are to be expected at any given neutron energy.

^{14}N	
S.No	Energy of states (MeV)
1	Ground state
2	2.31
3	3.95
4	4.91
5	5.10
6	5.68
7	5.83
8	6.23
8	6.44

Table 7.4: States of ^{14}N.

The net gamma-ray spectra for the ^{14}N interrogated by ^{252}Cf neutrons are shown in figure 7.7 (b). Gamma rays were detected using a NaI scintillator of energies from 0.511 to 3 MeV. The γ-peaks with energies of 1.64, 2.14, 2.34 MeV were observed, in which approximately half of the production of γ-radiation is from the reaction with neutrons. For γ-radiations above 2 MeV, the first and second annihilation radiation escape peaks are present. The 1.64 MeV γ-radiation results from a cascade transition from the 3 MeV level of ^{14}N to the 2.31 MeV level. The results were simulated with the same Geant4 codes. The theoretical calculations and experimental measurements presented in M.N. Nasrabadi et al. indicate that this method can be used for the detection of explosives and illicit drugs.

In figure 7.7 (c), the net gamma-ray spectra for the ^{1}H have been presented using a water sample. Among all the organic elements H absorbs neutrons to a much larger extent than the other elements. The displayed spectra show the gamma line of 2.23 MeV emitted from ^{1}H. The γ peaks ranging from 0.511 MeV and 0.860 MeV in all spectra might also result from the fast neutrons that lose energy primarily by elastic scattering while slow and thermal neutrons have a high probability of being captured. The two neutron capture reactions ^{1}H(n,γ)^{2}H and ^{14}N(n,p)^{14}C followed inelastic scattering from a nucleus that may result in decay of unstable nucleus and releases a gamma energy of 0.90 MeV, which is deposited by the proton and recoil carbon nucleus in the immediate vicinity of the capture site.

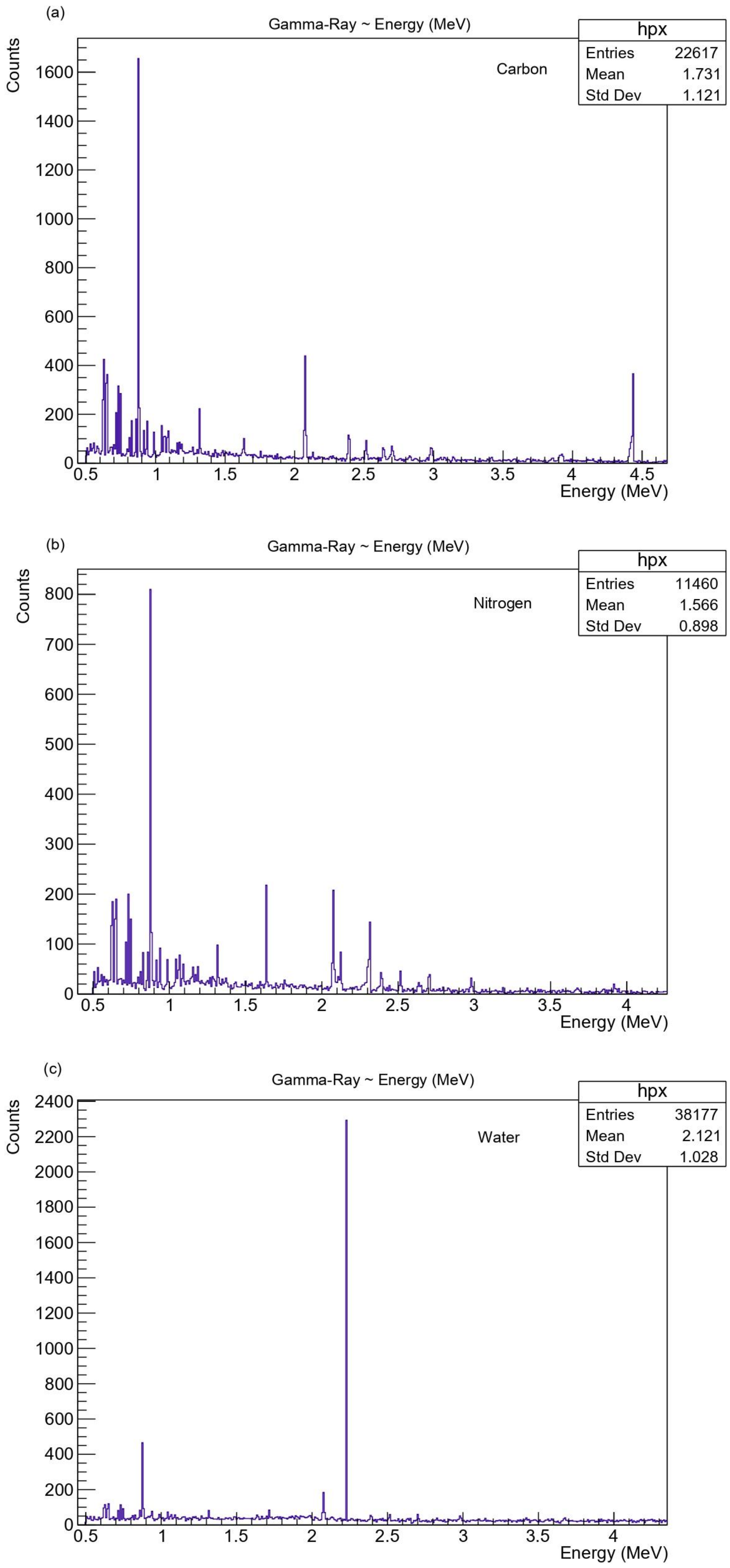

Figure 7.7: Net gamma-ray signatures obtained with NAI detector for C, N, O, H elements acquired with the MCNP simulations performed with the ^{252}Cf neutron source of 10 MeV.

7.3 Fusion-based Neutron Sources

A fusion-based neutron source offers several advantages over the ^{252}Cf neutron source in terms of safety concerns. A D-D/D-T neutron generator produces no radioactivity when the neutron generator is not in operation. Using an accelerator-based neutron source of 2.5 MeV neutron is approximately equal to that of ^{252}Cf spontaneous fission neutrons. The model of the TNSA based fusion neutron production system is shown in Fig. 3.5.

7.3.1 Mono-Energetic Fusion Neutron

Neutron irradiation of bulk materials is of particular interest through the DD neutron generator. When a high-intensity laser interacts with dense materials, it forms a non-equilibrium plasma with high temperature and density that may cause ion acceleration at energies beyond 1 MeV per charge state via a TNSA process, discussed in the previous section. At the Prague Asterix Laser System (PALS) laboratory, a laser pulse of 300 ps duration, 1315 nm wavelength, and 10^{16} W/cm^2 intensity [62], was used to accelerate deuterons using TNSA approaches to irradiate the deuterated targets. By simulating the DD fusion reaction in LISE++ simulation we obtain a maximum of 6.21 MeV of the neutron at the kinetic energy of 3 MeV, resulting in the maximum D-D cross-section [63]. Fig. 7.8 shows plot of D-D nuclear fusion cross-section vs. deuterium energy and comparison of cross sections for the D-T, D-^{3}He, T-T, T-^{3}He, ^{3}He-^{3}He and p-T fusion processes [63]. It shows that DD fusion reaction produces maximum cross-section when deuterons accelerates with projectile energy of 3.0 MeV. The use of bulk or thick materials in the TNSA mechanism generates significant ion acceleration and a hot plasma, which increases the number of fusion events per laser pulse. It can also be confirmed by observing the distinctive neutrons released by the D-D nuclear reaction.

$$D + D \longrightarrow 3He(1.33MeV) + 1n(6.21MeV)K.E = 3MeV \tag{7.1}$$

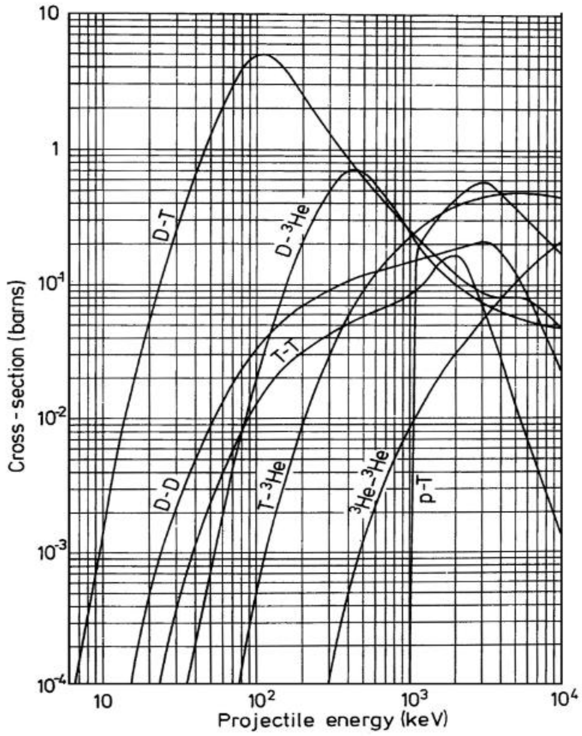

Figure 7.8: D-D nuclear fusion cross-section vs. the deuterium energy and comparison with the cross sections for the D-T, D-^{3}He, T-T, T-^{3}He, ^{3}He-^{3}He and p-T fusion processes.

A typical result obtained during our first experiment for the case of the mono-energetic neutron at 6.21 MeV which is shown in Fig. 7.9, relative to the laser irradiation in fusion accelerator(TNSA) conditions. The energy deposition in terms of γ spectrum detected in NaI scintillator for the same materials interrogated with ^{252}Cf neutron source.

In the gamma energy spectrum for carbon in figure 7.9(a), there is a photopeak at 4.4 MeV due to the photoelectric effect, formed in the case of full absorption of the gamma quanta's energy due to electrons and their Bremsstrahlung detection in the detector. At approximately 4.1 MeV we can see the Compton edge, and using a Compton energy equation [64], the theoretical value of the Compton edge should be around 4.16 MeV, which is in good agreement with the simulated result presented in figure 7.9(a). The region at 0.5 MeV and the Compton edge is the Compton continuum. This region contains the Compton scattering events which give the Compton edge. The peaks at around 3.4 MeV and 3.9 MeV are the double and single escape peaks that might be caused by the pair production. Theoretically, these two peaks should be at 0.511 MeV and 1.02 MeV from the photopeak which is 3.889 MeV and 3.378 MeV [64] which is also in good agreement with the simulated result. The spectrum of figure 7.9(a) also indicates a high yield due to neutrons of about 3.0 MeV kinetic energy, due to the contribution coming from the D-D nuclear fusion reaction in a target, followed by deuteron acceleration contribution. The other peaks at 2.1 2.4, 2.5, and 2.7 MeV results from an inelastic scattering in carbon from the incident energy of the neutrons.

By irradiating high density ^{14}N of 0.81 g/cm^3 under the same conditions we obtain the net gamma spectra, demonstrated in figure 7.9(b). There is a large and clear peak at 2.1 2.31, 2.5, and 2.7 MeV which may result from the inelastic scattering in nitrogen from the incident energy of the fusion neutrons. Finally, the third spectrum of figure 7.9(c) shows a net gamma spectrum from the water sample presents the gamma signatures in ^{1}H from the water sample interrogated by mono-energetic fusion neutron of 6.21 MeV coming from the D-D nuclear reaction production generated at 3.0 MeV of kinetic energy. It can be seen that there is a large peak at around 1.8, 2.09, and 2.23 MeV, which represents gamma rays that may result from the elastic scattering in hydrogen with an incident energy of neutrons. The inset of this spectrum reports that H absorbs neutrons to a lower extent as compared to the radioactive neutron source. The total neutron energy deposited for one neutron shows different elastic scattering events in the NaI detector. The total scintillation light output caused by a neutron interacting with hydrogen produces recoil protons which could be the response function translating the proton energy to scintillation light output.

The time of interaction for gammas and mono-energetic neutrons may show the distribution in time of interactions due to the size of the NaI detector. The particle interaction might be at the beginning or the end of the detector and everything in between, and this causes the time distribution. It is unclear what the origin of the large peak lies, but a possibility is that it is a result of the code that handles the interaction times. This needs to be looked into more. Since the neutron loses energy in its interactions with the material, it will slow down after each interaction. There are also fewer counts at the end of the detector since some neutrons deposit all of their energy into the detector before they reach the end of the detector. Another reason could be the placement of the NaI detector, which is close to the source and that the gamma quanta is much faster than the neutrons. This also makes the distribution in the gamma time of interaction relatively small, which is preferable.

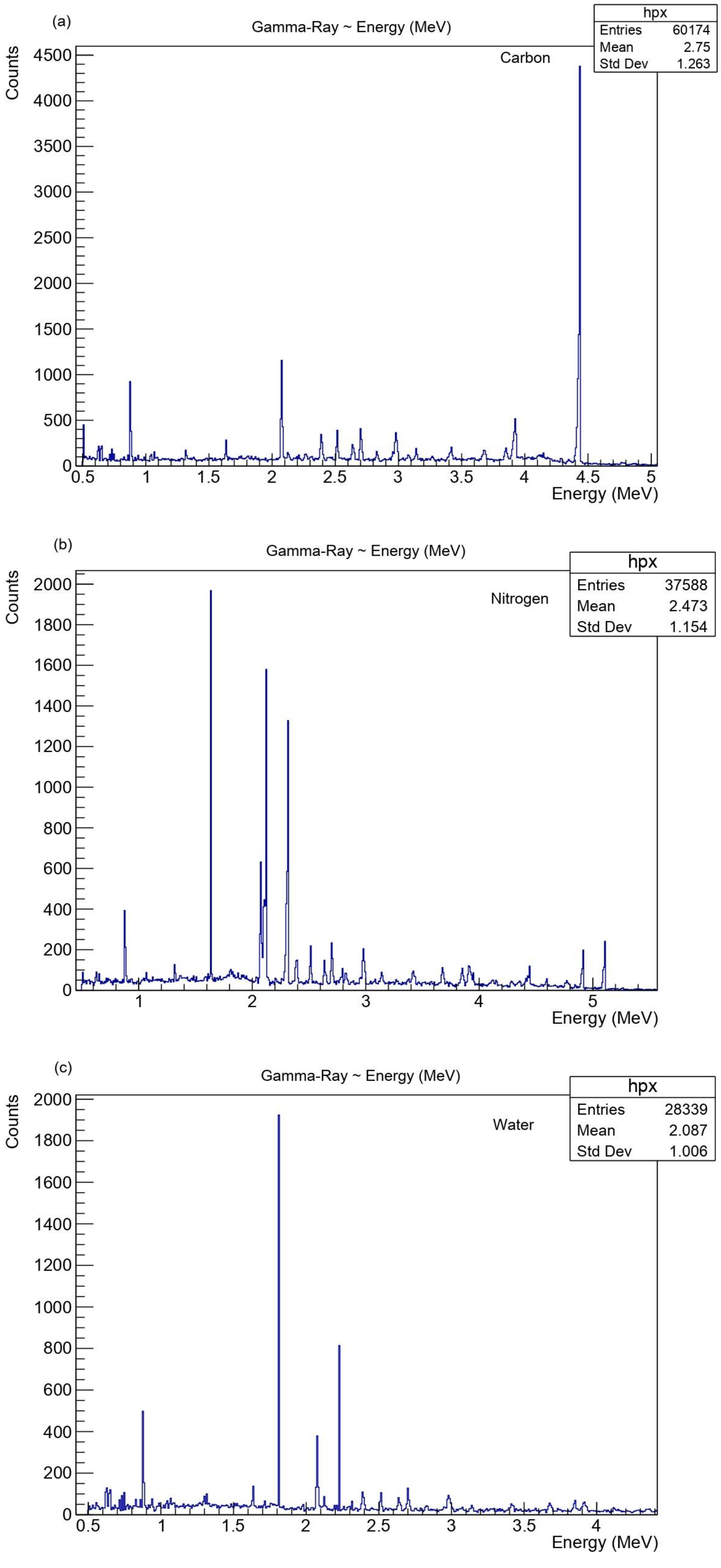

Figure 7.9: Simulated gamma spectra of C, N, H, and O from mono-energetic DD neutron source at 6.21 MeV.

7.3.2 Uniform Neutron Spectrum

The second simulated run was carried out with the uniform distribution of DD neutron source on the same target nuclei with minimum and maximum energy range from 2.45 MeV to 6.21 MeV obtained in the D-D fusion nuclear reaction. Fig. 7.10 reports gamma-ray lines produced in neutron-induced nuclear reactions with the same materials. In figure 7.10(a), The main, prominent gamma line at 4.439 MeV, results from the inelastic neutron scattering off ^{12}C at 4.44 MeV as explained in previous sections. The lines at 0.718 and 1.022 MeV, and 2.0 MeV are of ^{11}C and 2.124 MeV of ^{11}B may produce in various other nuclear reactions. Regarding the 4.439 MeV main gamma line of ^{12}C, one can observe in figure 7.10(a) that our simulated data is in very good agreement with all the previous data sets. Finally, concerning the other gamma lines, no previous experimental values were reported in the literature that could be compared to our data points.

With a uniform distribution of the neutron energy spectrum, we can explain the energies with the most counts in 1.02 MeV and 2.09 MeV of gamma lines which then falls off to 0 at 4 MeV. Since at 4 MeV neutrons can deposit a larger variation of energies, the counts will be more spread out. In other words, the integral of the contribution from the 2 MeV neutrons is close to the same as the integral from the 4 MeV neutrons. The difference between the integrals is caused by the cross-section for the different neutron energies. Also, with the uniform distribution neutron energy spectrum, we can explain the dip in counts at approximately 2.1 MeV and 2.9 MeV. These dips might be explained by the elastic scattering for carbon. Looking at 2.1, 2.8 and 2.9 MeV in Figure 7.10(a) the spikes in the carbon cross-section, meaning the probability for the neutrons to react with the carbon in the detector is a lot higher at those energies.

The gamma spectrum for ^{14}N in figure 7.10(b) shows several clear and large peaks at 0.62 Mev 2.31 MeV, 3.95 MeV energy range results from the inelastic scattering in nitrogen from the minimum and maximum energy range of the incident fusion neutrons. Looking at the spectrum of water which identifies hydrogen in figure 7.10(c) with a maximum count of gamma peak at 2.23 MeV, it decreases with higher energies. The probability for the neutrons to scatter from the hydrogen decreases with the energy which will result in fewer counts for higher energies the energy transferred is not registered by the detector since it has a gamma filter and it will therefore be fewer counts for these energies. The shape of the spectrum is not as clear as for the mono-energetic neutrons. One could expect more counts at the end of the spectrum since the probability for elastic scattering on protons to take place is higher for lower energies. However, the distribution is smaller for higher energies since the higher-energy neutrons travel faster. Using the equation mentioned in [64], we can calculate the number of neutrons for the higher energy, that will be gathered, resulting in more counts at the beginning of the spectrum.

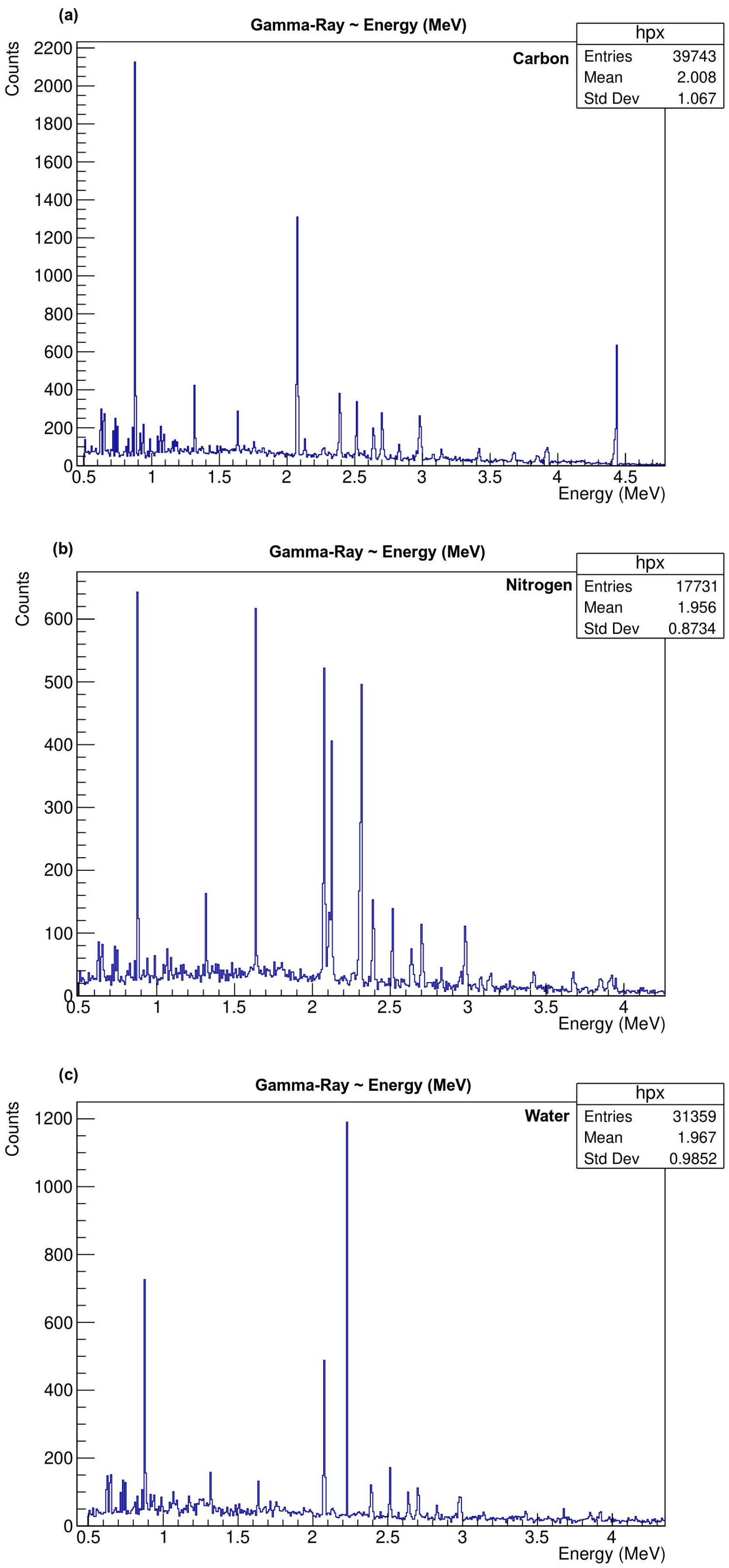

Figure 7.10: Simulated gamma spectra of C, N, H and O from uniform DD neutron spectron source at 2.45 to 6.21 MeV.

7.3.3 Exponential Spectrum

In earlier research [16], high laser energy 10-1000 J experiments were carried out to investigate the neutron production from laser-based acceleration mechanisms using ${}^{2}_{1}$d(d,n)${}^{3}_{2}$He reactions (D-D) in bulk deuterated targets [65–67] as well as pitcher-catcher configurations [16,68] from neutrons produced by ${}^{7}_{3}$Li(p,n)${}^{7}_{4}$Be reactions (p-Li), [16,69,70] and ${}^{7}_{3}$Li(d,n)${}^{8}_{4}$Be reactions (d-Li) [49,71]. Femtosecond lasers, which are known as laser-based acceleration mechanisms for the development of compact and portable laser-driven neutron sources, reported in [16], were used to produce neutrons at extremely high intensities. Femtosecond lasers can also be produced by using thin film targets with TNSA acceleration [72].

TNSA produces energetic electrons that travel through the target but are unable to entirely escape the electric potential caused by charge separation, forming a quasi-static electric sheath field at the interface between the solid target and the vacuum. This sheath field ionizes and accelerates ions from the target's surface, which is mostly made up of hydrogenous impurities. TNSA generates exponential ion spectra, which have been examined for the p-Li and d-Li reactions in a pitcher-catcher configuration despite being created in a sub-picosecond bunch duration. [16]. These techniques were also studied by Willingale et al., [66] and Hou et al. [73] and further developed by Morrison et al. [74] and Maksimchuk, [75].

In this letter, we present the measurements of γ-rays from the study of two nuclear reactions, d-Li, and p-Li, used for neutron production, reported in [16]. We show that using a cryogenically cooled target with a heavy water H_2O, ^{12}C, and ^{14}N produced the high energy γ-rays, in excess of high flux neutrons produced from ${}^{7}_{3}$Li(d,n)${}^{8}_{4}$Be reaction in the energy range of 1 to 15 MeV while and in the range from 1 to 7.75 MeV for ${}^{7}_{3}$Li(p,n)${}^{7}_{4}$Be reactions. NaI detector was used for the detection of γ production and the input neutron flux. The large NaI detector was placed at a distance of 15 m from the targets. The neutron energy spectrum from each reaction was measured before the target. An exponential decaying neutron spectrum, consistent with TNSA acceleration, exhibits maximum detectable neutron energy up to 15 MeV. The spectra are shown in Fig. 7.11. The experimental neutron spectra for these reactions are presented in [16]. Both p-Li and d-Li neutron spectra demonstrate the same exponential shape with the highest flux of 10^7 n/sr.

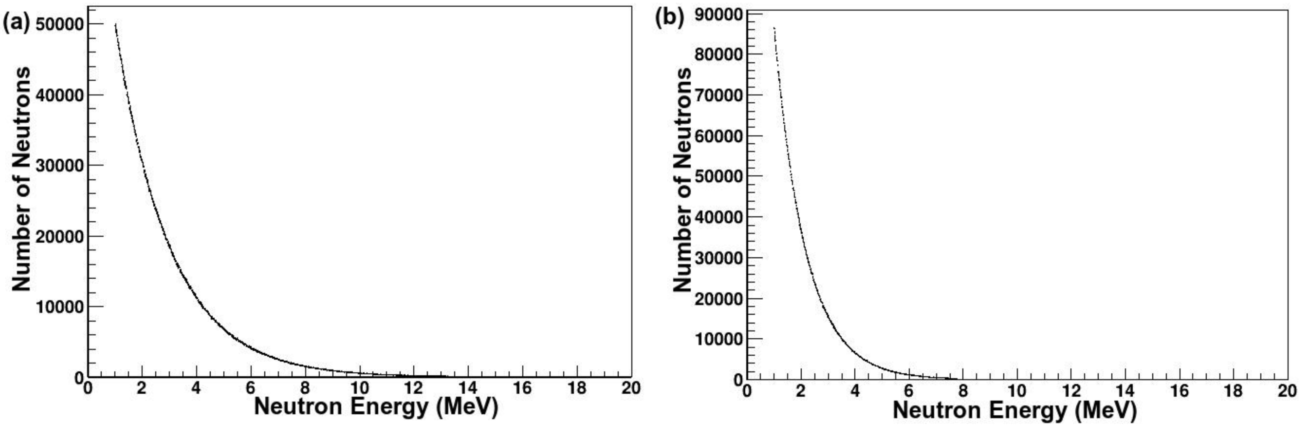

Figure 7.11: Simulated neutron spectra along different targets in the normal direction. (a) The d-Li neutron spectrum shows higher flux and energy. (b)The p-Li neutron spectrum shows the highest energies and total flux. The simulated spectrum was calculated with an exponential scale to match the experimental flux spectra shown in [49]

Numerical simulations were then performed to interrogate γ-rays from a reaction of these neutrons with samples used in earlier tests, This ultra-intense neutron interrogation method was performed to better understand the identification of materials. The simulated results are presented from the production of both neutrons for each sample in Fig. 7.12.

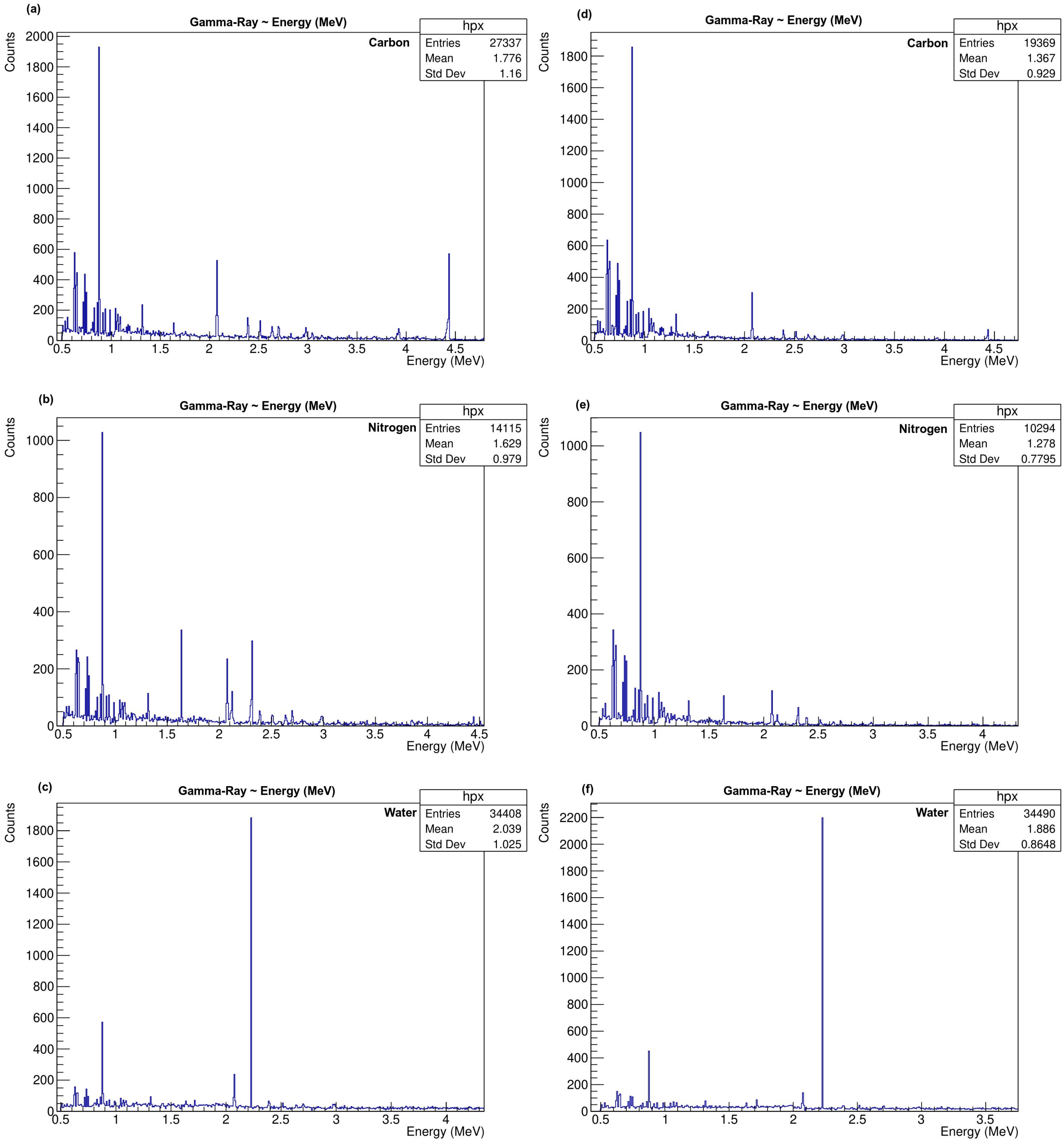

Figure 7.12: Simulated γ-spectra for H_2O, ^{12}C, and ^{14}N are interrogated by the d-Li neutron spectrum and p-Li neutron spectrum. The spectrum (a), (b), and (c) results from d-Li (1-15 MeV) and (d), (e), and (f) from p-Li (1-7.75 MeV) neutrons reactions with these elements.

The modeled element acquisitions with Geant4 identify the gamma-ray spectra and validate the simulation method to our previous measurements obtained from ^{252}Cf radioisotopic neutron source. It can be seen that observed plots (a), (b), and (c) in figure 7.12 have relative pulse heights similar to a spectrum presented in Fig. 7.7. These dedicated measurements for γ-spectra verify our results in a qualitative point of view in order to classify organic goods in special hydrogenous materials and explosives presented in table 7.3, from fast and thermal neutron interactions with these elements. The spectra displayed in this figure are emitted when the objects were interrogated up to 15 MeV neutrons emitted from the d-Li fusion reaction. In these spectra, the 10^3 number of photons emitted at 0.511 MeV to 10^1 for 1 MeV of energy. In particular, these gamma rays are primarily produced due to electron-positron annihilation following pair production. rays of 2.1 MeV and 4.4 MeV emitted from a carbon nucleus following the inelastic neutron scattering ($>$1.02 MeV) from carbon which could be the signature in estimating the carbon content in different materials given in table 7.3. The net gamma spectra for the presence of nitrogen content is shown in the spectrum (b) in Fig. 7.12, follows the thermal neutron capture reaction in which states of ^{14}N may be excited to higher states and decay either directly to the ground state or through cascades with γ-emission at energies of 1.64, 2.14, 2.32 MeV. Figure 7.12 (c), shows the net gamma-ray spectra for the presence of ^{1}H content interrogated by d-Li neutrons. The displayed spectra emit the gamma line of 2.23 MeV emitted from ^{1}H.

The gamma spectra presented in Fig. 7.12 (d), (e), and (f) do not validate the simulation results in view of other measurements. The p-Li neutron spectra are consistent with the p-Li proton flux due to the initial proton energy and have been measured experimentally in earlier work [16]. The neutron production from the p-Li reaction in TNSA acceleration shows an exponential spectrum with a negative Q value of -1.64 MeV which downshifts the neutron spectra in a pitcher-catcher configuration. Therefore, the observed peaks for these elements have the absence of peaks and even no gamma-ray production data at energies of 4.4 MeV in carbon at 2.34 MeV in nitrogen and no gamma at the energy of 3.95 MeV. The calculated γ-spectra for water from ^{1}H represents a qualitative point of view that better verifies the spectrum shape for hydrogen content to classify organic goods in special materials, explosives, or narcotics in the plot (f) of Fig: 7.12.

Chapter 8
Conclusion

In this thesis, we studied the laser plasma based acceleration technologies for neutrons production within the framework of the MULTISCAN3D project. The laser-driven neutron sources for the elemental characterization of materials has been obtained from these nuclear reactions i.e., ${}^{2}_{1}$d(d,n)${}^{3}_{2}$He, ${}^{7}_{3}$Li(p,n)${}^{7}_{4}$Be, and ${}^{7}_{3}$Li(d,n)${}^{8}_{4}$Be. These neutron productions mechanisms were studied in a framework of target normal sheath acceleration (TNSA) mechanism in a pitcher-catcher configuration in three different schemes i.e., monoenergetic, uniform neutrons, and exponential neutron spectrum. A proposed TNSA neutron production system is shown schematically in Fig. 3.5. Fusion reaction produces neutron of 2.5 MeV energy which is approximately equal to that of ^{252}Cf spontaneous fission neutron energies. A continuous beam of monoenergetic neutrons can be produced by a sealed tube neutron generator shown in Fig: 3.7, or other small accelerator. In our simulation, we produce monoenergetic neutron of 6.21 MeV by accelerating deuteron at kinetic energy of 3 keV. The uniform neutrons spectrum is obtained in minimum and maximum range of 2.5 MeV and 6.21 MeV. The exponential neutron spectrum is based on a portable femtosecond laser system also known as compact laser systems. Femtosecond lasers can produce neutrons at extremely high intensities and high neutron flux than fusion driven neutron sources.

The simulated neutrons were used to interact with target materials in order to to detect γ signatures from target samples for elemental characterization. For this purpose, we have implemented a simulation code in Geant4 with a detector environment, and later we used it to optimize the geometries and materials of a detector set up for different neutron processes. The detector environment consists of NaI detector to detect γ signatures from target samples containing H,C,N,O. The NaI detector was placed in front of a target sample. When the neutron interacts with the material placed in a box at a distance from the source, it excites the nuclei and emits gamma rays signal of characteristic energies which is observed with NaI detector. The obtained results from the fusion neutron source are in good agreement than compact laser driven neutron source produced in p-Li and d-Li reactions. The p-Li reaction did not validate our other results in view of other measured spectrums due to the high initial proton energy and negative Q value. In contrast, the d-Li reaction has a positive Q value which upshifts the neutron spectra. The p-Li and d-Li reactions produced higher neutron flux than the d-d fusion reaction.

The experimental investigation was performed with radioactive ^{252}Cf neutron source. The experimental tests were based on the characterization of organic liquid EJ-309, and inorganic LaBr scintillation detectors. A calibration analysis and measurements were explained in previous chapter. Then, with the calibrated detectors using a radioisotope of ^{252}Cf source we tried to see gamma emission from ^{12}C sample. Since our ^{252}Cf source was not strong enough to produce neutrons that could react with carbon and this resulted in gamma emission with less counts. This problem can be circumvented using strong neutron source like Americium - Beryllium (AmBe). In order to validate the experiment for future work, we implement a similar simulation code in Geant4 of a detector environment for a ^{252}Cf neutron source with target sample H,C,N,O. The results from the simulation were also in better agreement with the previous work and can therefore be used and can be further expanded. In the continuation of this project, an isotropic Am-Be neutron source can be used in the laboratory with the characterized scintillators in order to validate our interrogation method.

In conclusion, Several methods exist that use neutrons from radioisotopes such as ^{252}Cf or Am-Be. The primary benefit is the low initial cost and long service life of such sources. The detection of illegal substances and explosives has benefited from the use of ^{252}Cf sources. The findings of this study furthermore verify the viability of using neutrons generated by laser facilities for materials identification. Based on the predictions, the ^{252}Cf neutron source generates high-energy correlated gammas and neutrons, making it a useful interrogation source. A major problem of this source is that they are constantly emitting neutrons and they cannot be turned off. This restricts their applicability to small experiments that rely on a constant neutron flux without pulsed emission. Since it might be useful to switch the probing radiation on and off, a laser-driven fusion neutron source is practically suitable since it has no intrinsic gamma-neutron correlations.

Bibliography

[1] Megahid, R. M., Osman, A. M., Kansouh, W. A. (2009, November). Neutron based techniques for the detection of illicit materials and explosives. In IAEA Third Research Co-ordination Meeting, Johannesburg, South Africa (Vol. 9).

[2] Melnikov, Y., Avtonomov, P., Kornienko, V., Olshansky, Y. (2011). Detection of dangerous materials and illicit objects in cargoes and baggage: current tools, existing problems and possible solutions. Journal of homeland security and emergency management, 8(1).

[3] https://nap.nationalacademies.org/read/6469/chapter/4.

[4] Knoll, G. F. (2010). Radiation detection and measurement. John Wiley Sons.

[5] Grodzicka-Kobylka, M., Szczesniak, T., Swiderski, L., Brylew, K., Moszyński, M., Valiente-Dobón, J. J., ... Mianowska, Z. (2021). Comparison of detectors with pulse shape discrimination capability for simultaneous detection of gamma-rays, slow and fast neutrons. Nuclear Instruments and Methods in Physics Research Section A: Accelerators, Spectrometers, Detectors and Associated Equipment, 1019, 165858.

[6] Melnikov, Y., Avtonomov, P., Kornienko, V., Olshansky, Y. (2011). Detection of dangerous materials and illicit objects in cargoes and baggage: current tools, existing problems and possible solutions. Journal of homeland security and emergency management, 8(1).

[7] Alvarez, J., Fernández-Tobias, J., Mima, K., Nakai, S., Kar, S., Kato, Y., Perlado, J. M. (2014). Laser driven neutron sources: characteristics, applications and prospects. Physics Procedia, 60, 29-38.

[8] Esarey, E., Schroeder, C. B. (2003). Physics of laser-driven plasma-based accelerators. LBNL Report, LBNL 53510, 1-39.

[9] Marc Zimmer, "Laser-Driven Neutron Sources - A Compact Approach to Non-Destructive Material Analysis", DOI: 10.25534/tuprints-00012996, https://tuprints.ulb.tu-darmstadt.de/id/eprint/12996.

[10] Zimmer, M. (2020). Laser-Driven Neutron Sources-A Compact Approach to Non-Destructive Material Analysis.

[11] Jiao, X. (2019). Neutron Sources from Laser Plasma Interactions. The University of Texas at Austin.

[12] Chen, F. F. (1984). Introduction to plasma physics and controlled fusion (Vol. 1, pp. 19-51). New York: Plenum press.

[13] Gurnett, D. A., Bhattacharjee, A. (2017). Introduction to plasma physics: With space, laboratory and astrophysical applications. Cambridge University Press.

[14] Alvarez, J., Fernández-Tobias, J., Mima, K., Nakai, S., Kar, S., Kato, Y., Perlado, J. M. (2014). Laser driven neutron sources: characteristics, applications and prospects. Physics Procedia, 60, 29-38.

[15] Alejo, A., Ahmed, H., Green, A., Mirfayzi, S. R., Borghesi, M., Kar, S. (2015). Recent advances in laser-driven neutron sources. Il nuovo cimento C, 38(6), 1-7.

[16] Zulick, C., Dollar, F., Chvykov, V., Davis, J., Kalinchenko, G., Maksimchuk, A., ... Krushelnick, K. (2013). Energetic neutron beams generated from femtosecond laser plasma interactions. Applied Physics Letters, 102(12), 124101.

[17] Hah, J., Nees, J. A., Hammig, M. D., Krushelnick, K., Thomas, A. G. R. (2018). Characterization of a high repetition-rate laser-driven short-pulsed neutron source. Plasma Physics and Controlled Fusion, 60(5), 054011.

[18] Paschotta, Rüdiger (July 1, 2017). “Chirped-pulse Amplification”. RP Photonics Encyclopedia. Retrieved October 2, 2018.

[19] Keppler, S., Sävert, A., Körner, J., Hornung, M., Liebetrau, H., Hein, J., Kaluza, M. C. (2016). The generation of amplified spontaneous emission in high-power CPA laser systems. Laser photonics reviews, 10(2), 264-277.

[20] Hamm, R. (2010). Paper AP/IA-12, IAEA Proceedings Series, STI/PUB/1433, ISBN 978-92-0-150410-4.

[21] M. Roth and M. Schollmeier, Ion Acceleration—Target Normal Sheath Acceleration, Proceedings of the CAS-CERN Accelerator School: Plasma Wake Acceleration, Geneva, Switzerland, 23–29 November 2014, edited by B. Holzer, CERN-2016-001 (CERN, Geneva, 2016).

[22] J.R. Davies, Phys. Rev. E 69(6) (2004) 065401(R). http://dx.doi.org/10.1103/PhysRevE.69.065402.

[23] UM Radiation Facilities (2019). 250 kw triga reactor. https://radiation.umd.edu/facilities/reactor. Accessed: 2019-08-24.

[24] Ludewigt, B. A., Wells, R. P., Reijonen, J. (2007). High-yield D–T neutron generator. Nuclear Instruments and Methods in Physics Research Section B: Beam Interactions with Materials and Atoms, 261(1-2), 830-834.

[25] Litos, M., Adli, E., An, W., Clarke, C. I., Clayton, C. E., Corde, S., ... Yocky, G. (2014). High-efficiency acceleration of an electron beam in a plasma wakefield accelerator. Nature, 515(7525), 92-95.

[26] Jirka, M., Vranic, M., Grismayer, T., Silva, L. O. (2020). Scaling laws for direct laser acceleration in a radiation-reaction dominated regime. New Journal of Physics, 22(8), 083058.

[27] Modena, A., Najmudin, Z., Dangor, A. E., Clayton, C. E., Marsh, K. A., Joshi, C., ... Walsh, F. N. (1995). Electron acceleration from the breaking of relativistic plasma waves. nature, 377(6550), 606-608.

[28] Maksimchuk, A., Reed, S., Naumova, N., Chvykov, V., Hou, B., Kalintchenko, G., ... Yanovsky, V. (2007). Energy scaling of quasi-monoenergetic electron beams from laser wakefields driven by 40-TW ultra-short pulses. Applied Physics B, 89, 201-207.

[29] Maksimchuk, A., Reed, S., Bulanov, S. S., Chvykov, V., Kalintchenko, G., Matsuoka, T., ... Schultz, D. R. (2008). Studies of laser wakefield structures and electron acceleration in underdense plasmas. Physics of Plasmas, 15(5), 056703.

[30] Nelson, R. O., Vogel, S. C., Hunter, J. F., Watkins, E. B., Losko, A. S., Tremsin, A. S., ... Winch, N. M. (2018). Neutron imaging at LANSCE—from cold to ultrafast. Journal of Imaging, 4(2), 45.

[31] Connaster, R. (2019). Overview presentation-connaster r (ess), ess fundamentals.

[32] Mason, T. E., Abernathy, D., Ankner, J., Ekkebus, A., Granroth, G., Hagen, M., ... Wang, X. L. (2005, June). The Spallation Neutron Source: A powerful tool for materials research. In AIP Conference Proceedings (Vol. 773, No. 1, pp. 21-25). American Institute of Physics.

[33] World Nuclear Association (2018). Physics of uranium and nuclear energy. https://www.world-nuclear.org/information-library/nuclear-fuel-cycle/introduction/physics-of-nuclear-energy.aspx. Accessed: 2019-08-22.

[34] Half a century of life of the TRIGA Mark II reactor and of scientific and didactic activity of the Applied Nuclear Energy Laboratory (LENA) of the University of Pavia , on researchgate.net.

[35] IAEA (2009). Physics of uranium and nuclear energy. http://www-naweb.iaea.org/napc/physics/research reactors/database/RR20Data20Base/datasets/report/Italy 20(Italian20Republic)2020Research20Reactor20Details20-20LENA,20TRIGA20II. 20PAVIA.htm. Accessed: 2019-08-22.

[36] Garrett, A. B. (1962). The neutron identified: Sir james chadwick. Journal of Chemical Education, 39(12), 638.

[37] Seaborg, G. T. (1969). sup252 Cf: RADIOISOTOPE WITH A FUTURE (No. CONF-681032-). Atomic Energy Commission, Washington, DC.

[38] Cornman, W. R., Reinig, W. C., Permar, P. H. (1974). Californium-252: a new, promising neutron source (No. DP-MS-73-26; CONF-730641-2). Du Pont de Nemours (EI) and Co., Aiken, SC (United States). Savannah River Lab..

[39] Tsoulfanidis, N., Landsberger, S. (2021). Measurement detection of radiation. CRC press.

[40] Photomultiplier Tubes, Basics and Applications, THIRD EDITION (Edition 3a), Hamamatsu Photonics K.K. (2007).

[41] User S. Home - Eljen Technology [Internet]. Eljentechnology.com. 2021. Available from: https://eljentechnology.com/.

[42] S.V. Budakovsky et al., Mol. Cryst. Liq. Cryst. 385, 71 (2002).

[43] Marques, L., Vale, A., Vaz, P. (2021). State-of-the-art mobile radiation detection systems for different scenarios. Sensors, 21(4), 1051.

[44] Special Nuclear Material [Internet]. NRC Web. 2021 [cited 23 July 2021]. Available from: https://www.nrc.gov/materials/sp-nucmaterials.html.

[45] Liquid Scintillators, Organic Scintillation Materials and Assemblies, saint-gobain crystals.

[46] NaIL Dual Detection Neutron-Gamma Scintillator, Inorganic Scintillation Materials and Assemblies, saint-gobain crystals. https://www.crystals.saint-gobain.com/radiation-detection-scintillators/crystal-scintillators/nail-scintillation-crystals.

[47] Grodzicka-Kobylka, M., Szczesniak, T., Swiderski, L., Brylew, K., Moszyński, M., Valiente-Dobón, J. J., ... Mianowska, Z. (2021). Comparison of detectors with pulse shape discrimination capability for simultaneous detection of gamma-rays, slow and fast neutrons. Nuclear Instruments and Methods in Physics Research Section A: Accelerators, Spectrometers, Detectors and Associated Equipment, 1019, 165858.

[48] Kim, C., Yeom, J. Y., Kim, G. (2019). Digital n- pulse shape discrimination in organic scintillators with a high-speed digitizer. Journal of Radiation Protection and Research, 44(2), 53-63.

[49] Swiderski, L., Moszynski, M., Wolski, D., Batsch, T., Iwanowska, J., Nassalski, A., ... Hurlbut, C. (2010). Further study of boron-10 loaded liquid scintillators for detection of fast and thermal neutrons. IEEE Transactions on Nuclear Science, 57(1), 375-380.

[50] Balmer, M. J., Gamage, K. A., Taylor, G. C. (2015). Comparative analysis of pulse shape discrimination methods in a 6Li loaded plastic scintillator. Nuclear Instruments and Methods in Physics Research Section A: Accelerators, Spectrometers, Detectors and Associated Equipment, 788, 146-153.

[51] Delgado, J. (2021). Design and characterization of the neutron-gamma detection module of the DRAGON project.

[52] User S. Home - Eljen Technology [Internet]. Eljentechnology.com. 2021. Available from: https://eljentechnology.com/.

[53] CAEN - Tools for Discovery [Internet]. CAEN - Tools for Discovery. 2021. Available from: https://www.caen.it/.

[54] Pino F. Development of Innovative Technology for Detection and Identification of Radioactive Materials. PhD Thesis, Univerity of Padova; 2014.

[55] Cester, D., Lunardon, M., Stevanato, L., Viesti, G., Chandra, R., Davatz, G., ... Touramanis, C. (2016). Commissioning and field tests of a van-mounted system for the detection of radioactive sources and special nuclear material. IEEE Transactions on Nuclear Science, 63(2), 1314-1322.

[56] Incident and Trafficking Database (ITDB) — IAEA [Internet]. Iaea.org. 2021. Available from: https://www.iaea.org/resources/databases/itdb.

[57] Fontana, C. L., Carnera, A., Lunardon, M., Pino, F. E., Sada, C., Soramel, F., ... Moretto, S. (2018, July). A distributed data acquisition system for nuclear detectors. In International Journal of Modern Physics: Conference Series (Vol. 48, p. 1860118). World Scientific Publishing Company.

[58] Zhang, G. (2011). Monte Carlo simulation of mixed neutron-gamma radiation fields and dosimetry devices.

[59] Hatchett, S. P., Brown, C. G., Cowan, T. E., Henry, E. A., Johnson, J. S., Key, M. H., ... Yasuike, K. (2000). Electron, photon, and ion beams from the relativistic interaction of Petawatt laser pulses with solid targets. Physics of Plasmas, 7(5), 2076-2082.

[60] Maksimchuk, A., Raymond, A., Yu, F., Petrov, G. M., Dollar, F., Willingale, L., ... Krushelnick, K. (2013). Dominant deuteron acceleration with a high-intensity laser for isotope production and neutron generation. Applied Physics Letters, 102(19), 191117.

[61] Neutron-Activated Gamma-Emission: Technology Review by Marc Litz, Christopher Waits, and Jennifer Mullins, Army Research Laboratory, ARL-TR-5871, January 2012. https://apps.dtic.mil/sti/pdfs/ADA554870.pdf.

[62] http://www.pals.cas.cz/laser-induced-aneutronic-fusion-reaction-by-advanced-materials-2/.

[63] Verbeke, J. M. (2000). Development of high-intensity DD and DT neutron sources and neutron filters for medical and industrial applications.

[64] Sjöberg, J. (2019). Coincidences between neutrons and gammas.

[65] Norreys, P. A., Fews, A. P., Beg, F. N., Bell, A. R., Dangor, A. E., Lee, P., ... Cable, M. D. (1998). Neutron production from picosecond laser irradiation of deuterated targets at intensities of. Plasma physics and controlled fusion, 40(2), 175.

[66] Izumi, N., Sentoku, Y., Habara, H., Takahashi, K., Ohtani, F., Sonomoto, T., ... Yamanaka, T. (2002). Observation of neutron spectrum produced by fast deuterons via ultraintense laser plasma interactions. Physical Review E, 65(3), 036413.

[67] Habara, H., Lancaster, K. L., Karsch, S., Murphy, C. D., Norreys, P. A., Evans, R. G., ... Silva, L. O. (2004). Ion acceleration from the shock front induced by hole boring in ultraintense laser-plasma interactions. Physical Review E, 70(4), 046414.

[68] Willingale, L., Petrov, G. M., Maksimchuk, A., Davis, J., Freeman, R. R., Joglekar, A. S., ... Krushelnick, K. (2011). Comparison of bulk and pitcher-catcher targets for laser-driven neutron production. Physics of Plasmas, 18(8), 083106.

[69] Lancaster, K. L., Karsch, S., Habara, H., Beg, F. N., Clark, E. L., Freeman, R., ... Zepf, M. (2004). Characterization of 7 Li (p, n) 7 Be neutron yields from laser produced ion beams for fast neutron radiography. Physics of plasmas, 11(7), 3404-3408.

[70] Higginson, D. P., McNaney, J. M., Swift, D. C., Bartal, T., Hey, D. S., Kodama, R., ... Beg, F. N. (2010). Laser generated neutron source for neutron resonance spectroscopy. Physics of plasmas, 17(10), 100701.

[71] Higginson, D. P., McNaney, J. M., Swift, D. C., Petrov, G. M., Davis, J., Frenje, J. A., ... Beg, F. N. (2011). Production of neutrons up to 18 MeV in high-intensity, short-pulse laser matter interactions. Physics of Plasmas, 18(10), 100703.

[72] Hatchett, S. P., Brown, C. G., Cowan, T. E., Henry, E. A., Johnson, J. S., Key, M. H., ... Yasuike, K. (2000). Electron, photon, and ion beams from the relativistic interaction of Petawatt laser pulses with solid targets. Physics of Plasmas, 7(5), 2076-2082.

[73] Hou, B., Nees, J. A., He, Z., Petrov, G., Davis, J., Easter, J. H., ... Krushelnick, K. M. (2011). Laser-ion acceleration through controlled surface contamination. Physics of Plasmas, 18(4), 040702.

[74] Morrison, J. T., Storm, M., Chowdhury, E., Akli, K. U., Feldman, S., Willis, C., ... Freeman, R. R. (2012). Selective deuteron production using target normal sheath acceleration. Physics of Plasmas, 19(3), 030707.

[75] Maksimchuk, A., Raymond, A., Yu, F., Petrov, G. M., Dollar, F., Willingale, L., ... Krushelnick, K. (2013). Dominant deuteron acceleration with a high-intensity laser for isotope production and neutron generation. Applied Physics Letters, 102(19), 191117.

[76] Garrett, A. B. (1962). The neutron identified: Sir james chadwick. Journal of Chemical Education, 39(12), 638.

[77] NRC, U. (2010). Neutron sources. https://www.nrc.gov/docs/ML1122/ML11229A704. pdf. Accessed: 2019-08-23.

[78] Wu, Y. (2009). Development of a Compact Neutron Generator to be Used For Associated Particle Imaging Utilizing a RF-Driven Ion Source (Doctoral dissertation, UC Berkeley).

[79] ARIOLI, F. (2018). Compact laser-driven neutron sources: a theoretical investigation.

[80] Norreys, P. A., Fews, A. P., Beg, F. N., Bell, A. R., Dangor, A. E., Lee, P., ... Cable, M. D. (1998). Neutron production from picosecond laser irradiation of deuterated targets at intensities of. Plasma physics and controlled fusion, 40(2), 175.

[81] "Hercules 300 TW laser", https://cuos.engin.umich.edu/ researchgroups/hfs/facilities/hercules-petawatt-laser/. Accessed: 15-08-2018.

[82] The relativistic lambda cubed laser, https://cuos.engin.umich.edu/researchgroups/hfs /facilities/lambdacubed/. Accessed: 15-08-2018.

[83] Maksimchuk, A., Raymond, A., Yu, F., Petrov, G. M., Dollar, F., Willingale, L., ... Krushelnick, K. (2013). Dominant deuteron acceleration with a high-intensity laser for isotope production and neutron generation. Applied Physics Letters, 102(19), 191117.

[84] Willingale, L., Petrov, G. M., Maksimchuk, A., Davis, J., Freeman, R. R., Joglekar, A. S., ... Krushelnick, K. (2011). Comparison of bulk and pitcher-catcher targets for laser-driven neutron production. Physics of Plasmas, 18(8), 083106.

[85] Hah, J., Petrov, G. M., Nees, J. A., He, Z. H., Hammig, M. D., Krushelnick, K., Thomas, A. G. R. (2016). High repetition-rate neutron generation by several-mJ, 35 fs pulses interacting with free-flowing D2O. Applied Physics Letters, 109(14), 144102.

[86] Brenner, C. M., Mirfayzi, S. R., Rusby, D. R., Armstrong, C., Alejo, A., Wilson, L. A., ... Neely, D. (2015). Laser-driven x-ray and neutron source development for industrial applications of plasma accelerators. Plasma Physics and Controlled Fusion, 58(1), 014039..

[87] Žagar, T., Galy, J., Magill, J., Kellett, M. (2005). Laser-generated nanosecond pulsed neutron sources: scaling from VULCAN to table-top. New Journal of Physics, 7(1), 253.

[88] McKenna, P., Ledingham, K. W. D., Shimizu, S., Yang, J. M., Robson, L., McCanny, T., ... Wei, M. S. (2005). Broad energy spectrum of laser-accelerated protons for spallation-related physics. Physical review letters, 94(8), 084801.

[89] Ioffe, A. C 1 Neutron Sources.

[90] https://www.sandia.gov/pulsed-power/inertial-confinement/

[91] Baltateanu, N., Jurba, M., Calian, V., Stoenescu, G. (2000). Optimal fast neutron sources using linear electron accelerators. In Proceedings of EPAC (pp. 2591-2593).

.

Chapter 9

Appendix

9.1 Geant4 simulation files

9.1.1 DetectorConstruction.cc

```
#include ”B1DetectorConstruction.hh”
#include ”B1SteppingAction.hh”
#include ”G4RunManager.hh”
#include ”G4NistManager.hh”
#include ”G4Material.hh”
#include ”G4Box.hh”
#include ”G4LogicalVolume.hh”
#include ”G4PVPlacement.hh”
#include ”G4SystemOfUnits.hh”
#include ”G4VPrimitiveScorer.hh”
#include ”G4SDManager.hh”
#include ”G4Tubs.hh”
#include ”G4PSEnergyDeposit.hh”
//....oooOO0OOooo........oooOO0OOooo........oooOO0OOooo........oooOO0OOooo......
B1DetectorConstruction::B1DetectorConstruction()
: G4VUserDetectorConstruction()
//....oooOO0OOooo........oooOO0OOooo........oooOO0OOooo........oooOO0OOooo......
B1DetectorConstruction:: B1DetectorConstruction()
//....oooOO0OOooo........oooOO0OOooo........oooOO0OOooo........oooOO0OOooo......
G4VPhysicalVolume* B1DetectorConstruction::Construct()
// Get nist material manager
G4NistManager* nist = G4NistManager::Instance();
// Option to switch on/off checking of volumes overlaps
G4bool checkOverlaps = true;
// World
```

```
G4double world sizeXY = 100.cm; G4double world sizeZ = 100.cm;
G4Box solidWorld = new G4Box(”World”, //its name
world sizeXY, world sizeXY, world_sizeZ);//itssize
G4Material world mat = nist-¿FindOrBuildMaterial(”G4_AIR”);
G4LogicalVolume logicWorld = new G4LogicalVolume(solidWorld, //its solid
world mat, //its material
”World”); //its name
G4VPhysicalVolumephysWorld =
new G4PVPlacement(0, //no rotation
G4ThreeVector(), //at (0,0,0)
logicWorld, //its logical volume
”World”, //its name
0, //its mother volume
false, //no boolean operation
0, //copy number
checkOverlaps); //overlaps checking
// Carbon
G4double Carbon sizeX = (20./2)cm;
G4double Carbon sizeY = (30./2)cm;
G4double Carbon sizeZ = (10./2)cm;
G4Box solidCarbon = new G4Box(”SolidCarbon”, //its name
Carbon sizeX, Carbon_sizeY, Carbon_sizeZ); //its size
G4Material Carbon mat = nist->FindOrBuildMaterial(”G4_C”);
G4LogicalVolume logicCarbon = new G4LogicalVolume(solidCarbon, //its solid
Carbon_mat, //its material
”Carbon_logic”); //its name
new G4PVPlacement(0, // no rotation
G4ThreeVector(0.0cm, 0.0cm, -55cm), // translation position
logicCarbon, // its logical volume
”Carbon_logic”, // its name
logicWorld, // its mother (logical) volume
false, // no boolean operations
0, // its copy number
checkOverlaps); //overlaps checking
// Liquid Nitrogen
```

```
G4double density;
G4double A,Z;
G4double temperature;
// define elemental nitrogen and oxygen
//G4Element elNitrogen = new G4Element(”LiquidNitrogen”, Z=7., A=14.01*g/mole);
G4Box liquidNitrogen = new G4Box(”LiquidNitrogen”, 5.0cm, 5.0cm, 5.0cm);
G4Material Nitrogen_mat = new G4Material(”LiquidNitrogen”, Z=7., A=14.01g/mole,
density=0.808g/cm3, kStateLiquid, temperature=77kelvin);
G4LogicalVolume logic_Nitrogen = new G4LogicalVolume(liquidNitrogen, Nitrogen_mat,”Nitrogen_logic”);
new G4PVPlacement(0, // no rotation
G4ThreeVector(0.0cm, 0.0cm, -35cm), // translation position
logic_Nitrogen, // its logical volume
”Nitrogen_logic”, // its name
logicWorld, // its mother (logical) volume
false, // no boolean operations
0, // its copy number
checkOverlaps); //overlaps checking*/
// WATER
G4double Water_sizeX = (30./2)cm;
G4double Water_sizeY = (20./2)cm;
G4double Water_sizeZ = (10./2)cm;
G4Box Water = new G4Box(”Water”, //its name
Water_sizeX, Water_sizeY, Water_sizeZ); //its size
G4Material Water_mat = nist->FindOrBuildMaterial(”G4$_WATER$”);
G4LogicalVolume logicWater =
new G4LogicalVolume(Water, //its water Water_mat, //its material ”Water_logic”); new G4PVPlacement(0, // no rotation
G4ThreeVector(0.0*cm, 0.0*cm, -10*cm), // translation position
logicWater, // its logical volume
”Water_logic”, // its name
logicWorld, // its mother (logical) volume
false, // no boolean operations
0, // its copy number
checkOverlaps); //overlaps checking
// Inorganic scintillator NaI
```

```
G4String name, symbol;
G4int ncomponents;
G4double a, z;
//G4double abundance;
//Materials
a = 22.98977*g/mole;
G4Element elNa = new G4Element(name=”Sodium”, symbol=”Na” , z= 11., a);
a = 126.9045g/mole;
G4ElementelI = new G4Element(name=”Iodine”, symbol=”I” , z= 53., a);
G4double density_NaI = 3.67g/cm3;
G4Material NaI_mat = new G4Material(name=”NaI_mat”,density_NaI,ncomponents=2);
NaI_mat->AddElement(elNa, 50*perCent);
NaI_mat->AddElement(elI, 50*perCent);
//Solid
G4VSolid NaI_detector = new G4Box( ”NaI_detector”, 25.0*cm, 12.5*cm, 12.5*cm);
//Logical volume
G4LogicalVolume NaI_log = new G4LogicalVolume(NaI_detector, NaI_mat, ”NaI_detector_log”, 0, 0,
0);
//Placement
new G4PVPlacement(0, // no rotation
G4ThreeVector(0.0cm, -50cm, -55.0cm), // translation position
NaI_log, // its logical volume
”NaI_detector”, // its name
logicWorld, // its mother (logical) volume
false, // no boolean operations
0, // its copy number
checkOverlaps); //overlaps checking
G4cout << *(G4Material::GetMaterialTable()) << G4endl;
// Set detector as scoring volume
fScoringVolume_det = NaI_log;
```

9.1.2 DetectorConstruction.hh

```
#ifndef B1DetectorConstructionh
#define B1DetectorConstructionh 1
#include ”G4VUserDetectorConstruction.hh”
#include ”globals.hh”
```

```
class G4VPhysicalVolume;
class B1DetectorConstruction : public G4VUserDetectorConstruction
public:
B1DetectorConstruction();
virtual  B1DetectorConstruction();
public:
virtual G4VPhysicalVolume* Construct();
G4LogicalVolume* GetScoringVolume() const  return fScoringVolume_det;
protected:
G4LogicalVolume* fScoringVolume_det; ;
#endif
```

9.1.3 PrimaryGeneratorAction.cc

```
#include ”B1PrimaryGeneratorAction.hh”
#include ”G4LogicalVolumeStore.hh”
#include ”G4LogicalVolume.hh”
#include ”G4RunManager.hh”
#include ”G4GeneralParticleSource.hh”
#include ”G4ParticleGun.hh”
#include ”G4ParticleTable.hh”
#include ”G4ParticleDefinition.hh”
#include ”Randomize.hh”
#include ”G4SystemOfUnits.hh”
#include ”Analysis.hh”
//....oooOO0OOooo........oooOO0OOooo........oooOO0OOooo........oooOO0OOooo......
B1PrimaryGeneratorAction* B1PrimaryGeneratorAction::fgInstance = 0;
const B1PrimaryGeneratorAction* B1PrimaryGeneratorAction::Instance()
return fgInstance;
B1PrimaryGeneratorAction::B1PrimaryGeneratorAction()
: G4VUserPrimaryGeneratorAction()
fGeneralGun = new G4GeneralParticleSource();
B1PrimaryGeneratorAction:: B1PrimaryGeneratorAction()  delete fGeneralGun;
fgInstance = 0;
void B1PrimaryGeneratorAction::GeneratePrimaries(G4Event* anEvent)
fGeneralGun->GeneratePrimaryVertex(anEvent);
```

```
G4double particleEnergy = fGeneralGun->GetParticleEnergy();
G4AnalysisManager* analysisManager = G4AnalysisManager::Instance();
analysisManager->FillH1(1, particleEnergy);
```

9.1.4 PrimaryGeneratorAction.hh

```
#ifndef B1PrimaryGeneratorAction_h
#define B1PrimaryGeneratorAction_h 1
#include ”G4VUserPrimaryGeneratorAction.hh”
#include ”G4GeneralParticleSource.hh”
#include ”globals.hh”
#include ”G4PhysicalConstants.hh”
class G4GeneralParticleSource;
class G4Event;
class B1DetectorConstruction;
class B1PrimaryGeneratorAction : public G4VUserPrimaryGeneratorAction
public:
B1PrimaryGeneratorAction();
virtual  B1PrimaryGeneratorAction();
static const B1PrimaryGeneratorAction* Instance();
virtual void GeneratePrimaries(G4Event*);
G4GeneralParticleSource* GetGeneralGun() const  return fGeneralGun;
private:
static B1PrimaryGeneratorAction* fgInstance;
G4GeneralParticleSource* fGeneralGun; // pointer a to G4 gun class ;
#endif
```

9.1.5 EventAction.cc

```
#include ”B1EventAction.hh”
#include ”Analysis.hh”
#include ”B1Run.hh”
#include ”G4RunManager.hh”
#include ”G4Event.hh”
#include ”G4SDManager.hh”
#include ”G4HCofThisEvent.hh”
#include ”G4THitsMap.hh”
#include ”G4UnitsTable.hh”
```

```
#include ”G4SystemOfUnits.hh”
#include ”G4PhysicalConstants.hh”
//....oooOO0OOooo........oooOO0OOooo........oooOO0OOooo........oooOO0OOooo......
B1EventAction::B1EventAction(/*B1RunAction* runAction*/)
: G4UserEventAction()
fCollID_cryst(-1),
fcounter(0),
fEdep(-1)
//....oooOO0OOooo........oooOO0OOooo........oooOO0OOooo........oooOO0OOooo......
B1EventAction:: B1EventAction()
//....oooOO0OOooo........oooOO0OOooo........oooOO0OOooo........oooOO0OOooo......
void B1EventAction::BeginOfEventAction(const G4Event* /*evt*/)
fEdep =0.;
fcounter=0;
//....oooOO0OOooo........oooOO0OOooo........oooOO0OOooo........oooOO0OOooo......
void B1EventAction::EndOfEventAction(const G4Event* /*evt*/ )
G4HCofThisEvent* HCE = evt->GetHCofThisEvent();
if(!HCE) return;
if (fCollID_cryst < 0)
G4SDManager* SDMan = G4SDManager::GetSDMpointer();
fCollID_cryst = SDMan -> GetCollectionID(”crystal/edep”);
//Energy in crystals : identify ’good events’
G4THitsMap<G4double¿* evtMap = (G4THitsMap<G4double¿*)(HCE->GetHC(fCollID_cryst));
std::map<G4int,G4double*>::iterator itr;
for (itr = evtMap-¿GetMap()-¿begin(); itr != evtMap-¿GetMap()-¿end(); itr++)
fEdep = *(itr->second);
G4double fEdep;
G4AnalysisManager* analysisManager = G4AnalysisManager::Instance();
if (fEdep > 0.0)
analysisManager->FillNtupleDColumn(0,fEdep);
analysisManager->AddNtupleRow();
```

9.1.6 EventAction.hh

```
#ifndef B1EventActionh
#define B1EventActionh 1
```

```
#include ”G4UserEventAction.hh”
#include ”G4THitsMap.hh”
#include ”G4Accumulable.hh”
#include ”globals.hh”
#include ”G4ThreeVector.hh”
class B1EventAction : public G4UserEventAction
public:
B1EventAction();
virtual  B1EventAction();
virtual void BeginOfEventAction(const G4Event* event);
virtual void EndOfEventAction(const G4Event* event);
void AddEdep(G4double edep)  fEdep += edep; /*G4cout<<”Energy deposited: ”<<fEdep<<G4endl;*/;
private:
G4double fEdep;
;
#endif
```

9.1.7 RunAction.cc

```
#include ”B1RunAction.hh”
#include ”B1PrimaryGeneratorAction.hh”
#iinclude ”B1EventAction.hh”
#iinclude ”B1SteppingAction.hh”
#iinclude ”G4AccumulableManager.hh”
#iinclude ”G4Run.hh”
#include ”G4ParticleTable.hh”
#include ”G4ParticleDefinition.hh”
#include ”G4Track.hh”
#include ”G4Gamma.hh”
#include ”G4Electron.hh”
#include ”G4Positron.hh”
#include ”G4RunManager.hh”
#include ”G4UnitsTable.hh”
#include ”Analysis.hh”
#include ”G4SystemOfUnits.hh”
//....oooOO0OOooo........oooOO0OOooo........oooOO0OOooo........oooOO0OOooo......
```

```
B1RunAction::B1RunAction()
: G4UserRunAction()
analysisManager = G4AnalysisManager::Instance();
analysisManager->SetFirstHistoId(1);
// Creating histograms
analysisManager->CreateH1(”input_spectrum”,”Input Spectrum”, 2000, 0., 20.0*MeV);
// Creating ntuple
analysisManager->CreateNtuple(”NAI”, ”Edep”);
analysisManager->CreateNtupleDColumn(”Total_Deposited_Energy”);
analysisManager->FinishNtuple();
//....oooOO0OOooo........oooOO0OOooo........oooOO0OOooo........oooOO0OOooo......
B1RunAction:: B1RunAction()
// complete cleanup
delete G4AnalysisManager::Instance();
//....oooOO0OOooo........oooOO0OOooo........oooOO0OOooo........oooOO0OOooo......
void B1RunAction::BeginOfRunAction(const G4Run* /*aRun*/)
G4RunManager::GetRunManager()->SetRandomNumberStore(false);
// Open an output file
G4String fileName = ”Cf252Histo”; //used to be commented
analysisManager->OpenFile(fileName);
//....oooOO0OOooo........oooOO0OOooo........oooOO0OOooo........oooOO0OOooo......
void B1RunAction::EndOfRunAction(const G4Run* aRun)
G4int nofEvents = aRun->GetNumberOfEvent();
if (nofEvents == 0) return;
analysisManager->Write();
analysisManager->CloseFile();
```

9.1.8 RunAction.hh

```
#include ”G4UserRunAction.hh”
#include ”globals.hh”
#include ”Analysis.hh”
class G4Run;
class B1RunAction : public G4UserRunAction
public:
B1RunAction();
```

```
virtual  B1RunAction();
virtual void BeginOfRunAction(const G4Run*);
virtual void EndOfRunAction(const G4Run*);
private:
;
#endif
```